

MATHEMATICAL MODELING OF SPECIES-SPECIFIC DIACYLGLYCEROL
DYNAMICS IN THE RAW 264.7 MACROPHAGE FOLLOWING P2Y₆
RECEPTOR ACTIVATION BY URIDINE 5'-DIPHOSPHATE.

By

Hannah L. Callender

Dissertation

Submitted to the Faculty of the
Graduate School of Vanderbilt University
in partial fulfillment of the requirements
for the degree of

DOCTOR OF PHILOSOPHY

in

Mathematics

August, 2007

Nashville, Tennessee

Approved:

Date:

Mary Ann Horn

May 23, 2007

H. Alex Brown

May 23, 2007

Glenn F. Webb

May 23, 2007

Philip S. Crooke

May 23, 2007

Emmanuele DiBenedetto

May 23, 2007

Copyright © 2007 by Hannah L. Callender
All Rights Reserved

ACKNOWLEDGEMENTS

I would first like to thank my advisor, Professor Mary Ann Horn, for all of her help and guidance. In addition to all of her mathematical advice, she has provided exceptional career advice and moral support for which I will be infinitely grateful.

I would next like to thank my biology advisor, Professor H. Alex Brown, for giving me the opportunity to develop my skills as a true biomathematician while working in his laboratory, as well as for providing me with continual support and encouragement.

I would also like to thank Professor Glenn Webb for serving as my on site mathematics advisor and for providing key ideas for analysis techniques and encouragement, Professor Emmanuele DiBenedetto for serving as my inspiration to enter into the field of mathematical biology, and Professor Philip Crooke for his valuable feedback on my research.

This work was supported in part by the Alliance for Cellular Signaling National Institutes of Health grant, LIPID MAPS, the Ingram Endowment (to HAB) and by a Vanderbilt University Summer Research Award (HLC). I am thankful for that support.

Finally, I would like to thank my friends and family for their unconditional love and encouragement, and my Lord and Savior Jesus Christ for remaining by my side throughout this journey.

TABLE OF CONTENTS

	Page
ACKNOWLEDGEMENTS	iii
LIST OF TABLES	vi
LIST OF FIGURES	vii
LIST OF ABBREVIATIONS	ix
Chapter	
I INTRODUCTION	1
II MODEL CONSTRUCTION	7
II.1 Module 1: Receptor Dynamics	7
II.2 Module 2: G-protein Cascade	10
II.3 Module 3: Diacylglycerol production and degradation	13
II.4 Module 4: Cytosolic Calcium dynamics	16
II.5 Dimensionless Scaling	18
II.6 Initial Conditions of the Model	20
III THEORETICAL MODEL ANALYSIS	22
III.1 Introduction	22
III.2 Existence and Uniqueness of Solutions	24
III.3 Steady-State Solution	38
III.3.1 Local Stability of Steady States	40
III.3.2 Global Stability of Steady States	45
IV NUMERICAL MODEL ANALYSIS	60
IV.1 Introduction	60
IV.2 Estimation of Unknown Rate Parameters from Experimental Data	61
IV.2.1 Numerical Methods	61
IV.2.2 Experimental Methods	63
IV.2.3 Parameter Estimation	64
IV.3 Sensitivity Analysis	71
IV.3.1 Sampling Method and Sensitivity Technique	71
IV.3.2 Implementation of the Sensitivity Methods	74
V DIACYLGLYCEROL PATHWAY ANALYSIS	79
V.1 Introduction	79
V.2 Two-Dose UDP Experiments	80
V.3 DAG Kinase Inhibitor II (R59949) Experiments	80

V.4	Multiple DAG Inhibitors Experiments	88
V.5	Propranolol Experiments	91
VI	QUANTIFICATION OF MOLECULAR SPECIES OF DIACYLGLYCEROL	96
VI.1	Introduction	96
VI.2	Experimental Materials and Methods	98
VI.2.1	Materials	98
VI.2.2	Extraction of glycerophospholipids from stimulated cells	99
VI.2.3	Diacylglycerol isolation and recovery	99
VI.2.4	Mass spectrometric analysis of DAG extracts	100
VI.3	Results and Discussion	100
VI.3.1	Isotopic correction	100
VI.3.2	Chromatographic separation and DAG detection	104
VI.3.3	Mathematical analysis of data and development of standard curves	105
VI.3.4	Quantification of DAG species in RAW 264.7 cells after PAF stimulation	113
VII	CONCLUSIONS AND FUTURE DIRECTIONS	117
VII.1	Modeling Results	117
VII.2	Pathway Analysis Results	119
VII.3	DAG Quantification Results	121
Appendix		
A	ADDITIONAL SIMULINK FIGURES	123
B	MATLAB CODE FOR NUMERICAL ANALYSIS	123
BIBLIOGRAPHY		153

LIST OF TABLES

Table	Page
1 Time-dependent nondimensionalized model variables	18
2 Modified rate parameters for nondimensionalized system	19
3 Eigenvalues for the Jacobian Matrix	44
4 Time-independent model variables	65
5 Materials used for DAG quantification	98
6 % Total abundance of masses of naturally occurring 38:4 DAG	103
7 Slopes for eight DAG standards	109
8 Coefficients of the multiple parameter linear model for estimating slopes .	111
9 Predicted slopes for the 28 species of DAG	112
10 Limits of detection for the eight DAG internal standards	113

LIST OF FIGURES

Figure	Page
1 Schematic of UDP canonical pathway	11
2 Two pool DAG model	15
3 Jacobian matrix of our system at the steady state solution ξ	43
4 Full SIMULINK model	62
5 UDP Timecourse for 38:4 and 34:1 DAG, IP ₃ , and Ca ²⁺	66
6 UDP Timecourse for P2Y ₆ , G α -GTP, and PIP ₂	70
7 SRCs and R _y ² values for IP ₃	75
8 SRCs and R _y ² values for DAG	76
9 34:1 DAG changes for variations in k _{dp2}	77
10 34:1 DAG changes for variations in k _{ap2}	78
11 34:1 DAG changes for variations in k _{dp1}	78
12 Two-Dose UDP DAG Graphs	81
13 Fold changes and p-values for DAG response to 250 nM UDP	82
14 Fold changes and p-values for DAG response to 250 μ M UDP	82
15 DAG Kinase Inhibitor Graphs	84
16 Differences and p-values for R59949 data	85
17 Comparison between responses of UDP and UDP + R59949	86
18 Propranolol effects on DAG response to UDP at 15 minutes	88
19 Thimerosal effects on DAG response to UDP at 15 minutes	89
20 U73122 effects on DAG response to UDP at 15 minutes	89
21 U73433 effects on DAG response to UDP at 15 minutes	90
22 R59949 effects on DAG response to UDP at 15 minutes	90
23 Propranolol Graphs	92
24 Lipid Array for PA response to UDP +/- Propranolol	94
25 Identification of DAG sodium adducts	101

26	Baseline mass spectrum from RAW 264.7 cell extract	102
27	Example of isotopic correction	103
28	Positive ESI mass spectrum with 9 diacylglycerol standards	106
29	Effects on normalized signal strength of additions of 34:1 DAG to lipid extracts from RAW 264.7 cells.	108
30	Differences in standard curves among different cellular extracts.	114
31	PAF timecourse for four DAG species	116
32	SIMULINK Activated Receptor subsystem	123
33	SIMULINK Inactivated Receptor subsystem	123
34	SIMULINK Activated G-protein subsystem	124
35	SIMULINK PIP ₂ subsystem	124
36	SIMULINK IP ₃ subsystem	125
37	SIMULINK DAG _{p1} subsystem	126
38	SIMULINK DAG _{p2} subsystem	126
39	SIMULINK Cytosolic Ca ²⁺ subsystem	127
40	SIMULINK h subsystem	128
41	SIMULINK c ₀ subsystem	128
42	SIMULINK Block Definitions	129

LIST OF ABBREVIATIONS

Abbreviation

GPCR	G-protein-coupled receptor
Ca ²⁺	calcium
ER	endoplasmic reticulum
PLC	phospholypase C
PIP ₂	phosphatidylinositol 4,5-bisphosphate
DAG	diacylglycerol
IP ₃	inositol 1,4,5-trisphosphate
ATP	adenosine triphosphate
RNA	ribonucleic acids
DNA	deoxyribonucleic acid
UTP	uridine triphosphate
ADP	adenosine diphosphate
UDP	uridine diphosphate
ODEs	ordinary differential equations
N _X	number of molecules of species X
[X]	concentration (in μM) of species X
IP ₃ -R	IP ₃ receptor
GDP	guanine diphosphate
GTP	guanine triphosphate
PA	phosphatidic acid
PUFA	poly-unsaturated fatty acid
PLD	phospholipase D
PI	phosphatidylinositol
CDP-DG	cytidine diphosphate DAG
SRC	standardized regression coefficient

LHS	latin hypercube sampling
R_y^2	model coefficient of determination
DAGk	DAG kinase
LPP	lipid phosphate phosphatase
MAG	monoacylglycerol
MAGT	monoacylglycerol acyltransferase
MALDI	matrix-assisted laser desorption/ionization
ESI-MS	electrospray ionization mass spectrometry
PAF	platelet-activating factor
PC	phosphatidylcholine
PE	phosphatidylethanolamine
RSE	residual standard error
LOD	limit of detection

CHAPTER I

INTRODUCTION

Strong selection advantages are provided to any organism with the ability to send, receive and interpret information from the surrounding environment. In order to achieve proper development and function, multi-cellular organisms require an elaborate communication network between individual cells. These networks typically rely on the release and subsequent binding of signaling molecules. The effects of the signals on the target cells are very broad; responses can include survival, chemotaxis, proliferation, and even programmed cell death (apoptosis). The process of a signaling molecule, also called a ligand, binding to a receptor protein and subsequently causing a response is known as cell signaling.

Cell signaling can be divided into three stages: reception, transduction, and response. Reception occurs when a chemical agent from outside the cell binds to a cellular protein, often at the cell's surface. This binding of the signal molecule alters the receptor protein in some way, which initiates the process of transduction. Transduction then converts the signal to a different form in order to elicit a specific cellular response. Transduction may occur in one step; however it often requires a signal-transduction pathway involving a complex series of relay molecules. In the third stage of signaling, the transduced signal triggers the specific cellular response, which can include catalysis by an enzyme, rearrangement of the cytoskeleton, or activation of specific genes in the nucleus. The cell-signaling process is a critical component of cell behavior, playing an important role in normal cell development.

In order to recognize many different signals, cells express a large variety of receptor proteins that can recognize specific signal molecules. The binding of a signal molecule occurs due to its complementary shape with a specific site on the receptor, similar to a key in a lock. Many receptors are found on the cell membrane, also known as

the plasma membrane. Although the plasma membrane regulates the entry and exit of both protein constituents and small molecules, these molecules can also influence cellular activity through the binding to specific sites on receptor proteins embedded in the cell's plasma membrane. Such receptors can then transmit the information to the inside of the cell through allostery (changing shape) or aggregation caused by the binding of the ligand. Three major classes of receptors are G-protein-coupled receptors (GPCRs), tyrosine-kinase receptors, and ion-channel receptors.

Not all components of signal-transduction pathways are proteins. Second messengers, which are small, non-protein molecules or ions generated in response to an extracellular signaling molecule binding to a cell-surface receptor, play a vital role in signal transduction by activating other pathway components. Due to their small size, second messengers can readily spread throughout the cell by diffusion, where they participate in pathways initiated by both GPCRs and tyrosine-kinase receptors. Two of the most widely used and studied second messengers are cyclic adenosine monophosphate and calcium ions (Ca^{2+}). A large variety of relay proteins are sensitive to the cytosolic concentration of one or the other of these second messengers which can produce hysteretic responses in the target cells, allowing an initial response to be translated into longer term effects.

Many signaling molecules in animals, including neurotransmitters, growth factors, and some hormones, use signal transduction pathways which increase the cytosolic concentration of Ca^{2+} . This increase in Ca^{2+} is used to produce a wide variety of tissue dependent responses, which include muscle cell contraction, secretion of various hormones or enzymes, and cell division. Calcium also functions as a second messenger in plant cell signaling pathways that allow for coping with environmental stresses, such as drought or cold. Cells use Ca^{2+} as a second messenger in both G-protein pathways and tyrosine-kinase pathways. Although cells contain Ca^{2+} , this ion is able to function as a second messenger because of the concentration gradient created between the various compartments within the cell. Calcium ions are actively transported out

of the cytosol by a variety of protein pumps, which either remove the Ca^{2+} ions from the cell or sequester it within various cellular organelles including the endoplasmic reticulum (ER), mitochondria, or chloroplasts (in plant cells). As a result, the cytosolic concentration is usually much lower than that of the ER and extracellular fluid. Upon receiving a signal, the cytosolic Ca^{2+} level may rise, usually by a mechanism that releases Ca^{2+} from the cell's ER. Once a signal molecule binds to a receptor, the enzyme phospholipase C (PLC) is activated. This enzyme cleaves the plasma-membrane phospholipid phosphatidylinositol 4,5-bisphosphate (PIP_2) into two other second messengers, diacylglycerol (DAG) and inositol 1,4,5-trisphosphate (IP_3). IP_3 , a small molecule, quickly diffuses through the cytosol and binds to a ligand-gated calcium channel in the ER membrane, causing it to open. Calcium ions flow out of the ER (down their gradient, from areas of higher to lower concentration), raising the Ca^{2+} level in the cytosol. The Ca^{2+} ions activate the next protein in one or more signaling pathways, often by means of calmodulin, a Ca^{2+} -binding protein present at high levels in eukaryotic cells. The proteins most often regulated by calmodulin are protein kinases (enzymes that transfer phosphate groups from adenosine triphosphate (ATP) to a protein) and phosphatases (enzymes that remove phosphate groups from proteins)-the most common relay proteins in signaling pathways.

Due to the importance of these cellular signaling pathways in cellular function, much research has been conducted in order to identify the underlying mechanisms. However, signaling pathways often involve large numbers of molecules and varying levels of complexity, limiting the amount of information attainable from traditional experimental methods and thus suggesting the construction and analysis of quantitative models. Such mathematical models enable one to simultaneously study individual pathway elements and make predictions about the dynamical and interconnected behavior of the signaling pathway, such as the effect of pathway perturbations or the discovery of novel pathway components, and are thus powerful tools for directing further experimental research.

Although nucleotides serve as some of the most basic building blocks of ribonucleic acids (RNA) and deoxyribonucleic acid (DNA), they can also act as important signaling molecules, activating the family of P2 nucleotide receptors [35]. Nucleotides such as adenosine triphosphate (ATP) and uridine triphosphate (UTP) are known to regulate an array of diverse biological effects upon their release from cells that have undergone inflammation due to trauma or have been mechanically stimulated [7, 23, 36, 87]. Once released into the extracellular fluid, ATP and UTP are degraded by enzymes called ecto-nucleotidases into adenosine diphosphate (ADP) and uridine diphosphate (UDP), respectively [13, 26, 88]. UDP then serves as the primary agonist, or ligand, for the G protein-coupled receptor known as P2Y₆ [51].

This work focuses on modeling the signaling events downstream UDP activation of the P2Y₆ receptor in a macrophage-like cell line. Originating from monocytes (white blood cells), macrophages move through tissue fibers and engulf and then digest cellular debris and pathogens. This process of ingesting an invading organism by certain types of white cells is known as phagocytosis, and tissue macrophages are the largest phagocytic cells. Because of the difficulty of working with cells taken directly from an organism, our data are collected from a specific cell line. These cells are grown and live in a tissue-culture dish, surrounded by appropriate media for cell survival. They are similar to the primary cell (taken from the organism) but are essentially “immortal”, in that they will continue to grow and survive for as long as they are provided with nutrients. The macrophage-like cell line from which all of our data are derived is called RAW 264.7.

There have been a number of mathematical models developed to study GPCR signaling pathways in a variety of cell types [21, 39, 45, 73, 80]. Although several models have helped to uncover complex interactions in the areas of the G-protein cascade [43, 74, 85] and the intricate details surrounding the above mentioned Ca²⁺ flux [16, 19, 33, 40, 76], there is no information on modeling DAG changes following GPCR stimulation. DAGs also serve as second messengers through the activation

of protein kinase C, an enzyme linked to the regulation of many cellular processes including cell differentiation, proliferation, carcinogenesis, development, and memory in multiple mammalian cell types [4, 15, 46, 50, 52]. Increase in intracellular DAG levels is also believed to contribute to the transduction of mitogenic signals [24, 42, 54, 59, 69] as well as secondary secretion and aggregation [78]. More than 50 different species of DAG have been identified, depending on acyl chain length (number of carbons in the two fatty acyl chains of the DAG molecule) and degree of unsaturation (number of double bonds in the fatty acyl chains). With evidence for differential roles of these species in cellular processes [14, 55], determining the species-specific regulation of DAG in the signaling process is crucial to obtaining a comprehensive understanding of how the cell responds to its stimulus. The work presented here therefore places a major emphasis on the study of species-specific DAG dynamics. Though the mechanisms of DAG production and degradation downstream agonist stimulation of P2Y receptors is still relatively unclear, our modeling efforts are leading to new insights and novel pathway propositions.

In this dissertation, we describe a system of ten nonlinear ordinary differential equations (ODEs) which we have constructed to model the UDP signaling pathway in RAW 264.7 cells. In Chapter II, we describe in detail the interactions and corresponding ODEs involved in this signaling pathway, including the introduction of a novel branch of the signaling pathway involving DAG kinetics as suggested by the model. In Chapter III, we rigorously analyze the existence and uniqueness of solutions of the full model as well as the positivity, boundedness, and stability behavior of steady states for an altered model whereby the Ca^{2+} interactions have been simplified. In Chapter IV, we provide methods and descriptions of the numerical analysis performed, including parameter estimation techniques used to obtain best fits to experimental data and sensitivity analysis to determine which rate parameters are responsible for the most model output uncertainty. Then in Chapter V, we discuss results from data analysis of experiments performed to test the newly proposed signaling pathway introduced

in Chapter II. Chapter VI is devoted to the development of a novel method of simultaneous quantification of multiple species of DAG, a method which has enhanced the modeling efforts by enabling the modeling of species-specific DAG dynamics. This method has been previously published in *Analytical Chemistry* (Callender, et al.). In Chapter VII, we draw the final conclusions of our mathematical modeling efforts and propose future areas of research, both biological and mathematical. Finally, Chapters VII.3 and VII.3 are devoted to Appendices A and B, respectively, where we include further explanation of the numerical methods of analysis used, including code written to generate numerical simulations to the system of ODEs.

CHAPTER II

MODEL CONSTRUCTION

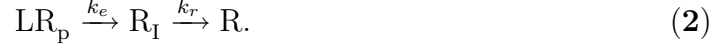
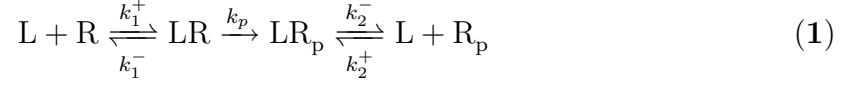
Our model utilizes the the law of mass action which is based on diffusion of species (in the membrane or cytosol), collisional interaction, and binding (or unbinding), such that the effective rates (of production or degradation) are proportional to the number of molecules (or concentration) of each species that contributes to a given reaction. The model consists of a system of ten nonlinear ordinary differential equations and is separated into four modules: Receptor Dynamics, G-protein Cascade, DAG Production and Degradation, and Cytosolic Calcium Dynamics. Where appropriate, number of molecules of species X will be denoted by N_X , while $[X]$ will denote the concentration of X in μM .

II.1 Module 1: Receptor Dynamics

Our representation of P2Y₆ receptor dynamics is based on previous work by Lemon et al. [39], which provides a detailed account of receptor regulation for the P2Y₂ receptor in response to its primary agonist UTP [51]. In the case of the P2Y₆ receptor, the mechanisms are assumed to be similar to those of P2Y₂, only Brinson and Harden [6] observed a much slower rate of desensitization for the P2Y₆ receptor in response to its primary agonist UDP. To account for this slower rate of desensitization, the receptor phosphorylation rate, k_p , is modified to fit the P2Y₆ observations of Brinson and Harden.

The activity of a GPCR is regulated by several processes. GPCRs may undergo phosphorylation and subsequent uncoupling from G-proteins or internalization. The phosphorylated receptors can then be dephosphorylated, returning to the surface of the plasma membrane. In our model, we assume that the ligand is not depleted by binding to the receptors and therefore has a fixed concentration. The reactions

involved for receptor dynamics are therefore given by the following:



As seen in equations (1) and (2), cell surface receptors are allowed to bind extracellular ligand reversibly, with forward rate constant k_1^+ and backward rate constant k_1^- . Ligand-bound receptors, LR, can be phosphorylated and therefore inactivated irreversibly at a rate k_p , forming LR_p , while phosphorylated receptors, R_p are still able to interact with ligand but with possibly different rates of binding and unbinding, given by k_2^\pm [60]. Since phosphorylation of LR causes desensitization of these receptors, G-protein is only activated by unphosphorylated receptors, R and LR. Although Lemon's model is similar to the cubic ternary complex model [77] in that G-proteins are allowed to bind to both R and LR, upon further analysis Lemon showed that under certain assumptions receptor/ligand and G-protein systems largely decouple and the only receptors that need to be included in the G-protein cascade are the activated surface receptors, LR. Upon phosphorylation, receptors are internalized at a rate that depends on agonist occupancy. This is incorporated into the model by having the phosphorylated receptors, LR_p , internalized at the rate k_e . Internalized receptors, R_I , are then recycled back to the surface at a rate k_r . The ordinary differential equations corresponding to the reactions from equations (1) and (2) are

$$\frac{dN_R(t)}{dt} = -k_1^+[L]N_R + k_1^-N_{LR} + k_rN_{R_I}, \quad (3)$$

$$\frac{dN_{LR}(t)}{dt} = k_1^+[L]N_R - (k_1^- + k_p)N_{LR}, \quad (4)$$

$$\frac{dN_{LR_p}(t)}{dt} = k_2^+[L]N_{R_p} - (k_2^- + k_e)N_{LR_p} + k_pN_{LR}, \quad (5)$$

$$\frac{dN_{R_p}(t)}{dt} = -k_2^+[L]N_{R_p} + k_2^-N_{LR_p}, \quad (6)$$

$$\frac{dN_{R_I}(t)}{dt} = -k_rN_{R_I} + k_eN_{LR_p}, \quad (7)$$

where $[L]$ denotes the ligand concentration, N_R and N_{LR} represent number of unbound and bound receptors, N_{R_p} and N_{LR_p} represent number of phosphorylated unbound and phosphorylated bound receptors, and N_{R_I} is the number of internalized receptors. Since this is a closed system (the sum of equations (3)-(7) is zero), we have that the total number of receptors in the cell, N_{R_T} , is given by

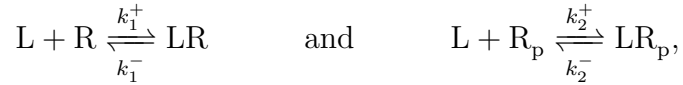
$$N_R + N_{LR} + N_{LR_p} + N_{R_p} + N_{R_I} = N_{R_T}. \quad (8)$$

The kinetics of ligand binding are considered to be fast relative to the other processes in the model, so that we may combine equations (3)-(7) to leave only the slow kinetics given by

$$\frac{dN_{R^S}(t)}{dt} = -k_r N_{R_I} - k_p N_{LR}, \quad (9)$$

$$\frac{dN_{R_p^S}(t)}{dt} = -k_e N_{LR_p} + k_p N_{LR}, \quad (10)$$

where $N_{R^S} = N_R + N_{LR}$ represents the total number of unphosphorylated, and therefore “active”, surface receptors, and $N_{R_p^S} = N_{R_p} + N_{LR_p}$ represents the total number of phosphorylated, and therefore “inactive”, surface receptors. Ligand binding occurs through the following reactions:



where k_1^\pm and k_2^\pm are the forward and backward rate constants for ligand binding to unphosphorylated and phosphorylated receptor, respectively. Therefore, the rapid ligand binding kinetics assumption [76], which is equivalent to assuming instantaneous equilibrium in the two above reactions, along with mass action kinetics gives

$$\frac{dN_R(t)}{dt} = -k_1^+[L]N_R + k_1^-N_{LR} = 0, \quad (11)$$

$$\frac{dN_{LR}(t)}{dt} = k_1^+[L]N_R - k_1^-N_{LR} = 0, \quad (12)$$

$$\frac{dN_{LR_p}(t)}{dt} = k_2^+[L]N_{R_p} - k_2^-N_{LR_p} = 0, \quad (13)$$

$$\frac{dN_{R_p}(t)}{dt} = -k_2^+[L]N_{R_p} + k_2^-N_{LR_p} = 0. \quad (14)$$

Simplifying equations (11) through (14) and using $N_{R^S} = N_R + N_{LR}$ and $N_{R_p^S} = N_{R_p} + N_{LR_p}$ from above, we have the following relations:

$$N_R = \frac{K_1 N_{R^S}}{K_1 + [L]}, \quad (15)$$

$$N_{LR} = \frac{[L] N_{R^S}}{K_1 + [L]}, \quad (16)$$

$$N_{LR_p} = \frac{[L] N_{R_p^S}}{K_2 + [L]}, \quad (17)$$

$$N_{R_p} = \frac{K_2 N_{R_p^S}}{K_2 + [L]}, \quad (18)$$

where $K_1 = k_1^-/k_1^+$ is the unphosphorylated receptor dissociation constant and $K_2 = k_2^-/k_2^+$ is the phosphorylated receptor dissociation constant. Substituting equations (15)-(18) into equations (9) and (10) and using the conservation equation (8), receptor regulation is modeled using the following reduced two-variable system:

$$\frac{dN_{R^S}(t)}{dt} = k_r N_{R_T} - \left(k_r + \frac{k_p [L]}{K_1 + [L]} \right) N_{R^S} - k_r N_{R_p^S} \quad (19)$$

$$\frac{dN_{R_p^S}(t)}{dt} = [L] \left(\frac{k_p N_{R^S}}{K_1 + [L]} - \frac{k_e N_{R_p^S}}{K_2 + [L]} \right). \quad (20)$$

II.2 Module 2: G-protein Cascade

A simplified schematic of the canonical signaling pathway downstream receptor activation by UDP is shown in Figure 1. Once a P2Y₆ receptor becomes activated through ligand binding, it undergoes a conformational change (a change in shape), allowing

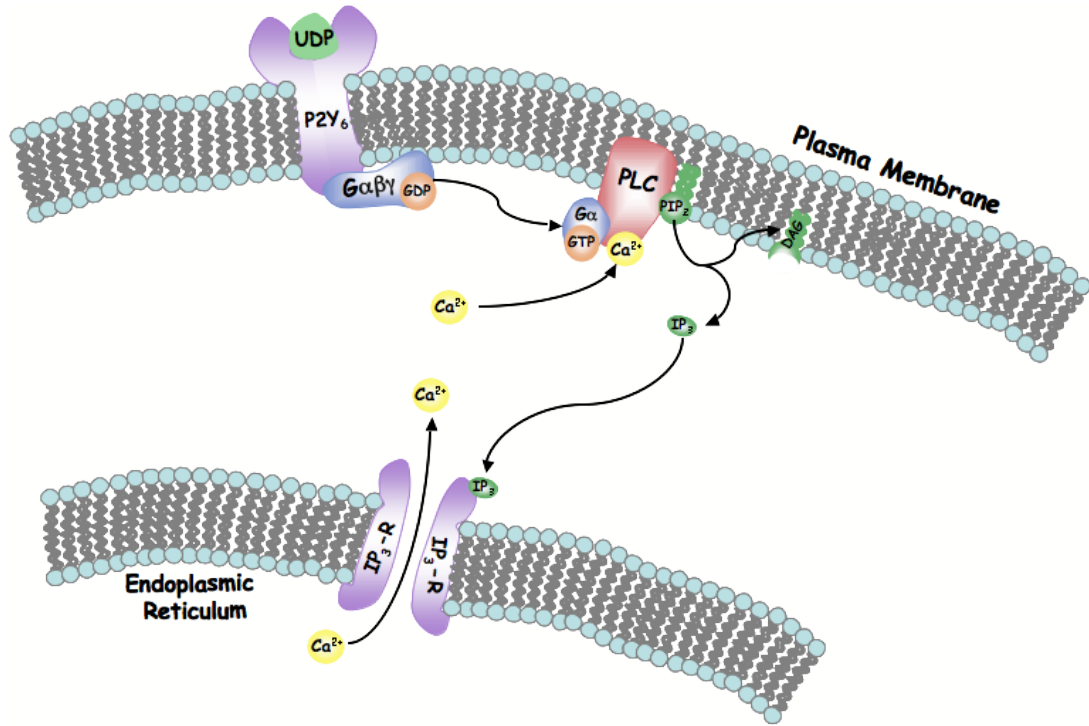


Figure 1: Simplified schematic of the UDP signaling pathway. UDP binds to the P2Y₆ receptor, causing exchange of GDP for GTP on the bound G-protein and release of G α ·GTP from G $\beta\gamma$. Activated G α ·GTP and Ca²⁺ bind to and activate membrane-bound PLC, which then hydrolyses PIP₂ into DAG and IP₃. IP₃ diffuses through the cytosol and releases Ca²⁺ from the ER by binding to the IP₃ receptor (IP₃-R).

a G-protein to bind to the activated receptor. G-proteins are receptor activated proteins that are bound to the inside surface of the cell membrane. They consist of three subunits: G α , and the tightly associated G β and G γ . Once bound to an activated GPCR, the G-protein releases its bound nucleotide guanine diphosphate (GDP) from the G α subunit, binding a new molecule of guanine triphosphate (GTP). This nucleotide exchange causes the dissociation of the GTP-bound G α subunit, the G $\beta\gamma$ dimer, and the GPCR. Although both G α ·GTP and G $\beta\gamma$ can then activate different signaling pathways and effector proteins, we are concerned only with the reactions downstream G α ·GTP activation. Eventually the G α subunit will hydrolyze the GTP to GDP through its inherent enzymatic activity. This allows G α to reassociate with G $\beta\gamma$, starting a new cycle. A simplified model of the time-dependent production and

degradation of $G\alpha\cdot\text{GTP}$, denoted by G^* , is

$$\frac{dN_{G^*}(t)}{dt} = k_a N_{RS} (N_{G_T} - N_{G^*}) - k_d N_{G^*}, \quad (21)$$

where, according to mass action kinetics, we have assumed that G^* are produced at a rate proportional to the number of activated surface receptors, N_{RS} , and the number of inactive G-proteins, $N_{G_T} - N_{G^*}$, where N_{G_T} is the total number of G-proteins, both activated and inactivated. The second term in equation (21) represents deactivation rate of G-proteins from hydrolysis of GTP into GDP and is proportional to the current number of active G-proteins. As laterally diffusing $G\alpha\cdot\text{GTP}$ subunits bind the (presumably freely diffusing) inactive cytosolic PLC enzymes on the inner leaflet of the plasma membrane, $G\alpha\cdot\text{GTP}\cdot\text{PLC}$ complexes are formed.

The bound state complex $G\alpha\cdot\text{GTP}\cdot\text{PLC}$ is considered fully activated when bound to Ca^{2+} where it then hydrolyzes plasma membrane-bound PIP_2 molecules into IP_3 and DAG. For simplicity, we assume that the number of $G\alpha\cdot\text{GTP}\cdot\text{PLC}$ complexes is directly proportional to the number of G^* , with proportionality constant λ , and PIP_2 replenishment occurs through a phenomenological term linear in the difference from the initial amount, $N_{\text{PIP}_2}(0)$. Therefore we can write the time dependence of PIP_2 as

$$\begin{aligned} \frac{dN_{\text{PIP}_2}(t)}{dt} = & -k_{hyd} \left(\frac{[\text{Ca}^{2+}]}{K_c + [\text{Ca}^{2+}]} \right) \lambda N_{G^*} N_{\text{PIP}_2} \\ & + k_{rep} (N_{\text{PIP}_2}(0) - N_{\text{PIP}_2}), \end{aligned} \quad (22)$$

where the effective hydrolysis rate is proportional to the number of PIP_2 and G^* molecules, with rate constant k_{hyd} , and we assume rapid binding kinetics of cytosolic Ca^{2+} (in μM) to the activated $G\alpha\cdot\text{GTP}\cdot\text{PLC}$ complex. Here K_c represents the dissociation constant for the Ca^{2+} binding site on the PLC molecule.

The generation of IP_3 is determined by the hydrolysis rate of PIP_2 . As IP_3 molecules are known to diffuse through the cytosol, we refer to IP_3 production and degradation in terms of concentration (in μM) instead of number of molecules. We

assume that IP_3 is degraded at a rate proportional to the current concentration of IP_3 , with rate constant k_{d3} . The equation for IP_3 is therefore

$$\frac{d[IP_3](t)}{dt} = k_{hyd} \left(\frac{[Ca^{2+}]}{K_c + [Ca^{2+}]} \right) \lambda N_{G^*} \left(\frac{10^6}{N_{av} \cdot v} \right) N_{PIP_2} - k_{d3} [IP_3], \quad (23)$$

where v is the volume of the cell (in L) and N_{av} is Avogadro's constant.

II.3 Module 3: Diacylglycerol production and degradation

The main focus of this work is on modeling the production and degradation of different species of DAG. As stated above, it is well-known that early DAG production is a result of PIP_2 hydrolysis at the plasma membrane [30, 81, 82], where it is produced stoichiometrically with IP_3 . DAG can then be converted into other molecules via several pathways. In particular, a diacylglycerol kinase can phosphorylate DAG into phosphatidic acid (PA). The effects of these pathways are combined into one effective rate constant, k_{dp1} , so that the rate at which DAG is lost is proportional to its current concentration. Using this canonical pathway to describe total DAG production and degradation in the cell results in an equation very similar to that of IP_3 :

$$\frac{d[DAG](t)}{dt} = k_{hyd} \left(\frac{[Ca^{2+}]}{K_c + [Ca^{2+}]} \right) \lambda N_{G^*} \left(\frac{10^6}{N_{av} \cdot v} \right) N_{PIP_2} - k_{dp1} [DAG]. \quad (24)$$

Using a new method of DAG quantification developed by Callender et al. [10], which allows for the simultaneous quantification of up to 28 different species of DAG, we found that the responses of many DAG species cannot be modeled via this signaling pathway alone (see Fig. 5a and 5b). In fact, many mono- and di-unsaturated DAGs (DAGs with one or two double bonds) such as 34:1 DAG (containing 34 carbons and 1 double bond), shown in Figure 5b, exhibit a biphasic response to a $25\mu\text{M}$ stimulation with UDP.

These data suggest the existence of two separate pools of DAG for each DAG species: DAG_{p1} , originating from PIP_2 hydrolysis post agonist stimulation and de-

graded as described above, and an intracellular pool, DAG_{p2} , present in high concentrations in resting cells, that is rapidly converted to PA upon UDP stimulation via a DAG kinase, therefore creating an initial decrease in DAG_{p2} levels. Each DAG species has varying levels of representation in each of these two pools. For instance, the second pool contains more of the mono- and di-unsaturated DAG species, while those species produced from early PIP_2 hydrolysis are more poly-unsaturated fatty acid-containing (PUFA-containing) species.

All DAG species measured exhibit a later rise phase, peaking on average around 15 minutes. Although this second rise phase has in some cases been attributed to phospholipase D (PLD) activity [30, 81, 82], RAW 264.7 cells have been shown to exhibit no PLD activation upon stimulation by UDP (data not shown). Thus a hypothetical mechanism for the observed response is, in addition to early production from PIP_2 hydrolysis, the activation of a known DAG metabolic pathway: agonist stimulated conversion of an intracellular pool of DAG to PA followed by cytidine diphosphate-DAG (CDP-DG) production and subsequent conversion to phosphatidylinositol (PI), resulting in a transformed pool of PIP_2 from the original primarily polyunsaturated form. A schematic of this two-pool DAG model is shown in Figure 2. In this scenario DAG_{p2} is replenished by a phosphatidylcholine-specific enzyme while it is simultaneously used for PI production and replenishment of the PIP_2 pool. The revised equation for DAG produced from PIP_2 hydrolysis based on this two-pool model is similar to equation (24) but includes an additional term to account for a contribution from the second pool of DAG. We make note here that our model includes a separate DAG module for each individual species of DAG. While the form of the modules (consisting of the two equations (25) and (26) below) for each species is identical, certain rates of production and degradation are assumed to vary, thus causing differential responses among species. This change in parameters, which is dependent upon the DAG species under consideration, is noted in the equations below by parameters containing the superscript i .

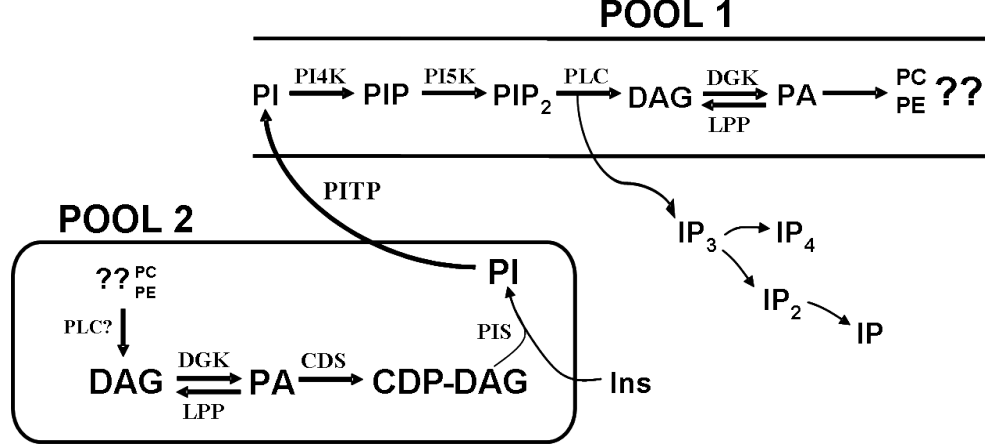


Figure 2: Proposed two-pool model for DAG kinetics post agonist stimulation with UDP. Initial production of DAG from the hydrolysis of PIP_2 in pool 1 (plasma membrane) is offset by phosphorylation of DAG by a DAG kinase in pool 2 (either in the ER or the nucleus) to aid in the PI replacement pathway. The second wave of DAG is a result of resynthesis of PIP_2 which is then hydrolyzed to form DAG and IP_3 .

The equation for DAG_{p1} of the i^{th} DAG species, denoted DAG_{p1}^i , is therefore given by

$$\frac{d[DAG_{p1}^i](t)}{dt} = k_{hyd} \left(\frac{[Ca^{2+}]}{K_c + [Ca^{2+}]} \right) \lambda N_{G^*} \left(\frac{10^6}{N_{av} \cdot v} \right) N_{PIP_2} - k_{dp1}^i [DAG_{p1}^i] + \eta^i k_{dp2}^i [DAG_{p2}^i], \quad (25)$$

where η^i denotes the fraction of DAG_{p2}^i contributing to DAG_{p1}^i , and k_{dp2}^i is the degradation rate of DAG_{p2}^i implicitly dependent on ligand concentration such that $k_{dp2}^i = 0$ when $[L] = 0$. To account for the dynamics of the second pool of DAG in the i^{th} DAG species, denoted DAG_{p2}^i , we also include the equation

$$\frac{d[DAG_{p2}^i](t)}{dt} = -k_{dp2}^i [DAG_{p2}^i] + k_{ap2}^i ([DAG_{p2}^i](0) - [DAG_{p2}^i]), \quad (26)$$

where DAGs from pool 2 are phosphorylated at a rate proportional to the current concentration of DAG_{p2} for the i^{th} DAG species and are replenished at a rate proportional to the amount of DAG_{p2}^i that has been phosphorylated by DAG kinase.

II.4 Module 4: Cytosolic Calcium dynamics

Upon receptor activation, PIP₂-derived IP₃ diffuses through the cytosol and binds to IP₃-gated Ca²⁺ channels (IP₃-Rs) on the ER, releasing Ca²⁺ into the cytosol. In the development of a model for agonist-induced cytosolic Ca²⁺ oscillations in a “closed cell” (i.e., no Ca²⁺ exchange with the extracellular medium through the plasma membrane), De Young and Keizer [16] assumed that the balance of Ca²⁺ levels is determined only by Ca²⁺ release out of the ER (mediated by the IP₃-R) and Ca²⁺ flow back into the ER (via a Ca²⁺-ATPase in the ER membrane). This model utilized the biophysical theory that the ion current through a channel is proportional to the channel’s open probability times the ion’s concentration gradient across the ER membrane when the ER membrane potential is zero [32] to develop ordinary differential equations for the IP₃-R channel gating process. Here they assumed that on each of the four subunits of the IP₃-R there exists one IP₃ binding site and two Ca²⁺ binding sites, one site for channel activation and a separate channel inactivation site. This model contained a total of nine differential equations: one Ca²⁺ balance equation, and eight equations for the channel gating kinetics (three binding sites corresponds to eight different possibilities of IP₃-R states).

By considering the different time scales of this nine-equation system along with the assumption that each of the three binding processes are independent of one another, Li and Rinzel [40] developed a simplified model of cytosolic Ca²⁺ dynamics which includes an additional term that allows for Ca²⁺ exchange between the cell and the extracellular medium, thus relaxing the “closed cell” constraints of the De Young and Keizer model. Due to the simpler form of the Li and Rinzel model as well as its ability to explain various experimental data, we have chosen to utilize this model of Ca²⁺ dynamics in our system. Thus cytosolic Ca²⁺ dynamics are modeled by the following system:

$$\begin{aligned} \frac{d[Ca^{2+}](t)}{dt} = & \left[\nu_1 m_\infty^3 (h)^3 + \nu_2 \right] \times \left[[c_0] - (1 + c_1) [Ca^{2+}] \right] \\ & - \frac{\nu_3 [Ca^{2+}]^2}{k_{er}^2 + [Ca^{2+}]^2} + \epsilon \left[j_{in} - \frac{\nu_4 [Ca^{2+}]^2}{k_{pl}^2 + [Ca^{2+}]^2} \right] \end{aligned} \quad (27)$$

$$\begin{aligned} m_\infty = & \left(\frac{[IP_3]}{[IP_3] + d_{IP_3}} \right) \left(\frac{[Ca^{2+}]}{d_{act} + [Ca^{2+}]} \right) \\ \frac{dh(t)}{dt} = & a \left([Ca^{2+}] + d_{inh} \right) \left[\left(\frac{d_{inh}}{[Ca^{2+}] + d_{inh}} \right) - h \right] \end{aligned} \quad (28)$$

$$\frac{d[c_0]}{dt} = \epsilon \left[j_{in} - \frac{\nu_4 [Ca^{2+}]^2}{k_{pl}^2 + [Ca^{2+}]^2} \right]. \quad (29)$$

Here $h(t)$ represents the fraction of IP_3 receptors not yet inactivated by Ca^{2+} binding to the inactivation site of the IP_3 -R, while m_∞ represents the probability of the IP_3 -R being in the activated (open) state, with IP_3 bound as well as Ca^{2+} bound to the activation site. Although the IP_3 -R contains four subunits, De Young and Keizer found that a power close to 3 for each of these terms provided the best fit to experimental data [16]. The c_0 term represents total free Ca^{2+} per cytosolic volume, and the parameter c_1 is the volume ratio between the ER and the cytosol.

The rate parameters ν_1 , ν_2 , ν_3 , and ν_4 are effective permeability constants for the IP_3 channels, ER membrane leakage, Ca^{2+} pumps on the ER, and Ca^{2+} flux through the plasma membrane via voltage-sensitive Ca^{2+} channels, respectively. The receptor dissociation constant for the IP_3 receptor is denoted by d_{IP_3} , while dissociation constants for the Ca^{2+} activation and deactivation sites on the IP_3 -R are d_{act} and d_{inh} , respectively, and a is the IP_3 -R binding constant for Ca^{2+} -dependent inhibition. The parameter k_{er} is the Michaelis constant for Ca^{2+} uptake from cytosol into the ER, and k_{pl} is the Michaelis constant for Ca^{2+} flux out of cell across plasma membrane. The term j_{in} , which represents the flux of Ca^{2+} through the plasma membrane and into the cell, is considered to be constant. The parameter ϵ is the ratio of the total area of the plasma membrane to the total area of the ER.

Although the modeling of Ca^{2+} was not a major emphasis of this work, its importance to the overall signaling pathway necessitates its inclusion in the model. For a

more detailed account and analysis of the role of Ca^{2+} in this pathway in RAW 264.7 cells, see Flaherty et al. [19].

II.5 Dimensionless Scaling

Dimensionless forms for the above signaling equations may be written which relate ratios of species, indicating which parameters are essential for the kinetics. We define the quantities $x_i(t)$ as given in Table 1.

Table 1: Time-dependent nondimensionalized model variables

Original Variable	Nondimensionalized Variable	Formula
$N_{RS}(t)$	$x_1(t)$	$N_{RS}(t) \div N_{RT}$
$N_{R_p^S}(t)$	$x_2(t)$	$N_{R_p^S}(t) \div N_{RT}$
$N_{G^*}(t)$	$x_3(t)$	$N_{G^*}(t) \div N_{GT}$
$N_{PIP_2}(t)$	$x_4(t)$	$N_{PIP_2}(t) \div N_{PIP_2}(t = 0)$
$[IP_3](t)$	$x_5(t)$	$[IP_3](t) \div \left[\left(\frac{10^6}{N_{av} \cdot v} \right) N_{PIP_2}(t = 0) \right]$
$[DAG_{p1}](t)$	$x_6(t)$	$[DAG_{p1}](t) \div \left[\left(\frac{10^6}{N_{av} \cdot v} \right) N_{PIP_2}(t = 0) \right]$
$[DAG_{p2}](t)$	$x_7(t)$	$[DAG_{p2}](t) \div [DAG_{p2}](t = 0)$
$[Ca^{2+}]$	$\hat{x}_8(t)$	$[Ca^{2+}] \div [Ca_T]$
h	$\hat{x}_9(t)$	h
c_0	$\hat{x}_{10}(t)$	$c_0 \div [Ca_T]$

Note that since IP_3 and DAG_{p1} originate from PIP_2 hydrolysis, they are therefore scaled by the maximum number of PIP_2 molecules, given by $N_{PIP_2}(t = 0)$. Also, the Ca^{2+} module equations are assigned a special notation, \hat{x}_i , $i = \{8, 9, 10\}$, as we will perform mathematical analysis with a simplified version of these equations. The modified parameters resulting from nondimensionalization are given in Table 2.

Table 2: Modified rate parameters for nondimensionalized system

Modified Parameter	Formula	Modified Parameter	Formula
\tilde{k}_a	$k_a N_{RT} = \left(\frac{k_a^*}{m2\mu M^a} \right) N_{RT}$	\tilde{k}_{er}	$\frac{k_{er}}{[Ca_T]}$
\tilde{k}_{hyd}	$k_{hyd} N_{GT} \lambda = \left(\frac{k_{hyd}^*}{m2\mu M^a} \right) N_{GT} \lambda$	\tilde{j}_{in}	$\frac{j_{in}}{[Ca_T]}$
ζ	$\frac{[DAG_{p2}](t=0)\eta}{(m2\mu M^a)N_{PIP_2}(t=0)}$	$\tilde{\nu}_4$	$\frac{\nu_4}{[Ca_T]}$
\tilde{K}_c	$\frac{K_c}{[Ca_T]}$	\tilde{k}_{pl}	$\frac{k_{pl}}{[Ca_T]}$
\tilde{d}_{IP_3}	$\frac{d_{IP_3}}{(m2\mu M^a)N_{PIP_2}(t=0)}$	\tilde{a}	$a [Ca_T]$
\tilde{d}_{act}	$\frac{d_{act}}{[Ca_T]}$	\tilde{d}_{inh}	$\frac{d_{inh}}{[Ca_T]}$
$\tilde{\nu}_3$	$\frac{\nu_3}{[Ca_T]}$		

${}^a m2\mu M = 10^6 / (N_{av} \cdot v)$ is a conversion factor which converts number of molecules to concentration (in μM); * denotes a rate constant in terms of concentration instead of number of molecules. (Here N_{av} is Avogadro's constant = 6.02252×10^{23} , and $v = 5 \times 10^{-13}$ is the volume of one cell in μM .)

The nondimensionalized model equations in terms of the variables listed in Table 1 and parameters in Table 2 are given in equations (30) - (39):

$$\frac{dx_1(t)}{dt} = k_r - \left(k_r + \frac{k_p [L]}{K_1 + [L]} \right) x_1 - k_r x_2 \quad (30)$$

$$\frac{dx_2(t)}{dt} = [L] \left(\frac{k_p x_1}{K_1 + [L]} - \frac{k_e x_2}{K_2 + [L]} \right) \quad (31)$$

$$\frac{dx_3(t)}{dt} = \tilde{k}_a x_1 (1 - x_3) - k_d x_3 \quad (32)$$

$$\frac{dx_4(t)}{dt} = -\tilde{k}_{hyd} \left(\frac{\hat{x}_8}{\tilde{K}_c + \hat{x}_8} \right) x_3 x_4 + k_{rep} (1 - x_4) \quad (33)$$

$$\frac{dx_5(t)}{dt} = \tilde{k}_{hyd} \left(\frac{\hat{x}_8}{\tilde{K}_c + \hat{x}_8} \right) x_3 x_4 - k_{d3} x_5 \quad (34)$$

$$\frac{dx_6(t)}{dt} = \tilde{k}_{hyd} \left(\frac{\hat{x}_8}{\tilde{K}_c + \hat{x}_8} \right) x_3 x_4 - k_{dp1} x_6 + k_{dp2} \zeta x_7 \quad (35)$$

$$\frac{dx_7(t)}{dt} = -k_{dp2} x_7 + k_{ap2} (1 - x_7) \quad (36)$$

$$\begin{aligned} \frac{d\hat{x}_8(t)}{dt} = & \left[\nu_1 \left(\frac{x_5}{x_5 + \tilde{d}_{IP_3}} \right)^3 \left(\frac{\hat{x}_8}{\hat{x}_8 + \tilde{d}_{act}} \right)^3 (\hat{x}_9)^3 + \nu_2 \right] \\ & \times (\hat{x}_{10} - (1 + c_1) \hat{x}_8) - \frac{\tilde{\nu}_3 \hat{x}_8^2}{\tilde{k}_{er}^2 + \hat{x}_8^2} + \epsilon \left[\tilde{j}_{in} - \frac{\tilde{\nu}_4 \hat{x}_8^2}{\tilde{k}_{pl}^2 + \hat{x}_8^2} \right] \end{aligned} \quad (37)$$

$$\frac{d\hat{x}_9(t)}{dt} = \tilde{a} (\hat{x}_8 + \tilde{d}_{inh}) \left[\left(\frac{\tilde{d}_{inh}}{\hat{x}_8 + \tilde{d}_{inh}} \right) - \hat{x}_9 \right] \quad (38)$$

$$\frac{d\hat{x}_{10}(t)}{dt} = \epsilon \left[\tilde{j}_{in} - \frac{\tilde{\nu}_4 \hat{x}_8^2}{\tilde{k}_{pl}^2 + \hat{x}_8^2} \right]. \quad (39)$$

II.6 Initial Conditions of the Model

With the exception of the calcium module variables, initial conditions for each model variable are chosen to reflect the levels of each variable over baseline levels prior to pathway activation. Since we assume rapid ligand binding, we set $R^S(0) = R_T$. Also, since PIP_2 and DAG_{p2} are initially at their maximum value, we have $N_{PIP_2}(0) = N_{PIP_{2T}}$ and $N_{DAG_{p2}}(0) = N_{DAG_{p2T}}$. Phosphorylated surface receptors, R_p^S , activated G-proteins, IP_3 , and DAG_{p1} are all given an initial value of zero since we assume there is no production of these molecules prior to receptor activation. While the

initial concentration of calcium, $0.0009 \mu\text{M}$, is taken from experimental data, the initial values of the remaining two calcium module variables, h and c_0 , are chosen to reflect values given by Li and Rinzel [40]. Therefore, the initial conditions for the nondimensionalized system are as follows:

$$x_1(t = 0) = 1$$

$$x_2(t = 0) = 0$$

$$x_3(t = 0) = 0$$

$$x_4(t = 0) = 1$$

$$x_5(t = 0) = 0$$

$$x_6(t = 0) = 0$$

$$x_7(t = 0) = 1$$

$$\hat{x}_8(t = 0) = 1.34 \times 10^{-4}$$

$$\hat{x}_9(t = 0) = 0.8$$

$$\hat{x}_{10}(t = 0) = 0.02985.$$

CHAPTER III

THEORETICAL MODEL ANALYSIS

III.1 Introduction

As the complexity of our model precludes an analytic solution, we make use of several known mathematical results to investigate the analytical behavior of our system of equations. First we want to ensure that our model is well-posed. Using the nondimensionalized form of the mathematical model described in the previous chapter, we thus perform a rigorous study of the existence and uniqueness of solutions to our model. Next, we turn our focus toward the asymptotic behavior of the model's solutions.

The majority of this analysis will be conducted on a simplified version of the nondimensionalized model, where the contribution of Ca^{2+} is simplified using the following fit to the experimental Ca^{2+} data shown in Section IV.2:

$$\frac{dx_8(t)}{dt} = \alpha(-\beta x_9 + \gamma x_{10}), \quad (40)$$

$$\frac{dx_9(t)}{dt} = -\beta x_9, \quad (41)$$

$$\frac{dx_{10}(t)}{dt} = -\gamma x_{10},$$

where α , β , and γ are positive constants, and x_8 denotes the simplified Ca^{2+} equation. From this system of equations, we can determine an analytic solution for $x_8(t)$, $x_9(t)$, and $x_{10}(t)$:

$$\begin{aligned} x_8(t) &= \alpha(x_9 - x_{10}) + \alpha(x_{10}(0) - x_9(0)) + x_8(0) \\ &= \alpha(e^{-\beta t} - e^{-\gamma t}) + \nu, \\ x_9(t) &= x_9(0)e^{-\beta t}, \\ x_{10}(t) &= x_{10}(0)e^{-\gamma t}, \end{aligned} \quad (42)$$

where

$$\nu = \alpha(x_{10}(0) - x_9(0)) + x_8(0).$$

Solving for $x_{10}(t)$ in the analytic solution (42) gives

$$x_{10}(t) = \frac{-x_8(t) + \nu}{\alpha} + x_9(t).$$

Substituting this equation in for x_{10} in (40) gives

$$\begin{aligned} \frac{dx_8(t)}{dt} &= \alpha \left(-\beta x_9 + \gamma \left(\frac{-x_8 + \nu}{\alpha} + x_9 \right) \right) \\ &= -\gamma x_8 + \alpha(\gamma - \beta)x_9 + \gamma\nu. \end{aligned} \quad (43)$$

This also allows us to eliminate the $x_{10}(0)$ term from the analytic solution for $x_8(t)$, so that we have

$$x_8(t) = \nu + \alpha x_9(0)(e^{-\beta t} - e^{-\gamma t}) + x_8(0)e^{-\gamma t}, \quad (44)$$

where now we set

$$\nu := \lim_{t \rightarrow \infty} x_8(t), \quad (45)$$

and we require that $\gamma > \beta$ to ensure positivity of $x_8(t)$ for all $t > 0$. We also note that the solution $x_8(t)$ remains bounded, with maximum value

$$M_8 := \frac{\ln[\gamma(\alpha x_9(0) - x_8(0))] - \ln[\alpha\beta x_9(0)]}{\gamma - \beta}. \quad (46)$$

We now use equations (41) and (43) for our mathematical analysis of the system, for a system total of nine ordinary differential equations. Although this Ca^{2+} module is a significant simplification to the original Ca^{2+} equations, it results in little effect

to the model behavior and will allow for a more thorough and detailed mathematical analysis of the system.

III.2 Existence and Uniqueness of Solutions

Using the simplified version of the nondimensionalized model, we prove local existence of solutions using the well-known results (taken from Brauer's Theorem 3.3 [8] and shown below) for systems of ordinary differential equations of the type

$$\dot{\mathbf{x}} = \mathbf{f}(t, \mathbf{x}) \quad (47)$$

such that $\mathbf{f} \in C^1$ is bounded and is Lipschitz continuous on some domain.

Theorem III.2.1. ([8], Theorem 3.3) *Let \mathbf{f} and $\partial\mathbf{f}/\partial\mathbf{x}_j$ ($j = 1, \dots, n$) be continuous on the box $\mathbf{B} = \{(t, \mathbf{x}) \mid |t - t_0| \leq a, |\mathbf{x} - \boldsymbol{\eta}| \leq b\}$, where a and b are positive numbers, and satisfying the bounds,*

$$|\mathbf{f}(t, \mathbf{x})| \leq N, \quad \left| \frac{\partial\mathbf{f}(t, \mathbf{x})}{\partial x_j} \right| \leq K \quad (j = 1, \dots, n)$$

for (t, \mathbf{x}) in \mathbf{B} . Let α be the smaller of the numbers a and b/N and define the successive approximations

$$\begin{cases} \phi_0(t) = \boldsymbol{\eta} \\ \phi_n(t) = \boldsymbol{\eta} + \int_{t_0}^t \mathbf{f}(s, \phi_{n-1}(s)) ds \end{cases}$$

Then the sequence $\{\phi_j\}$ of successive approximations converges (uniformly) on the interval $|t - t_0| \leq \alpha$ to a solution $\phi(t)$ of (47), that satisfies the initial condition $\phi(t_0) = \boldsymbol{\eta}$.

We now show that our system meets all the requirements of Theorem III.2.1 for $\boldsymbol{\eta} \geq 0$. Although we have shown that we can compute the analytic solutions of $x_8(t)$ and $x_9(t)$, we include these in our analysis for the sake of completeness. It is clear

that all f_j ($j = 1, \dots, 9$) are continuous for $x_i \geq 0$ ($i = 1, \dots, 9$). Computing the first partial derivatives, we have the following:

$$\begin{aligned}
f_1 &= \frac{dx_1(t)}{dt} = k_r - \left(k_r + \frac{k_p [L]}{K_1 + [L]} \right) x_1 - k_r x_2 & (48) \\
\Rightarrow \frac{\partial f_1}{\partial x_1} &= k_r + \left(\frac{k_p [L]}{K_1 + [L]} \right) \\
\frac{\partial f_1}{\partial x_2} &= -k_r,
\end{aligned}$$

$$\begin{aligned}
f_2 &= \frac{dx_2(t)}{dt} = [L] \left(\frac{k_p x_1}{K_1 + [L]} - \frac{k_e x_2}{K_2 + [L]} \right) & (49) \\
\Rightarrow \frac{\partial f_2}{\partial x_1} &= [L] \left(\frac{k_p}{K_1 + [L]} \right) \\
\frac{\partial f_2}{\partial x_2} &= [L] \left(-\frac{k_e}{K_2 + [L]} \right),
\end{aligned}$$

$$\begin{aligned}
f_3 &= \frac{dx_3(t)}{dt} = \tilde{k}_a x_1 (1 - x_3) - k_d x_3 & (50) \\
\Rightarrow \frac{\partial f_3}{\partial x_1} &= \tilde{k}_a (1 - x_3) \\
\frac{\partial f_3}{\partial x_3} &= -\tilde{k}_a x_1 - k_d,
\end{aligned}$$

$$\begin{aligned}
f_4 &= \frac{dx_4(t)}{dt} = -\tilde{k}_{hyd} \left(\frac{x_8}{\tilde{K}_c + x_8} \right) x_3 x_4 + k_{rep} (1 - x_4) & (51) \\
\Rightarrow \frac{\partial f_4}{\partial x_3} &= -\tilde{k}_{hyd} \left(\frac{x_8}{\tilde{K}_c + x_8} \right) x_4 \\
\frac{\partial f_4}{\partial x_4} &= -\tilde{k}_{hyd} \left(\frac{x_8}{\tilde{K}_c + x_8} \right) x_3 - k_{rep} \\
\frac{\partial f_4}{\partial x_8} &= -\tilde{k}_{hyd} \left(\frac{\tilde{K}_c}{(\tilde{K}_c + x_8)^2} \right) x_3 x_4,
\end{aligned}$$

$$\begin{aligned}
f_5 &= \frac{dx_5(t)}{dt} = \tilde{k}_{hyd} \left(\frac{x_8}{\tilde{K}_c + x_8} \right) x_3 x_4 - k_{d3} x_5 & (52) \\
\Rightarrow \frac{\partial f_5}{\partial x_3} &= \tilde{k}_{hyd} \left(\frac{x_8}{\tilde{K}_c + x_8} \right) x_4 \\
\frac{\partial f_5}{\partial x_4} &= \tilde{k}_{hyd} \left(\frac{x_8}{\tilde{K}_c + x_8} \right) x_3 \\
\frac{\partial f_5}{\partial x_5} &= -k_{d3} \\
\frac{\partial f_5}{\partial x_8} &= \tilde{k}_{hyd} \left(\frac{\tilde{K}_c}{(\tilde{K}_c + x_8)^2} \right) x_3 x_4,
\end{aligned}$$

$$\begin{aligned}
f_6 &= \frac{dx_6(t)}{dt} = \tilde{k}_{hyd} \left(\frac{x_8}{\tilde{K}_c + x_8} \right) x_3 x_4 - k_{dp1} x_6 + k_{dp2} \zeta x_7 & (53) \\
\Rightarrow \frac{\partial f_6}{\partial x_3} &= \tilde{k}_{hyd} \left(\frac{x_8}{\tilde{K}_c + x_8} \right) x_4 \\
\frac{\partial f_6}{\partial x_4} &= \tilde{k}_{hyd} \left(\frac{x_8}{\tilde{K}_c + x_8} \right) x_3 \\
\frac{\partial f_6}{\partial x_6} &= -k_{dp1} \\
\frac{\partial f_6}{\partial x_7} &= k_{dp2} \zeta \\
\frac{\partial f_6}{\partial x_8} &= \tilde{k}_{hyd} \left(\frac{\tilde{K}_c}{(\tilde{K}_c + x_8)^2} \right) x_3 x_4,
\end{aligned}$$

$$\begin{aligned}
f_7 &= \frac{dx_7(t)}{dt} = -k_{dp2} x_7 + k_{ap2} (1 - x_7) & (54) \\
\Rightarrow \frac{\partial f_7}{\partial x_7} &= -k_{dp2} - k_{ap2},
\end{aligned}$$

$$\begin{aligned}
f_8 &= \frac{dx_8(t)}{dt} = -\gamma x_8 + \alpha(\gamma - \beta)x_9 + \gamma\nu & (55) \\
\Rightarrow \frac{\partial f_8}{\partial x_8} &= -\gamma \\
\frac{\partial f_8}{\partial x_9} &= \alpha(\gamma - \beta),
\end{aligned}$$

$$\begin{aligned}
f_9 &= \frac{dx_9(t)}{dt} = -\beta x_9 & (56) \\
\Rightarrow \frac{\partial f_9}{\partial x_9} &= -\beta.
\end{aligned}$$

Although our initial analysis will only use information from f_8 and f_9 , the original equations for Ca^{2+} also satisfy the hypotheses of Theorem III.2.1, as shown below:

$$\begin{aligned}
\hat{f}_8 &= \frac{d\hat{x}_8(t)}{dt} = \left[\nu_1 \left(\frac{x_5}{x_5 + \tilde{d}_{IP_3}} \right)^3 \left(\frac{\hat{x}_8}{\hat{x}_8 + \tilde{d}_{act}} \right) (\hat{x}_9)^3 + \nu_2 \right] \\
&\quad \times (\hat{x}_{10} - (1 + c_1) \hat{x}_8) - \frac{\tilde{\nu}_3 \hat{x}_8^2}{\tilde{k}_{er}^2 + \hat{x}_8^2} + \epsilon \left[\tilde{j}_{in} - \frac{\tilde{\nu}_4 \hat{x}_8^2}{\tilde{k}_{pl}^2 + \hat{x}_8^2} \right] \\
\Rightarrow \frac{\partial \hat{f}_8}{\partial x_5} &= 3\nu_1 \left(\frac{x_5}{x_5 + \tilde{d}_{IP_3}} \right)^2 \left(\frac{\tilde{d}_{IP_3}}{(x_5 + \tilde{d}_{IP_3})^2} \right) \left(\frac{\hat{x}_8}{\hat{x}_8 + \tilde{d}_{act}} \right) (\hat{x}_9)^3 \\
&\quad \times (\hat{x}_{10} - (1 + c_1) \hat{x}_8) \\
\frac{\partial \hat{f}_8}{\partial \hat{x}_8} &= \nu_1 \left(\frac{x_5}{x_5 + \tilde{d}_{IP_3}} \right)^3 \left(\frac{\tilde{d}_{act}}{(\hat{x}_8 + \tilde{d}_{act})^2} \right) (\hat{x}_9)^3 (\hat{x}_{10} - (1 + c_1) \hat{x}_8) \\
&\quad - \left[\nu_1 \left(\frac{x_5}{x_5 + \tilde{d}_{IP_3}} \right)^3 \left(\frac{\hat{x}_8}{\hat{x}_8 + \tilde{d}_{act}} \right) (\hat{x}_9)^3 + \nu_2 \right] (1 + c_1) \\
&\quad - \frac{2\tilde{\nu}_3 \tilde{k}_{er}^2 \hat{x}_8}{(\tilde{k}_{er}^2 + \hat{x}_8^2)^2} + \frac{2\epsilon \tilde{\nu}_4 \tilde{k}_{pl}^2 \hat{x}_8}{(\tilde{k}_{pl}^2 + \hat{x}_8^2)^2} \\
\frac{\partial \hat{f}_8}{\partial \hat{x}_9} &= 3\nu_1 \left(\frac{x_5}{x_5 + \tilde{d}_{IP_3}} \right)^3 \left(\frac{\hat{x}_8}{\hat{x}_8 + \tilde{d}_{act}} \right) (\hat{x}_9)^2 \\
&\quad \times (\hat{x}_{10} - (1 + c_1) \hat{x}_8) \\
\frac{\partial \hat{f}_8}{\partial \hat{x}_9} &= \nu_1 \left(\frac{x_5}{x_5 + \tilde{d}_{IP_3}} \right)^3 \left(\frac{\hat{x}_8}{\hat{x}_8 + \tilde{d}_{act}} \right) (\hat{x}_9)^3 + \nu_2,
\end{aligned} \tag{57}$$

$$\begin{aligned}
\hat{f}_9 &= \frac{d\hat{x}_9(t)}{dt} = \tilde{a} (\hat{x}_8 + \tilde{d}_{inh}) \left[\left(\frac{\tilde{d}_{inh}}{\hat{x}_8 + \tilde{d}_{inh}} \right) - \hat{x}_9 \right] \\
\Rightarrow \frac{\partial \hat{f}_9}{\partial \hat{x}_8} &= \tilde{a} \left[\left(\frac{\tilde{d}_{inh}}{\hat{x}_8 + \tilde{d}_{inh}} \right) - \hat{x}_9 \right] + \tilde{a} (\hat{x}_8 + \tilde{d}_{inh}) \left(\frac{-\tilde{d}_{inh}}{(\hat{x}_8 + \tilde{d}_{inh})^2} \right) \\
\frac{\partial \hat{f}_9}{\partial \hat{x}_9} &= -\tilde{a} (\hat{x}_8 + \tilde{d}_{inh}),
\end{aligned} \tag{58}$$

$$\begin{aligned}
\hat{f}_{10} &= \frac{d\hat{x}_{10}(t)}{dt} = \epsilon \left[\tilde{j}_{in} - \frac{\tilde{\nu}_4 \hat{x}_8^2}{\tilde{k}_{pl}^2 + \hat{x}_8^2} \right] \\
\Rightarrow \frac{\partial \hat{f}_{10}}{\partial \hat{x}_8} &= \frac{2\epsilon \tilde{\nu}_4 \tilde{k}_{pl}^2 \hat{x}_8}{(\tilde{k}_{pl}^2 + \hat{x}_8^2)^2}.
\end{aligned} \tag{59}$$

All other partial derivatives equal zero. From equations (48) - (56), we see that all partial derivatives are continuous in all of \mathbb{R}_+^9 , where $\mathbb{R}_+^9 = \{\mathbf{x} \in \mathbb{R}^9 \mid x_i \geq 0 \forall i = 1, \dots, 9\}$, since all rate constants are positive. In particular, each f_i and all of its partial derivatives are continuous on $[0, \mathbf{M}]$ such that $1 \leq M_i < \infty$ for $i \in \{1, \dots, 9\}$, where, as we will show in Propositions III.2.1 and III.2.2, each x_i ($i = 1, \dots, 9$) is bounded. Therefore, this guarantees the existence of a solution $\phi(t)$ of our system (47) which is defined on the interval $|t - t_0| \leq \alpha$ and satisfies the initial condition $\phi(t_0) = \boldsymbol{\eta}$. Here α is the smaller of a and b/N as defined in the statement of Theorem III.2.1.

According to Brauer's Theorem 3.4 [8] stated below, this solution ϕ is the unique solution satisfying the initial condition

$$\phi(t_0) = \boldsymbol{\eta}. \tag{60}$$

Theorem III.2.2. ([8], Theorem 3.4) *Suppose \mathbf{f} and $\partial \mathbf{f} / \partial \mathbf{y}_j$ ($j = 1, \dots, n$) are continuous on the "box"*

$$\mathbf{B} = \{(t, \mathbf{y}) \mid |t - t_0| \leq a, |\mathbf{y} - \boldsymbol{\eta}| \leq b\}.$$

Then there exists at most one solution of (47) satisfying the initial condition (60).

Now let $D = \{(t, \mathbf{x}) \in \mathbb{R}^{10} \mid t \geq 0, 0 \leq x_i \leq 1 \text{ for } i \in \{1, 2, 3, 4, 7\}, \text{ with } x_1 + x_2 \leq 1, \text{ and } 0 \leq x_j \leq M_j \text{ for } j \in \{5, 6, 8, 9\} \text{ and } 0 < M_j < \infty\}$. We note that from (42) and (44), we have $M_9 = x_9(0) > 0$, and M_8 is given by equation (46). Since our system satisfies the hypotheses of Theorems III.2.1 and III.2.2 on D , we know a local solution exists for any initial condition vector $\boldsymbol{\eta}$ in D on some interval $[0, t(\boldsymbol{\eta})]$, where, as we have indicated notationally, this interval is dependent on the initial condition vector $\boldsymbol{\eta}$. We let $[0, t_{max}(\boldsymbol{\eta})]$, where $0 < t_{max}(\boldsymbol{\eta}) \leq \infty$, be the maximal interval of existence, and we will show that in fact $t_{max}(\boldsymbol{\eta}) = \infty$ in Proposition III.2.3.

In order to find solutions to our system of nondimensionalized equations in the region of biological interest, we must have that all solutions $x_i(t), i = (0, \dots, 9)$, are positive and remain bounded for all $t \in (0, t_{max}(\boldsymbol{\eta}))$. In other words, we want to show that D is *positively invariant*, so that all solutions with initial conditions in D remain in D for all $t \in [0, t_{max}(\boldsymbol{\eta})]$. As we have already shown that $x_8(t)$ and $x_9(t)$ meet these criteria, we now verify that the remaining equations in our system satisfy these requirements. From the receptor conservation equation (8), we are only interested in solutions for the receptor module on the closed set

$$\hat{D} = \{x_1, x_2 \in \mathbb{R} \mid x_1, x_2 \geq 0 \text{ and } x_1 + x_2 \leq 1\}. \quad (61)$$

We make use of the following results of Amann [1]:

Theorem III.2.3. ([1], Theorem 16.5) *Let $\hat{D} \subseteq \mathbb{R}^2$ be closed. Then \hat{D} is positively invariant if and only if for every $x \in \hat{D}$, the subtangent condition*

$$\liminf_{h \rightarrow 0^+} \frac{1}{h} \text{dist}(x + hF(x); \hat{D}) = 0 \quad (62)$$

is satisfied.

Therefore, we need to show that the subtangent condition (62) holds for points on the boundary of \hat{D} defined in (61) since it is straightforward to show this condition is met on interior points of \hat{D} . We verify this condition in Proposition III.2.1.

Proposition III.2.1. *Let $\eta_1, \eta_2 \in \hat{D}$. If $t \in (0, t_{max}(\boldsymbol{\eta}))$, then $x_1(t), x_2(t) \in \hat{D}$.*

Proof. We consider three cases: **A:** $x_1 + x_2 = 1$ and $0 < x_2 < 1$, **B:** $0 \leq x_1 \leq 1$ and $x_2 = 0$, and **C:** $0 \leq x_2 \leq 1$ and $x_1 = 0$, with

$$\mathbf{F} \left(\begin{pmatrix} x_1 \\ x_2 \end{pmatrix} \right) = \begin{bmatrix} k_r(1 - x_1 - x_2) - c_1 x_1 \\ c_1 x_1 - c_2 x_2 \end{bmatrix},$$

where \mathbf{F} is defined as in equations (48) and (49), and we have simplified the right hand sides of these equations by setting

$$c_1 = \frac{k_p[L]}{K_1 + [L]} \quad \text{and} \quad c_2 = \frac{k_e[L]}{K_2 + [L]}. \quad (63)$$

Case A: For $x_1 + x_2 = 1$ and $0 < x_2 < 1$, we have

$$\begin{aligned} \text{dist} \left((\mathbf{I} + h\mathbf{F}) \begin{bmatrix} x_1 \\ x_2 \end{bmatrix}, \hat{D} \right) &= \text{dist} \left(\begin{bmatrix} x_1 \\ x_2 \end{bmatrix} + h \begin{bmatrix} -c_1 x_1 \\ c_1 x_1 - c_2 x_2 \end{bmatrix}, \hat{D} \right) \\ &= \text{dist} \left(\begin{bmatrix} (1 - hc_1) x_1 \\ hc_1 x_1 + (1 - hc_2) x_2 \end{bmatrix}, \hat{D} \right) \\ &= \text{dist} \left(\begin{bmatrix} (1 - hc_1) x_1 \\ (1 - h(c_1 + c_2)) x_2 + hc_1 \end{bmatrix}, \hat{D} \right). \end{aligned}$$

Now for h sufficiently small, note that

$$\begin{aligned} 0 &< ((\mathbf{I} + h\mathbf{F})\mathbf{x})_1 = (1 - hc_1) x_1 < 1, \\ 0 &< ((\mathbf{I} + h\mathbf{F})\mathbf{x})_2 = (1 - h(c_1 + c_2)) x_2 + hc_1 < 1, \end{aligned}$$

and also

$$\begin{aligned} ((\mathbf{I} + h\mathbf{F})\mathbf{x})_1 + ((\mathbf{I} + h\mathbf{F})\mathbf{x})_2 &= (1 - hc_1) x_1 + hc_1 x_1 + (1 - hc_2) x_2 \\ &= x_1 + x_2 - hc_2 x_2 = 1 - hc_2 x_2 < 1. \end{aligned}$$

Therefore, for h sufficiently small, we have $(\mathbf{I} + h\mathbf{F})\mathbf{x} \in \hat{D}$, giving the required sub-tangent condition and thus ensuring that solutions $x_1(t)$ and $x_2(t)$ remain in \hat{D} .

Case B: For $0 \leq x_1 \leq 1$ and $x_2 = 0$, we have

$$\begin{aligned} \text{dist} \left((\mathbf{I} + h\mathbf{F}) \begin{bmatrix} x_1 \\ x_2 \end{bmatrix}, \hat{D} \right) &= \text{dist} \left(\begin{bmatrix} x_1 \\ x_2 \end{bmatrix} + h \begin{bmatrix} k_r(1 - x_1) - c_1 x_1 \\ c_1 x_1 \end{bmatrix}, \hat{D} \right) \\ &= \text{dist} \left(\begin{bmatrix} (1 - h(k_r + c_1)) x_1 + hk_r \\ hc_1 x_1 \end{bmatrix}, \hat{D} \right). \end{aligned}$$

For h sufficiently small, we have

$$\begin{aligned} 0 &< ((\mathbf{I} + h\mathbf{F})\mathbf{x})_1 = (1 - h(k_r + c_1)) x_1 + hk_r < 1, \\ 0 &\leq ((\mathbf{I} + h\mathbf{F})\mathbf{x})_2 = hc_1 x_1 < 1, \end{aligned}$$

and also

$$\begin{aligned} ((\mathbf{I} + h\mathbf{F})\mathbf{x})_1 + ((\mathbf{I} + h\mathbf{F})\mathbf{x})_2 &= (1 - h(k_r + c_1)) x_1 + hk_r + hc_1 x_1 < 1 \\ &= (1 - hk_r)x_1 + hk_r \leq 1. \end{aligned}$$

For h sufficiently small this gives $(\mathbf{I} + h\mathbf{F})\mathbf{x} \in \hat{D}$, so that **(62)** is satisfied.

Case C: For $0 \leq x_2 \leq 1$ and $x_1 = 0$, we have

$$\begin{aligned} \text{dist} \left((\mathbf{I} + h\mathbf{F}) \begin{bmatrix} x_1 \\ x_2 \end{bmatrix}, \hat{D} \right) &= \text{dist} \left(\begin{bmatrix} x_1 \\ x_2 \end{bmatrix} + h \begin{bmatrix} k_r(1 - x_2) \\ -c_2 x_2 \end{bmatrix}, \hat{D} \right) \\ &= \text{dist} \left(\begin{bmatrix} hk_r(1 - x_2) \\ (1 - hc_2) x_2 \end{bmatrix}, \hat{D} \right). \end{aligned}$$

Once again, for h sufficiently small, we have

$$\begin{aligned} 0 &< ((\mathbf{I} + h\mathbf{F})\mathbf{x})_1 = hk_r(1 - x_2) < 1, \\ 0 &\leq ((\mathbf{I} + h\mathbf{F})\mathbf{x})_2 = (1 - hc_2) x_2 < 1, \end{aligned}$$

and also

$$((\mathbf{I} + h\mathbf{F})\mathbf{x})_1 + ((\mathbf{I} + h\mathbf{F})\mathbf{x})_2 = hk_r(1 - x_2) + (1 - hc_2) x_2 < 1.$$

For such small h we have $(\mathbf{I} + h\mathbf{F})\mathbf{x} \in \hat{D}$, so that again (62) holds. Therefore, we have that the subtangent condition from Theorem III.2.3 is satisfied for all three cases **A**, **B**, and **C**, ensuring that $x_1(t)$ and $x_2(t)$ remain in \hat{D} for all $t \in (0, t_{max}(\boldsymbol{\eta}))$. ■

In Proposition III.2.2, we prove positivity and boundedness for the remaining equations $x_i(t)$ for $i \in \{3, \dots, 7\}$, and we also extend the result of Proposition III.2.1 to show that $0 < x_1(t), x_2(t) < 1$ and therefore $x_1(t), x_2(t) \in \text{int}(\hat{D})$ for all $t \in (0, t_{max}(\boldsymbol{\eta}))$, a result needed for proving global existence of a unique solution.

Proposition III.2.2. *Let $\boldsymbol{\eta} \in \text{int}(D)$. If $t \in (0, t_{max}(\boldsymbol{\eta}))$, then $0 < x_i(t) < M_i$ for $i = \{1, \dots, 7\}$, with $M = (1, 1, 1, 1, M_5, M_6, 1)$.*

Proof. For the sake of contradiction, assume there exists some $t_i^* \in (0, t_{max}(\boldsymbol{\eta}))$ such that one of two possibilities occurs for each $i \in \{1, \dots, 7\}$: $x_i(t_i^*) \geq M_i$ or $x_i(t_i^*) \leq 0$.

Suppose $x_i(t_i^*) \geq M_i$ for some $t_i^* \in (0, t_{max}(\boldsymbol{\eta}))$. Define $\hat{t}_i := \inf \{t \in [0, t_{max}(\boldsymbol{\eta})) \mid x_i(t) \geq M_i\}$, and therefore

$$\lim_{t \rightarrow \hat{t}_i} x_i(t) = M_i.$$

We wish to verify that for each x_i , this gives

$$\lim_{t \rightarrow \hat{t}_i} \frac{dx_i(t)}{dt} < 0.$$

If this inequality holds, using the fact that $dx_i(t)/dt$ is continuous on $(0, \hat{t}_i)$ and $dx_i(\hat{t}_i)/dt < 0$, we can find a $\delta > 0$ so that

$$\frac{dx_i(t)}{dt} < 0, \quad \text{for } t \in (\hat{t}_i - \delta, \hat{t}_i). \quad (64)$$

By the Fundamental Theorem of Calculus and equation (64),

$$x_i(\hat{t}_i) - x_i(\tau_i) = \int_{\tau_i}^{\hat{t}_i} x_i'(t) dt < 0.$$

Therefore, $x_i(\hat{t}_i) < x_i(\tau_i) < M_i$ for $\tau_i \in (\hat{t}_i - \delta, \hat{t}_i)$, which contradicts the definition of \hat{t}_i , therefore proving that we must have $x_i(t) < M_i$ for $t \in (0, t_{max}(\boldsymbol{\eta}))$.

Now to show $x_i(t) > 0$ for $t \in (0, t_{max}(\boldsymbol{\eta}))$, we again proceed by method of contradiction. Suppose $x_i(t_i^*) \leq 0$ for some $t_i^* \in (0, t_{max}(\boldsymbol{\eta}))$. Define $\tilde{t}_i := \inf \{t \in [0, t_{max}(\boldsymbol{\eta})) \mid x_i(t) \leq 0\}$, and therefore

$$\lim_{t \rightarrow \tilde{t}_i} x_i(t) = 0.$$

If we can show

$$\lim_{t \rightarrow \tilde{t}_i} \frac{dx_i(t)}{dt} > 0,$$

we again reach a contradiction by using continuity of the derivative along with the Fundamental Theorem of Calculus, thereby proving that in fact we must have $x_i(t) > 0$ for $t \in (0, t_{max}(\boldsymbol{\eta}))$.

Therefore, by considering each x_i as a separate case, we need only show that for each x_i

$$\lim_{t \rightarrow \hat{t}_i} \frac{dx_i(t)}{dt} < 0 \quad \text{and} \quad \lim_{t \rightarrow \tilde{t}_i} \frac{dx_i(t)}{dt} > 0,$$

where \hat{t}_i and \tilde{t}_i are defined above.

Case A: By continuity, there exists a t_0 such that $0 < x_1(t), x_2(t) < 1$ for $0 \leq t \leq t_0$ for $\eta_1, \eta_2 \in \text{Int}(D)$. Stipulations for η_1 and η_2 on the boundary of D are discussed at the end of Case A.

From equation (31), we have

$$\lim_{t \rightarrow \hat{t}_2} \frac{dx_2(t)}{dt} = \lim_{t \rightarrow \hat{t}_2} \left[[L] \left(\frac{k_p x_1}{K_1 + [L]} - \frac{k_e}{K_2 + [L]} \right) \right] < 0$$

since, from Proposition III.2.1, $x_1(t) + x_2(t) \leq 1$ for all $t \in [0, t_{max}(\boldsymbol{\eta})]$, which implies here that

$$\lim_{t \rightarrow \hat{t}_2} x_1(t) \leq 0,$$

proving, by the comments above, that we must have $x_2(t) < 1$ for $t \in (0, t_{max}(\boldsymbol{\eta}))$.

From equation (30), we also have

$$\lim_{t \rightarrow \hat{t}_1} \frac{dx_1(t)}{dt} = k_r - k_r \left[\lim_{t \rightarrow \hat{t}_1} x_2(t) \right] > 0$$

since, from above, $x_2(t) < 1$ for all $t \in (0, t_{max}(\boldsymbol{\eta}))$. This shows that $x_1(t) > 0$ for $t \in (0, t_{max}(\boldsymbol{\eta}))$.

Next, from equation (31), we have

$$\lim_{t \rightarrow \hat{t}_2} \frac{dx_2(t)}{dt} = \lim_{t \rightarrow \hat{t}_2} \left[[L] \left(\frac{k_p x_1(t)}{K_1 + [L]} \right) \right] > 0$$

since, from above, $x_1(t) > 0$ for all $t \in (0, t_{max}(\boldsymbol{\eta}))$. This proves that $x_2(t) > 0$ for $t \in (0, t_{max}(\boldsymbol{\eta}))$.

Finally, from equation (30), we have

$$\lim_{t \rightarrow \hat{t}_1} \frac{dx_1(t)}{dt} = k_r - \left(k_r + \frac{k_p [L]}{K_1 + [L]} \right) - k_r \left[\lim_{t \rightarrow \hat{t}_1} x_2(t) \right] < 0$$

since, from above, $x_2(t) > 0$ for all $t \in (0, t_{max}(\boldsymbol{\eta}))$. Therefore, we have that $x_1(t) < 1$ for $t \in (0, t_{max}(\boldsymbol{\eta}))$.

Note that for $\eta_1 = 1$ we have that $dx_1(t)/dt|_{t=0} < 0$ as long as $\eta_2 \geq 0$ and for $\eta_2 = 0$ we have that $dx_2(t)/dt|_{t=0} > 0$ as long as $\eta_1 > 0$. Furthermore, for $\eta_1 = 0$ we have

that $dx_1(t)/dt|_{t=0} > 0$ as long as $\eta_2 < 1$, and for $\eta_2 = 1$ we have that $dx_2(t)/dt|_{t=0} < 0$ when $\eta_1 = 0$. Therefore, by continuity of $dx_1(t)/dt$ and $dx_2(t)/dt$, each one of these initial conditions ensures the existence of a t_0 such that $0 < x_1(t), x_2(t) < 1$ for $0 \leq t \leq t_0$. The same arguments as mentioned above can then be used to show that $x_1(t)$ and $x_2(t)$ will remain in $Int(D)$ for any of these initial conditions. We do not consider initial conditions which violate the conservation equation (8).

Case B: There exists a t_0 such that $0 < x_3(t) < 1$ for $0 \leq t \leq t_0$ for the following initial conditions: $\eta_3 \in Int(D)$ by continuity; $\eta_3 = 0$ with $\eta_1 > 0$, since this gives $dx_3(t)/dt|_{t=0} > 0$; and $\eta_3 = 1$ since this gives $dx_3(t)/dt|_{t=0} < 0$ and $dx_3(t)/dt$ is continuous in D. Also, by (32),

$$\lim_{t \rightarrow \hat{t}_3} \frac{dx_3(t)}{dt} = -k_d < 0 \quad \text{and} \quad \lim_{t \rightarrow \hat{t}_3} \frac{dx_3(t)}{dt} = \lim_{t \rightarrow \hat{t}_3} [\tilde{k}_a x_1(t)] > 0$$

since from Case A, $x_1(t) > 0$ for $t \in (0, t_{max}(\boldsymbol{\eta}))$. Therefore, we have that $0 < x_3(t) < 1$ for $t \in (0, t_{max}(\boldsymbol{\eta}))$.

Case C: There exists a t_0 such that $0 < x_4(t) < 1$ for $0 \leq t \leq t_0$ for the following initial conditions: $\eta_4 \in Int(D)$ by continuity; $\eta_4 = 1$ with $\eta_3, \eta_8 > 0$, since this gives $dx_4(t)/dt|_{t=0} < 0$ (in fact, we can also have $\eta_4 = 1$ and $\eta_3 = 0$ since $dx_3(t)/dt|_{t=0} > 0$ for $\eta_3 = 0$, which implies the existence of a t_0 such that $0 < x_3(t) < 1$ for $0 \leq t \leq t_0$, and therefore $dx_4(t)/dt > 0$ on this interval); and $\eta_4 = 0$ since this gives $dx_4(t)/dt|_{t=0} > 0$ and $dx_4(t)/dt$ is continuous in D. Also, by (33),

$$\lim_{t \rightarrow \hat{t}_4} \frac{dx_4(t)}{dt} = \lim_{t \rightarrow \hat{t}_4} \left[-\tilde{k}_{hyd} \left(\frac{x_8(t)}{\tilde{K}_c + x_8(t)} \right) x_3(t) \right] < 0$$

since $0 < x_8(t) < 1$ always, and $0 < x_3(t) < 1$ from Case B. Furthermore,

$$\lim_{t \rightarrow \hat{t}_4} \frac{dx_4(t)}{dt} = k_{rep} > 0,$$

so that we have $0 < x_4(t) < 1$ for $t \in (0, t_{max}(\boldsymbol{\eta}))$.

Case D: There exists a t_0 such that $0 < x_7(t) < 1$ for $0 \leq t \leq t_0$ for the following initial conditions: $\eta_7 \in \text{Int}(D)$ by continuity; $\eta_7 = 0$, since this gives $dx_7(t)/dt|_{t=0} > 0$; and $\eta_7 = 1$ since this gives $dx_7(t)/dt|_{t=0} < 0$ and $dx_7(t)/dt$ is continuous in D. Also, by (36),

$$\lim_{t \rightarrow \hat{t}_1} \frac{dx_7(t)}{dt} = -k_{dp2} < 0 \quad \text{and} \quad \lim_{t \rightarrow \hat{t}_0} \frac{dx_7(t)}{dt} = \tilde{k}_{ap2} > 0.$$

Therefore, we have that $0 < x_7(t) < 1$ for $t \in (0, t_{max}(\boldsymbol{\eta}))$.

Case E: There exists a t_0 such that $0 < x_5(t) < M_5$ for $0 \leq t \leq t_0$ for the following initial conditions: $\eta_5 \in \text{Int}(D)$ by continuity; $\eta_5 = 0$ with $\eta_3, \eta_4, \eta_8 > 0$, since this gives $dx_5(t)/dt|_{t=0} > 0$ (for the same reason as in Case C, we can also have $\eta_5 = 0$ with $\eta_3 = 0$ as well as $\eta_4 = 0$, where we keep the condition $\eta_8 > 0$). Now from (34),

$$\lim_{t \rightarrow \hat{t}_5} \frac{dx_5(t)}{dt} = \lim_{t \rightarrow \hat{t}_5} \left[\tilde{k}_{hyd} \left(\frac{x_8(t)}{\tilde{K}_c + x_8(t)} \right) x_3(t) x_4(t) \right] > 0$$

since, by definition, $0 < x_8(t) < 1$ always, and $0 < x_3(t), x_4(t) < 1$ from Cases B and C, ensuring that $x_5(t) > 0$ for $t \in (0, t_{max}(\boldsymbol{\eta}))$. Taking $M_5 > \tilde{k}_{hyd}/k_{d3}$, we also have

$$\lim_{t \rightarrow \hat{t}_5} \frac{dx_5(t)}{dt} = \lim_{t \rightarrow \hat{t}_5} \left[\tilde{k}_{hyd} \left(\frac{x_8(t)}{\tilde{K}_c + x_8(t)} \right) x_3(t) x_4(t) \right] - k_{d3}M_5 \leq \tilde{k}_{hyd} - k_{d3}M_5 < 0,$$

which gives a contradiction. Therefore, we now have $0 < x_5(t) < M_5$ for $t \in (0, t_{max}(\boldsymbol{\eta}))$.

Case F: This case is very similar to Case E, as $x_5(t)$ and $x_6(t)$ are produced stoichiometrically from $x_4(t)$. Indeed, there exists a t_0 such that $0 < x_6(t) < M_6$ for $0 \leq t \leq t_0$ for the following initial conditions: $\eta_6 \in \text{Int}(D)$ by continuity; and, for the same reasons as in Case E, $\eta_6 = 0$ with $\eta_3, \eta_4, \eta_7 \geq 0$ and $\eta_8 > 0$, since this gives $dx_6(t)/dt > 0$ on an interval $0 \leq t \leq t_0$. Now from (35),

$$\lim_{t \rightarrow \hat{t}_6} \frac{dx_6(t)}{dt} = \lim_{t \rightarrow \hat{t}_6} \left[\tilde{k}_{hyd} \left(\frac{x_8(t)}{\tilde{K}_c + x_8(t)} \right) x_3(t) x_4(t) + k_{dp2}\zeta x_7(t) \right] > 0$$

from the remarks given in Case E, and since $0 < x_7(t) < 1$ from Case D. Thus, we have $x_6(t) > 0$ for $t \in (0, t_{max}(\boldsymbol{\eta}))$. Now taking $M_6 > (\tilde{k}_{hyd} + k_{dp2}\zeta)/k_{dp1}$, we have

$$\begin{aligned} \lim_{t \rightarrow \hat{t}_6} \frac{dx_6(t)}{dt} &= \lim_{t \rightarrow \hat{t}_6} \left[\tilde{k}_{hyd} \left(\frac{x_8(t)}{\tilde{K}_c + x_8(t)} \right) x_3(t) x_4(t) + k_{dp2}\zeta x_7(t) \right] - k_{dp1}M_6 \\ &\leq \tilde{k}_{hyd} + k_{dp2}\zeta - k_{dp1}M_6 < 0, \end{aligned}$$

which gives a contradiction. Therefore, we now have $0 < x_6(t) < M_6$ for $t \in (0, t_{max}(\boldsymbol{\eta}))$. ■

We now use Brauer's Theorem 3.6 stated below to obtain the unique continuation of our solution.

Theorem III.2.4. ([8], Theorem 3.6) *Suppose that \mathbf{f} and $\partial\mathbf{f}/\partial\mathbf{x}_j$ ($j = 1, \dots, n$) are continuous in a given region D and suppose \mathbf{f} is bounded on D . Let $(t_0, \boldsymbol{\eta})$ be a given point of D . Then the unique solution $\boldsymbol{\phi}$ of the system $\dot{\mathbf{x}} = \mathbf{f}(t, \mathbf{x})$ passing through the point $(t_0, \boldsymbol{\eta})$ can be extended until its graph meets the boundary of D .*

Proposition III.2.3. *For $\boldsymbol{\eta} \in \text{Int}(D)$ and for the special cases of $\eta_i, i \in \{1, \dots, 7\}$ discussed in Propositions III.2.1 and III.2.2, $t_{max}(\boldsymbol{\eta}) = \infty$.*

Proof. We have established continuity of our system \mathbf{f} and $\partial\mathbf{f}/\partial\mathbf{x}_j$ ($j = 1, \dots, 9$) on $D = \{(t, \mathbf{x}) \in \mathbb{R}^{10} \mid t \geq 0, 0 \leq x_i \leq 1 \text{ for } i \in \{1, 2, 3, 4, 7\}, \text{ with } x_1 + x_2 \leq 1, \text{ and } 0 \leq x_j \leq M_j \text{ for } j \in \{5, 6, 8, 9\} \text{ and } 0 < M_j < \infty\}$. Since D is closed, \mathbf{f} is also bounded on D . Therefore, for $\boldsymbol{\eta}$ satisfying the conditions in Propositions III.2.1 and III.2.2, by Theorem III.2.4, the unique solution $\boldsymbol{\phi}$ of our system $\dot{\mathbf{x}} = \mathbf{f}(t, \mathbf{x})$ passing through the point $(t_0, \boldsymbol{\eta})$ can be extended until its graph meets the boundary of D . Since we have established that for these such $\boldsymbol{\eta}$, $\boldsymbol{\phi}$ remains in $\text{Int}(D)$, we must have $t_{max}(\boldsymbol{\eta}) = \infty$. ■

We have thus established the global existence of a unique solution to our system given by equations (30) - (36), (41), and equation (43).

III.3 Steady-State Solution

The steady state solutions for our simplified system can be found by setting the right hand side of the system equal to zero. Therefore, for the receptor module (equations (30) and (31)), we have

$$\frac{dx_1}{dt} = \frac{dx_2}{dt} = 0$$

implies

$$k_r - \left(k_r + \frac{k_p [L]}{K_1 + [L]} \right) x_1 - k_r x_2 = 0$$

and

$$\left(\frac{k_p x_1}{K_1 + [L]} - \frac{k_e x_2}{K_2 + [L]} \right) = 0. \quad (65)$$

Solving for x_2 in equation (65) we have

$$\begin{aligned} \frac{k_p x_1}{K_1 + [L]} &= \frac{k_e x_2}{K_2 + [L]} \\ \Rightarrow x_2 &= \frac{k_p}{k_e} \left(\frac{K_2 + [L]}{K_1 + [L]} \right) x_1. \end{aligned}$$

Substituting this value of x_2 in for x_1 in equation (65) and simplifying gives

$$\begin{aligned} k_r - \left(k_r + \frac{k_p [L]}{K_1 + [L]} \right) x_1 - \frac{k_r k_p}{k_e} \left(\frac{K_2 + [L]}{K_1 + [L]} \right) x_1 &= 0 \\ \Rightarrow k_r k_e &= \left(k_r k_e + \frac{k_p [k_e [L] + k_r (K_2 + [L])]}{K_1 + [L]} \right) x_1 \\ \Rightarrow x_1 &= \frac{k_r k_e (K_1 + [L])}{k_r k_e (K_1 + [L]) + k_p [k_e [L] + k_r (K_2 + [L])]} \end{aligned} \quad (66)$$

Next we substitute this value of x_1 into equation (65) and simplify to obtain

$$x_2 = \left[\frac{k_r k_p (K_2 + [L])}{k_r k_e (K_1 + [L]) + k_p [k_e [L] + k_r (K_2 + [L])]} \right]. \quad (67)$$

These two values can be interpreted as the percentage of phosphorylated (in equation (67)) and unphosphorylated (in equation (66)) surface receptors remaining after the ligand concentration has been held fixed for a long period of time. For future reference, we set ξ_1 and ξ_2 to be the steady-state values of x_1 and x_2 , respectively. The steady-state number of molecules for the two groups of surface receptors is found by multiplying ξ_1 and ξ_2 by N_{RT} . We can now determine the equilibrium number of surface receptors $N_{R_E^S}$ by setting

$$\begin{aligned} N_{R_E^S} &= \lim_{t \rightarrow \infty} (N_{R^S} + N_{R_p^S}) = (\xi_1 + \xi_2) N_{RT} \\ &= \frac{k_r k_e (K_1 + [L]) + k_r k_p (K_2 + [L])}{k_r k_e (K_1 + [L]) + k_p [k_e [L] + k_r (K_2 + [L])]} \\ &= \frac{k_r \left[1 + \frac{k_p}{k_e} \left(\frac{K_2 + [L]}{K_1 + [L]} \right) \right]}{\left[k_r + \frac{k_p [L]}{K_1 + [L]} + \frac{k_p k_r}{k_e} \left(\frac{K_2 + [L]}{K_1 + [L]} \right) \right]}. \end{aligned}$$

Steady states for the remaining equations are also found by setting the right hand side of the equation equal to zero and solving for ξ_i , where ξ_i denotes the steady state for equation $x_i(t)$. The remaining steady states in terms of ξ_1 are

$$\xi_3 = \frac{\xi_1 \tilde{k}_a}{\xi_1 \tilde{k}_a + k_d} \quad (68)$$

$$\xi_4 = \frac{k_{rep} (\tilde{K}_c + \nu) (k_d + \tilde{k}_a \xi_1)}{k_d k_{rep} (\tilde{K}_c + \nu) + \tilde{k}_a (\tilde{K}_c k_{rep} + (k_{rep} + \tilde{k}_{hyd}) \nu) \xi_1} \quad (69)$$

$$\xi_5 = \frac{\tilde{k}_a \tilde{k}_{hyd} k_{rep} \nu \xi_1}{k_d k_{d3} k_{rep} (\tilde{K}_c + \nu) + \tilde{k}_a k_{d3} (\tilde{K}_c k_{rep} + (k_{rep} + \tilde{k}_{hyd}) \nu) \xi_1} \quad (70)$$

$$\xi_6 = \frac{k_{rep} + \frac{k_{ap2}k_{dp2}\zeta}{k_{ap2} + k_{dp2}} - \frac{k_{rep}^2(\tilde{K}_c + \nu)(k_d + \tilde{k}_a\xi)}{k_d k_{rep}(\tilde{K}_c + \nu) + \tilde{k}_a(\tilde{K}_c k_{rep} + (k_{rep} + \tilde{k}_{hyd})\nu)\xi_1}}{k_{dp1}} \quad (71)$$

$$\xi_7 = \frac{k_{ap2}}{k_{ap2} + k_{dp2}} \quad (72)$$

$$\xi_8 = \nu \quad (73)$$

$$\xi_9 = 0, \quad (74)$$

with ν given in equation (45).

III.3.1 Local Stability of Steady States

Due to the fact that our model is a simplification of the actual signaling pathway and therefore our system of ordinary differential equations as well as the initial conditions are approximations to the actual dynamical response to a stimulus, it becomes necessary to investigate the qualitative behavior of the model, such as how sensitive our model is to small perturbations or changes of initial conditions and various model parameters. One important qualitative phenomenon is that of the stability of a certain state or solution of our system of equations. In particular, we now look into the stability of the steady states of our simplified model. First we define the concepts of stability and asymptotic stability of a steady state ξ_0 of an autonomous (not explicitly depending on time) system of the form

$$\dot{\mathbf{x}} = \mathbf{f}(\mathbf{x}), \quad (75)$$

and then of an arbitrary solution to the nonautonomous (explicitly depending on time) system of the form

$$\dot{\mathbf{x}} = \mathbf{f}(t, \mathbf{x}). \quad (76)$$

Definitions 1 and 2 are for the autonomous system, and definitions 3 and 4 are for the nonautonomous system.

Definition 1. ([8], Definition 1) Denote $\boldsymbol{\xi}_0$ to be the equilibrium solution of (75). This solution is said to be *stable* if for each number $\varepsilon > 0$ we can find a number $\delta > 0$ (depending on ε) such that if $\boldsymbol{\phi}(t)$ is any solution of (75) having $\|\boldsymbol{\phi}(t_0) - \boldsymbol{\xi}_0\| < \delta$, then the solution $\boldsymbol{\phi}(t)$ exists for all $t \geq t_0$ and $\|\boldsymbol{\phi}(t) - \boldsymbol{\xi}_0\| < \varepsilon$ for $t \geq t_0$ (where, for convenience, $\|\cdot\|$ may be thought of as the Euclidean norm.)

Definition 2. ([8], Definition 2) The equilibrium solution $\boldsymbol{\xi}_0$ is said to be *asymptotically stable* if it is stable and if there exists a number $\delta_0 > 0$ such that if $\boldsymbol{\phi}(t)$ is any solution of (75) having $\|\boldsymbol{\phi}(t_0) - \boldsymbol{\xi}_0\| < \delta_0$, then $\lim_{t \rightarrow +\infty} \boldsymbol{\phi}(t) = \boldsymbol{\xi}_0$.

The equilibrium solution $\boldsymbol{\xi}_0$ is said to be *unstable* if it is not stable.

In equation (76) above, the real vector \mathbf{f} with n components is defined and continuous in some region $D = \{(t, \mathbf{x}) \mid 0 \leq t \leq \infty, |\mathbf{x}| < a\}$ of real $(n+1)$ -dimensional Euclidean space, and with $a \in \mathbb{R}$ such that $a \geq 0$. For the purposes of Definitions 3 and 4, we let $\boldsymbol{\phi}(t)$ be some solution of (76) existing on $[0, \infty)$, and $\boldsymbol{\psi}(t, t_0, \mathbf{x}_0)$, $t_0 \geq 0$, be a solution of (76) such that $\boldsymbol{\psi}(t_0, t_0, \mathbf{x}_0) = \mathbf{x}_0$.

Definition 3. ([8], Definition 3) The solution $\boldsymbol{\phi}(t)$ of (76) is said to be *stable* if for every $\varepsilon > 0$ and every $t_0 \geq 0$ there exists a $\delta > 0$ (δ now depending on both ε and possibly t_0) such that whenever $|\boldsymbol{\phi}(t_0) - \mathbf{x}_0| < \delta$, the solution $\boldsymbol{\psi}(t, t_0, \mathbf{x}_0)$ exists for all $t > t_0$ and satisfies $|\boldsymbol{\phi}(t) - \boldsymbol{\psi}(t, t_0, \mathbf{x}_0)| < \varepsilon$ for $t \geq t_0$.

Definition 4. ([8], Definition 4) The solution $\boldsymbol{\phi}(t)$ of (76) is said to be *asymptotically stable* if it is stable and if there exists a $\delta_0 > 0$ such that whenever $|\boldsymbol{\phi}(t_0) - \mathbf{x}_0| < \delta_0$, the solution $\boldsymbol{\psi}(t, t_0, \mathbf{x}_0)$ approaches the solution $\boldsymbol{\phi}(t)$ as $t \rightarrow \infty$ (in other words, $\lim_{t \rightarrow \infty} |\boldsymbol{\psi}(t, t_0, \mathbf{x}_0) - \boldsymbol{\phi}(t)| = 0$).

We first consider the local stability properties of our steady state solution $\boldsymbol{\xi}$ of the system $\dot{\mathbf{x}} = \mathbf{F}(\mathbf{x})$ with $\mathbf{F}_i = f_i$ for $i \in \{1, \dots, 9\}$ defined in equations (48) through

(56). To examine the local stability properties of $\boldsymbol{\xi}$, we first need the following result due to Poincare and Perron [8]:

Theorem III.3.1. ([8], Theorem 4.3) *Consider the system*

$$\dot{\mathbf{x}} = \mathbf{A}\mathbf{x} + \mathbf{f}(t, \mathbf{x}), \quad (77)$$

where all eigenvalues of \mathbf{A} have negative real parts, $\mathbf{f}(t, \mathbf{x})$ and $(\partial\mathbf{f}/\partial x_j)(t, \mathbf{x})$ for $(j = 1, \dots, n)$ are continuous in (t, \mathbf{x}) for $0 \leq t < \infty$, $|\mathbf{x}| < \mathbf{k}$ where $k > 0$ is a constant, and \mathbf{f} is small in the sense that

$$\lim_{|\mathbf{x}| \rightarrow \mathbf{0}} \frac{|\mathbf{f}(t, \mathbf{x})|}{|\mathbf{x}|} = 0 \quad (78)$$

uniformly with respect to t on $0 \leq t < \infty$. Then the solution $\mathbf{x} \equiv \mathbf{0}$ of (77) is asymptotically stable.

Using Theorem III.3.1, we show in Proposition III.3.1 that the equilibrium solution $\boldsymbol{\xi}(t)$ of our system is indeed locally asymptotically stable.

Proposition III.3.1. *The equilibrium solution $\boldsymbol{\xi}(t)$ of the system of equations (48) through (56) is locally asymptotically stable.*

Proof. First we consider the linearization of our system \mathbf{F} at $\boldsymbol{\xi}$ by defining $\mathbf{y} = \mathbf{x} - \boldsymbol{\xi}(t)$ so that

$$\begin{aligned} \dot{\mathbf{y}} &= \mathbf{F}(t, \mathbf{x}) - \mathbf{F}(t, \boldsymbol{\xi}(t)) = \mathbf{F}(t, \mathbf{y} + \boldsymbol{\xi}(t)) - \mathbf{F}(t, \boldsymbol{\xi}(t)) \\ &= \frac{\partial \mathbf{F}}{\partial \mathbf{x}}(t, \boldsymbol{\xi}(t))\mathbf{y} + \mathbf{G}(t, \mathbf{y}), \end{aligned} \quad (79)$$

where \mathbf{G} , by construction, satisfies condition (78) of Theorem III.3.1. Furthermore, by setting $\mathbf{A} = \frac{\partial \mathbf{F}}{\partial \mathbf{x}}(t, \boldsymbol{\xi}(t))$, which is the Jacobian matrix of our system at the steady state solution $\boldsymbol{\xi}$, we simply need to determine the sign of the eigenvalues of this Jacobian matrix given in Figure 3. Eigenvalues for this Jacobian matrix are found

Table 3: Eigenvalues for the Jacobian Matrix

Eigenvalue
$\lambda_1 = -k_{d3}$
$\lambda_2 = -k_{dp1}$
$\lambda_3 = -k_{ap2} - k_{dp2}$
$\lambda_4 = -\frac{(K_1 K_2 k_r + K_1 k_e L + K_2 k_p L + K_1 k_r L + K_2 k_r L + k_e L^2 + k_p L^2 + k_r L^2)}{2(K_1 + L)(K_2 + L)} +$ $\frac{\sqrt{-4L(K_1 + L)(K_2 + L)(K_1 k_e k_r + K_2 k_p k_r + (k_e k_p + k_p k_r)L) + (K_1(K_2 k_r + (k_e + k_r)L) + L(K_2(k_p + k_r) + (k_e + k_p + k_r)L))^2}}{2(K_1 + L)(K_2 + L)}$
$\lambda_5 = -\frac{(K_1 K_2 k_r + K_1 k_e L + K_2 k_p L + K_1 k_r L + K_2 k_r L + k_e L^2 + k_p L^2 + k_r L^2)}{2(K_1 + L)(K_2 + L)} -$ $\frac{\sqrt{-4L(K_1 + L)(K_2 + L)(K_1 k_e k_r + K_2 k_p k_r + (k_e k_p + k_p k_r)L) + (K_1(K_2 k_r + (k_e + k_r)L) + L(K_2(k_p + k_r) + (k_e + k_p + k_r)L))^2}}{2(K_1 + L)(K_2 + L)}$
$\lambda_6 = -\beta$
$\lambda_7 = -\gamma$
$\lambda_8 = -k_d - \tilde{k}_a \xi_1$
$\lambda_9 = -k_{rep} - \frac{\tilde{k}_{hyd} \xi_3 \nu}{\tilde{K}_c + \nu}$

using Mathematica and are listed in Table 3. Except in the case of λ_5 and λ_6 it is immediately clear that all eigenvalues are real and negative, as all rate parameters are strictly positive. If the term under the square root in λ_5 and λ_6 is positive, both of these eigenvalues have negative real parts, and if the term under the square root is negative, then λ_6 is real and negative. In this second case, λ_5 is also real and negative by the following argument: λ_5 can be written as $\frac{-b+\sqrt{b^2-4ac}}{2a}$, so that we have $b^2 - 4ac > 0 \Rightarrow$ the real part of λ_5 is negative $\iff b > \sqrt{b^2 - 4ac} \iff b^2 > b^2 - 4ac \iff -4ac < 0$, but this is always true since all of the rate constants contained in the terms a and c are positive. Therefore, we have that all eigenvalues of the Jacobian matrix $\frac{\partial \mathbf{F}}{\partial \mathbf{x}}(t, \boldsymbol{\xi}(t))$ have negative real parts, so that the hypotheses of Theorem III.3.1 are satisfied for the linearization equation (79).

We can thus conclude that the solution $\mathbf{y} \equiv 0$ of equation (79) is asymptotically stable, which is equivalent to concluding the (local) asymptotic stability of the solution $\mathbf{x} = \boldsymbol{\xi}(t)$. ■

III.3.2 Global Stability of Steady States

Here we extend the local stability analysis from the previous section to a global stability result. We make note that from the analytical equations for $x_8(t)$ and $x_9(t)$, we know that the steady states $\xi_8 = \nu$ and $\xi_9 = 0$ are globally asymptotically stable. First we simultaneously prove global stability of ξ_1 and ξ_2 , the steady states of x_1 and x_2 , respectively.

Proposition III.3.2. *The steady states ξ_1 and ξ_2 are globally asymptotically stable within the region of global existence of $x_1(t)$ and $x_2(t)$ as defined in Proposition III.2.2.*

Proof. First we rewrite the differential equations for x_1 and x_2 as follows:

$$\begin{aligned}x_1' &= k_r(1 - x_1 - x_2) - c_1x_1 \\x_2' &= c_1x_1 - c_2x_2,\end{aligned}$$

where c_1 and c_2 are defined in equation (63). Writing this system of equations in matrix form, we have

$$\begin{bmatrix} x_1 \\ x_2 \end{bmatrix}' = \begin{bmatrix} -(k_r + c_1) - k_r & \\ c_1 & -c_2 \end{bmatrix} \begin{bmatrix} x_1 \\ x_2 \end{bmatrix} + \begin{bmatrix} k_r \\ 0 \end{bmatrix}.$$

Then by the variation of parameters formula, we have that

$$\mathbf{x}(t) = e^{[t\mathbf{A}]} \mathbf{x}_0 + \int_0^t e^{[(t-s)\mathbf{A}]} \begin{bmatrix} k_r \\ 0 \end{bmatrix} ds$$

is the solution of this system, where

$$\mathbf{A} = \begin{bmatrix} -(k_r + c_1) - k_r & \\ c_1 & -c_2 \end{bmatrix} \quad (80)$$

with eigenvalues

$$\lambda_1 = \frac{-c_1 - c_2 - k_r + \sqrt{c_1^2 + (c_2 - k_r)^2 - 2c_1(c_2 + k_r)}}{2} \quad (81)$$

$$\lambda_2 = \frac{-c_1 - c_2 - k_r - \sqrt{c_1^2 + (c_2 - k_r)^2 - 2c_1(c_2 + k_r)}}{2}. \quad (82)$$

In general, for an n -by- n matrix \mathbf{A} with n distinct eigenvalues, we know that there exist n linearly independent eigenvectors $\mathbf{v}_1, \dots, \mathbf{v}_n$, corresponding to these eigenvalues.

We can then define the matrix

$$\mathbf{T} = [\mathbf{v}_1, \mathbf{v}_2, \dots, \mathbf{v}_n] \quad (83)$$

having these n linearly independent eigenvectors as columns. As a result of Theorem III.3.2 stated below (taken from Brauer and Nohel's Theorem 2.8 on page 76 [8]), we

can therefore write

$$\mathbf{T}^{-1}\mathbf{A}\mathbf{T} = \mathbf{D},$$

where \mathbf{D} is the diagonal matrix

$$\mathbf{D} = \begin{bmatrix} \lambda_1 & & & 0 \\ & \lambda_2 & & \\ & & \ddots & \\ 0 & & & \lambda_n \end{bmatrix}. \quad (84)$$

Theorem III.3.2. (Diagonal Canonical Form. [8], Theorem 2.9) *If the n -by- n constant matrix \mathbf{A} has n linearly independent eigenvectors $\mathbf{v}_1, \dots, \mathbf{v}_n$, corresponding to the eigenvalues $\lambda_1, \lambda_2, \dots, \lambda_n$, then \mathbf{A} is similar to the diagonal matrix \mathbf{D} given by (84), and the matrix \mathbf{T} that accomplishes the similarity is given by (83).*

So by Theorem III.3.2, since our eigenvalues λ_1 and λ_2 from equations (81) and (82) are distinct, we can write

$$\mathbf{T}^{-1}\mathbf{A}\mathbf{T} = \mathbf{J} \quad \Rightarrow \quad \mathbf{A} = \mathbf{T}\mathbf{J}\mathbf{T}^{-1}, \quad (85)$$

where

$$\mathbf{T} = [\mathbf{v}_1, \mathbf{v}_2] \quad \text{and} \quad \mathbf{J} = \begin{bmatrix} \lambda_1 & 0 \\ 0 & \lambda_2 \end{bmatrix}.$$

Then by equation (85) and by property of the exponential of a matrix, we have

$$e^{[t\mathbf{A}]} = \mathbf{T}e^{[t\mathbf{J}]} \mathbf{T}^{-1}. \quad (86)$$

Since we have that λ_1, λ_2 from (81) and (82) have negative real part, equation (86) gives

$$\lim_{t \rightarrow \infty} e^{[t\mathbf{A}]} = \lim_{t \rightarrow \infty} (\mathbf{T}e^{[t\mathbf{J}]\mathbf{T}^{-1}}) = \begin{bmatrix} 0 \\ 0 \end{bmatrix}.$$

Therefore as $t \rightarrow \infty$, our solution $\mathbf{x}(t) = (x_1(t), x_2(t))$ in equation (80) becomes

$$\begin{aligned} \lim_{t \rightarrow \infty} \mathbf{x}(t) &= \lim_{t \rightarrow \infty} (e^{[t\mathbf{A}]\mathbf{x}_0}) + \lim_{t \rightarrow \infty} \left(\int_0^t e^{[(t-s)\mathbf{A}]} \begin{bmatrix} k_r \\ 0 \end{bmatrix} ds \right) \\ &= \lim_{t \rightarrow \infty} (\mathbf{T}e^{[t\mathbf{J}]\mathbf{T}^{-1}}\mathbf{x}_0) + \lim_{t \rightarrow \infty} \left(\int_0^t \mathbf{T}e^{[(t-s)\mathbf{J}]\mathbf{T}^{-1}} \begin{bmatrix} k_r \\ 0 \end{bmatrix} ds \right) \\ &= \mathbf{0} + \lim_{t \rightarrow \infty} \left(\mathbf{T} \left(\int_0^t e^{[(t-s)\mathbf{J}]} ds \right) \mathbf{T}^{-1} \begin{bmatrix} k_r \\ 0 \end{bmatrix} \right) \\ &= \lim_{t \rightarrow \infty} \left(\mathbf{T} \left(\int_0^t \begin{bmatrix} e^{(t-s)\lambda_1} & 0 \\ 0 & e^{(t-s)\lambda_2} \end{bmatrix} ds \right) \mathbf{T}^{-1} \begin{bmatrix} k_r \\ 0 \end{bmatrix} \right) \\ &= \mathbf{T} \begin{bmatrix} -\frac{1}{\lambda_1} & 0 \\ 0 & -\frac{1}{\lambda_2} \end{bmatrix} \mathbf{T}^{-1} \begin{bmatrix} k_r \\ 0 \end{bmatrix} = \begin{bmatrix} \xi_1 \\ \xi_2 \end{bmatrix}. \end{aligned} \tag{87}$$

Thus no matter what choice of initial vector \mathbf{x}_0 , we will always attain the steady state given by (87) and equivalent to the matrix $[\xi_1, \xi_2]^T$, where ξ_1 and ξ_2 are the steady states found earlier for $x_1(t)$ and $x_2(t)$, respectively. We have therefore proved the global stability of this steady state solution. ■

As seen in the next proposition, we now turn our focus to determining the global stability of the model's remaining steady states given in equations (68) through (74).

Proposition III.3.3. *The steady states ξ_i , $i = 3 \dots 7$, are globally asymptotically stable within the region of global existence as defined in Proposition III.2.2.*

Proof. We split the proof into a separate case for each steady state.

Case A: Global stability of ξ_3 . Since

$$x_3'(t) = \tilde{k}_a x_1(t) - (\tilde{k}_a x_1(t) + k_d) x_3(t),$$

by variation of parameters, we have

$$x_3(t) = e^{-\int_0^t (\tilde{k}_a x_1(s) + k_d) ds} x_3(0) + \int_0^t e^{-\int_s^t (\tilde{k}_a x_1(r) + k_d) dr} \tilde{k}_a x_1(s) ds. \quad (88)$$

Note that $\tilde{k}_a x_1(s) + k_d \geq k_d$ since $x_1(s) \geq 0$ for all $s \geq 0$ and $\tilde{k}_a, k_d > 0$ always.

Therefore, we have

$$\begin{aligned} \lim_{t \rightarrow \infty} \int_0^t k_d ds = \infty &\Rightarrow \lim_{t \rightarrow \infty} \int_0^t (\tilde{k}_a x_1(t) + k_d) ds = \infty \\ &\Rightarrow \lim_{t \rightarrow \infty} e^{-\int_0^t (\tilde{k}_a x_1(s) + k_d) ds} x_3(0) = 0, \end{aligned}$$

so that the asymptotic behavior of $x_3(t)$ does not depend on the choice of initial conditions. We now show that the solution $x_3(t)$ converges to its steady state ξ_3 . By (88), we have

$$\lim_{t \rightarrow \infty} x_3(t) = \lim_{t \rightarrow \infty} \left(e^{-\int_0^t (\tilde{k}_a x_1(s) + k_d) ds} x_3(0) + \int_0^t e^{-\int_s^t (\tilde{k}_a x_1(r) + k_d) dr} \tilde{k}_a x_1(s) ds \right)$$

if this limit exists.

Now take $\varepsilon > 0$ such that $\varepsilon < \tilde{k}_a \xi_1 + k_d$, and choose a t_1 such that

$$|\tilde{k}_a x_1(t) - \tilde{k}_a \xi_1| < \varepsilon \quad \text{for } t > t_1 > 0. \quad (89)$$

Such a t_1 exists since from (87) we know that $\lim_{t \rightarrow \infty} x_1(t) = \xi_1$. Note also for t sufficiently larger than t_1 , the following conditions hold:

- (i) $e^{-\int_0^t (\tilde{k}_a x_1(s) + k_d) ds} x_3(0) < \frac{\varepsilon}{2}$
- (ii) $\frac{\tilde{k}_a}{k_d} e^{-k_d t} [e^{k_d t_1} - 1] < \frac{\varepsilon}{2}$
- (iii) $e^{-(\tilde{k}_a \xi_1 + k_d + \varepsilon)(t - t_1)} < \varepsilon$.

Now from (88), we can write

$$\begin{aligned} x_3(t) &= e^{-\int_0^t (\tilde{k}_a x_1(s) + k_d) ds} x_3(0) + \int_0^{t_1} e^{-\int_s^t (\tilde{k}_a x_1(r) + k_d) dr} \tilde{k}_a x_1(s) ds \\ &\quad + \int_{t_1}^t e^{-\int_s^t (\tilde{k}_a x_1(r) + k_d) dr} \tilde{k}_a x_1(s) ds. \end{aligned}$$

Notice for the above choice of t_1 in (89) and for $t \gg t_1$ such that conditions (i) – (iii) hold, we have

$$\begin{aligned} &e^{-\int_0^t (\tilde{k}_a x_1(s) + k_d) ds} x_3(0) + \int_0^{t_1} e^{-\int_s^t (\tilde{k}_a x_1(r) + k_d) dr} \tilde{k}_a x_1(s) ds \\ &\leq \frac{\varepsilon}{2} + \tilde{k}_a \int_0^{t_1} e^{-\int_s^t (\tilde{k}_a x_1(r) + k_d) dr} ds \\ &\leq \frac{\varepsilon}{2} + \tilde{k}_a \int_0^{t_1} e^{-\int_s^t k_d dr} ds \\ &= \frac{\varepsilon}{2} + \tilde{k}_a e^{-k_d t} \int_0^{t_1} e^{k_d s} ds \\ &= \frac{\varepsilon}{2} + \frac{\tilde{k}_a}{k_d} e^{-k_d t} [e^{k_d t_1} - 1] < \frac{\varepsilon}{2} + \frac{\varepsilon}{2} = \varepsilon. \end{aligned} \tag{90}$$

Then for the same choice of t_1 and $t \gg t_1$, we also have

$$\begin{aligned} &\int_{t_1}^t e^{-\int_s^t (\tilde{k}_a x_1(r) + k_d) dr} \tilde{k}_a x_1(s) ds \\ &= \int_{t_1}^t e^{-\int_s^t [(\tilde{k}_a x_1(r) - \tilde{k}_a \xi_1) + (\tilde{k}_a \xi_1 + k_d)] dr} [(\tilde{k}_a x_1(s) - \tilde{k}_a \xi_1) + \tilde{k}_a \xi_1] ds \\ &\leq \int_{t_1}^t e^{-\int_s^t [(\tilde{k}_a \xi_1 + k_d) - \varepsilon] dr} (\varepsilon + \tilde{k}_a \xi_1) ds \\ &= (\varepsilon + \tilde{k}_a \xi_1) \int_{t_1}^t e^{-(\tilde{k}_a \xi_1 + k_d - \varepsilon)t} e^{(\tilde{k}_a \xi_1 + k_d - \varepsilon)s} ds \\ &= \left(\frac{\varepsilon + \tilde{k}_a \xi_1}{\tilde{k}_a \xi_1 + k_d - \varepsilon} \right) e^{-(\tilde{k}_a \xi_1 + k_d - \varepsilon)t} [e^{(\tilde{k}_a \xi_1 + k_d - \varepsilon)t} - e^{(\tilde{k}_a \xi_1 + k_d - \varepsilon)t_1}] \\ &= \left(\frac{\varepsilon + \tilde{k}_a \xi_1}{\tilde{k}_a \xi_1 + k_d - \varepsilon} \right) [1 - e^{-(\tilde{k}_a \xi_1 + k_d - \varepsilon)(t - t_1)}] \leq \left(\frac{\varepsilon + \tilde{k}_a \xi_1}{\tilde{k}_a \xi_1 + k_d - \varepsilon} \right). \end{aligned} \tag{91}$$

Thus (90) and (91) together give

$$x_3(t) \leq \varepsilon + \left(\frac{\varepsilon + \tilde{k}_a \xi_1}{\tilde{k}_a \xi_1 + k_d - \varepsilon} \right) \quad \forall t \gg t_1. \quad (92)$$

Now we need to find a lower bound for $x_3(t)$. For the above choice of t_1 and $t \gg t_1$, we have

$$\begin{aligned} x_3(t) &= e^{-\int_0^t (\tilde{k}_a x_1(s) + k_d) ds} x_3(0) + \int_0^t e^{-\int_s^t (\tilde{k}_a x_1(r) + k_d) dr} \tilde{k}_a x_1(s) ds \\ &\geq \int_0^{t_1} e^{-\int_s^t (\tilde{k}_a x_1(r) + k_d) dr} \tilde{k}_a x_1(s) ds + \int_{t_1}^t e^{-\int_s^t (\tilde{k}_a x_1(r) + k_d) dr} \tilde{k}_a x_1(s) ds \\ &\geq \int_{t_1}^t e^{-\int_s^t (\tilde{k}_a x_1(r) + k_d) dr} \tilde{k}_a x_1(s) ds \\ &= \int_{t_1}^t e^{-\int_s^t [(\tilde{k}_a x_1(r) - \tilde{k}_a \xi_1) + (\tilde{k}_a \xi_1 + k_d)] dr} [(\tilde{k}_a x_1(s) - \tilde{k}_a \xi_1) + \tilde{k}_a \xi_1] ds \\ &\geq \int_{t_1}^t e^{-\int_s^t [(\tilde{k}_a \xi_1 + k_d) + \varepsilon] dr} (\tilde{k}_a \xi_1 - \varepsilon) ds \\ &= \left(\frac{\tilde{k}_a \xi_1 - \varepsilon}{\tilde{k}_a \xi_1 + k_d + \varepsilon} \right) e^{-(\tilde{k}_a \xi_1 + k_d + \varepsilon)t} \left[e^{(\tilde{k}_a \xi_1 + k_d + \varepsilon)t} - e^{(\tilde{k}_a \xi_1 + k_d + \varepsilon)t_1} \right] \\ &= \left(\frac{\tilde{k}_a \xi_1 - \varepsilon}{\tilde{k}_a \xi_1 + k_d + \varepsilon} \right) \left[1 - e^{-(\tilde{k}_a \xi_1 + k_d + \varepsilon)(t - t_1)} \right] \\ &\geq \left(\frac{\tilde{k}_a \xi_1 - \varepsilon}{\tilde{k}_a \xi_1 + k_d + \varepsilon} \right) [1 - \varepsilon]. \end{aligned}$$

Together with (92), this gives

$$\left(\frac{\tilde{k}_a \xi_1 - \varepsilon}{\tilde{k}_a \xi_1 + k_d + \varepsilon} \right) [1 - \varepsilon] \leq x_3(t) \leq \varepsilon + \left(\frac{\varepsilon + \tilde{k}_a \xi_1}{\tilde{k}_a \xi_1 + k_d - \varepsilon} \right) \quad \forall t \gg t_1.$$

Taking $\varepsilon \rightarrow 0$ forces $t \rightarrow \infty$, giving the desired result:

$$\lim_{t \rightarrow \infty} x_3(t) = \frac{\tilde{k}_a \xi_1}{\tilde{k}_a \xi_1 + k_d} = \xi_3.$$

We proceed in a similar fashion for the remaining model equations.

Case B: Global stability of ξ_4 . Since

$$x_4'(t) = \left[-\tilde{k}_{hyd} \frac{x_8(t)}{\tilde{K}_c + x_8(t)} x_3(t) - k_{rep} \right] x_4(t) + k_{rep},$$

by variation of parameters, we have

$$\begin{aligned} x_4(t) &= e^{-\int_0^t \left(\tilde{k}_{hyd} \frac{x_8(s)}{\tilde{K}_c + x_8(s)} x_3(s) + k_{rep} \right) ds} x_4(0) \\ &\quad + \int_0^t e^{-\int_s^t \left(\tilde{k}_{hyd} \frac{x_8(s)}{\tilde{K}_c + x_8(s)} x_3(s) + k_{rep} \right) ds} k_{rep} ds. \end{aligned} \quad (93)$$

Recalling that $\xi_8 = \nu$, now we take $\varepsilon > 0$ such that $\varepsilon < \tilde{k}_{hyd} \frac{\nu}{\tilde{K}_c + \nu} \xi_3 + k_{rep}$. We can choose a $t_1 > 0$ such that

$$\left| \left(\tilde{k}_{hyd} \frac{x_8(s)}{\tilde{K}_c + x_8(s)} x_3(s) \right) - \left(\tilde{k}_{hyd} \frac{\nu}{\tilde{K}_c + \nu} \xi_3 \right) \right| < \varepsilon \quad \text{for } t > t_1 > 0. \quad (94)$$

Such a t_1 exists since from (45) and (93). Note also for t sufficiently larger than t_1 , the following conditions hold:

$$\begin{aligned} (i) \quad & e^{-\int_0^t \left(\tilde{k}_{hyd} \frac{x_8(s)}{\tilde{K}_c + x_8(s)} x_3(s) + k_{rep} \right) ds} x_4(0) < \frac{\varepsilon}{2} \\ (ii) \quad & e^{-k_{rep}t} \left[e^{k_{rep}t_1} - 1 \right] < \frac{\varepsilon}{2} \\ (iii) \quad & e^{-(\tilde{k}_{hyd} \frac{\nu}{\tilde{K}_c + \nu} \xi_3 + k_{rep} + \varepsilon)(t - t_1)} < \varepsilon. \end{aligned}$$

Now from (93), we can write

$$\begin{aligned} x_4(t) &= e^{-\int_0^t \left(\tilde{k}_{hyd} \frac{x_8(s)}{\tilde{K}_c + x_8(s)} x_3(s) + k_{rep} \right) ds} x_4(0) \\ &\quad + \int_0^{t_1} e^{-\int_s^t \left(\tilde{k}_{hyd} \frac{x_8(s)}{\tilde{K}_c + x_8(s)} x_3(s) + k_{rep} \right) ds} k_{rep} ds \\ &\quad + \int_{t_1}^t e^{-\int_s^t \left(\tilde{k}_{hyd} \frac{x_8(s)}{\tilde{K}_c + x_8(s)} x_3(s) + k_{rep} \right) ds} k_{rep} ds. \end{aligned}$$

Notice for the above choice of t_1 in (94) and for $t \gg t_1$ such that conditions (i) – (iii) hold, we have

$$\begin{aligned} e^{-\int_0^t \left(\tilde{k}_{hyd} \frac{x_8(s)}{\bar{K}_c + x_8(s)} x_3(s) + k_{rep} \right) ds} x_4(0) + \int_0^{t_1} e^{-\int_s^t \left(\tilde{k}_{hyd} \frac{x_8(s)}{\bar{K}_c + x_8(s)} x_3(s) + k_{rep} \right) ds} k_{rep} ds \\ \leq \frac{\varepsilon}{2} + e^{-k_{rep} t} \left[e^{k_{rep} t_1} - 1 \right] < \frac{\varepsilon}{2} + \frac{\varepsilon}{2} = \varepsilon. \end{aligned} \quad (95)$$

Then for the same choice of t_1 and $t \gg t_1$,

$$\begin{aligned} \int_{t_1}^t e^{-\int_s^t \left(\tilde{k}_{hyd} \frac{x_8(s)}{\bar{K}_c + x_8(s)} x_3(s) + k_{rep} \right) ds} k_{rep} ds \\ = \int_{t_1}^t e^{-\int_s^t \left(\left[\tilde{k}_{hyd} \frac{x_8(s)}{\bar{K}_c + x_8(s)} x_3(s) - \tilde{k}_{hyd} \frac{\nu}{\bar{K}_c + \nu} \xi_3 \right] + \tilde{k}_{hyd} \frac{\nu}{\bar{K}_c + \nu} \xi_3 + k_{rep} \right) ds} k_{rep} ds \\ \leq \int_{t_1}^t e^{-\int_s^t \left[\tilde{k}_{hyd} \frac{\nu}{\bar{K}_c + \nu} \xi_3 + k_{rep} - \varepsilon \right] ds} k_{rep} ds \\ = \frac{k_{rep}}{\tilde{k}_{hyd} \frac{\nu}{\bar{K}_c + \nu} \xi_3 + k_{rep} - \varepsilon} \left[1 - e^{-(\tilde{k}_{hyd} \frac{\nu}{\bar{K}_c + \nu} \xi_3 + k_{rep} - \varepsilon)(t - t_1)} \right] \\ \leq \frac{k_{rep}}{\tilde{k}_{hyd} \frac{\nu}{\bar{K}_c + \nu} \xi_3 + k_{rep} - \varepsilon}. \end{aligned} \quad (96)$$

Combining (95) and (96), we have

$$x_4(t) \leq \varepsilon + \frac{k_{rep}}{\tilde{k}_{hyd} \frac{\nu}{\bar{K}_c + \nu} \xi_3 + k_{rep} - \varepsilon} \quad \forall t \gg t_1. \quad (97)$$

For the above choice of t_1 and $t \gg t_1$,

$$\begin{aligned} x_4(t) = e^{-\int_0^t \left(\tilde{k}_{hyd} \frac{x_8(s)}{\bar{K}_c + x_8(s)} x_3(s) + k_{rep} \right) ds} x_4(0) + \int_0^t e^{-\int_s^t \left(\tilde{k}_{hyd} \frac{x_8(s)}{\bar{K}_c + x_8(s)} x_3(s) + k_{rep} \right) ds} k_{rep} ds \\ \geq \int_0^{t_1} e^{-\int_s^t \left(\tilde{k}_{hyd} \frac{x_8(s)}{\bar{K}_c + x_8(s)} x_3(s) + k_{rep} \right) ds} k_{rep} ds \\ + \int_{t_1}^t e^{-\int_s^t \left(\tilde{k}_{hyd} \frac{x_8(s)}{\bar{K}_c + x_8(s)} x_3(s) + k_{rep} \right) ds} k_{rep} ds \\ \geq \int_{t_1}^t e^{-\int_s^t \left(\tilde{k}_{hyd} \frac{x_8(s)}{\bar{K}_c + x_8(s)} x_3(s) + k_{rep} \right) ds} k_{rep} ds \\ \geq \frac{k_{rep}}{\tilde{k}_{hyd} \frac{\nu}{\bar{K}_c + \nu} \xi_3 + k_{rep} + \varepsilon} \left[1 - e^{-(\tilde{k}_{hyd} \frac{\nu}{\bar{K}_c + \nu} \xi_3 + k_{rep} + \varepsilon)(t - t_1)} \right] \\ \geq \frac{k_{rep}}{\tilde{k}_{hyd} \frac{\nu}{\bar{K}_c + \nu} \xi_3 + k_{rep} + \varepsilon} [1 - \varepsilon]. \end{aligned}$$

Together with (97), this gives

$$\frac{k_{rep}}{\tilde{k}_{hyd} \frac{\nu}{\tilde{K}_c + \nu} \xi_3 + k_{rep} + \varepsilon} [1 - \varepsilon] \leq x_4(t) \leq \varepsilon + \frac{k_{rep}}{\tilde{k}_{hyd} \frac{\nu}{\tilde{K}_c + \nu} \xi_3 + k_{rep} - \varepsilon} \quad \forall t \gg t_1.$$

Taking $\varepsilon \rightarrow 0$ forces $t \rightarrow \infty$, giving the desired result:

$$\lim_{t \rightarrow \infty} x_4(t) = \frac{k_{rep}}{\tilde{k}_{hyd} \frac{\nu}{\tilde{K}_c + \nu} \xi_3 + k_{rep}} = \xi_4. \quad (98)$$

Case C: Global stability of ξ_5 . The derivative for $x_5(t)$ is given by

$$x_5'(t) = \tilde{k}_{hyd} \frac{x_8(t)}{\tilde{K}_c + x_8(t)} x_3(t) x_4(t) - k_{d3} x_5(t), \quad (99)$$

so by the variation of parameters formula we can write

$$x_5(t) = e^{-\int_0^t k_{d3} ds} x_5(0) + \int_0^t e^{-\int_s^t k_{d3} ds} \tilde{k}_{hyd} \frac{x_8(t)}{\tilde{K}_c + x_8(t)} x_3(t) x_4(t) ds. \quad (100)$$

Here we take any $\varepsilon > 0$ and choose a $t_1 > 0$ such that

$$\left| \left(\tilde{k}_{hyd} \frac{x_8(t)}{\tilde{K}_c + x_8(t)} x_3(t) x_4(t) \right) - \left(\tilde{k}_{hyd} \frac{\nu}{\tilde{K}_c + \nu} \xi_3 \xi_4 \right) \right| < \varepsilon \quad \text{for } t > t_1 > 0. \quad (101)$$

Such a t_1 exists by (45), (93), and (98).

Note also for t sufficiently larger than t_1 , the following conditions hold:

- (i) $e^{-\int_0^t k_{d3} ds} x_5(0) < \frac{\varepsilon}{2}$
- (ii) $\frac{\tilde{k}_{hyd}}{k_{d3}} e^{-k_{d3} t} [e^{k_{d3} t_1} - 1] < \frac{\varepsilon}{2}$
- (iii) $e^{-k_{d3}(t-t_1)} < \varepsilon$.

From (100), we can write

$$\begin{aligned} x_5(t) &= e^{-\int_0^t k_{d3} ds} x_5(0) + \int_0^{t_1} e^{-\int_s^t k_{d3} ds} \tilde{k}_{hyd} \frac{x_8(t)}{\tilde{K}_c + x_8(t)} x_3(t) x_4(t) ds \\ &\quad + \int_{t_1}^t e^{-\int_s^t k_{d3} ds} \tilde{k}_{hyd} \frac{x_8(t)}{\tilde{K}_c + x_8(t)} x_3(t) x_4(t) ds. \end{aligned}$$

Notice for the above choice of t_1 in (101) and for $t \gg t_1$ such that conditions (i) – (iii) hold, we have

$$\begin{aligned} e^{-\int_0^t k_{d3} ds} x_5(0) + \int_0^{t_1} e^{-\int_s^t k_{d3} ds} \tilde{k}_{hyd} \frac{x_8(t)}{\tilde{K}_c + x_8(t)} x_3(t) x_4(t) ds \\ \leq \frac{\varepsilon}{2} + \frac{\tilde{k}_{hyd}}{k_{d3}} e^{-k_{d3} t} [e^{k_{d3} t_1} - 1] \\ < \frac{\varepsilon}{2} + \frac{\varepsilon}{2} = \varepsilon. \end{aligned} \quad (102)$$

Then for the same choice of t_1 and $t \gg t_1$,

$$\begin{aligned} &\int_{t_1}^t e^{-\int_s^t k_{d3} ds} \tilde{k}_{hyd} \frac{x_8(t)}{\tilde{K}_c + x_8(t)} x_3(t) x_4(t) ds \\ &= \int_{t_1}^t e^{-\int_s^t k_{d3} ds} \left[\left(\tilde{k}_{hyd} \frac{x_8(t)}{\tilde{K}_c + x_8(t)} x_3(t) x_4(t) - \tilde{k}_{hyd} \frac{\nu}{\tilde{K}_c + \nu} \xi_3 \xi_4 \right) + \tilde{k}_{hyd} \frac{\nu}{\tilde{K}_c + \nu} \xi_3 \xi_4 \right] ds \\ &\leq \int_{t_1}^t e^{-\int_s^t k_{d3} ds} \left(\varepsilon + \tilde{k}_{hyd} \frac{\nu}{\tilde{K}_c + \nu} \xi_3 \xi_4 \right) ds \\ &= \frac{\varepsilon + \tilde{k}_{hyd} \frac{\nu}{\tilde{K}_c + \nu} \xi_3 \xi_4}{k_{d3}} [1 - e^{-k_{d3}(t-t_1)}] \\ &\leq \frac{\varepsilon + \tilde{k}_{hyd} \frac{\nu}{\tilde{K}_c + \nu} \xi_3 \xi_4}{k_{d3}}. \end{aligned} \quad (103)$$

Therefore (102) and (103) give

$$x_5(t) \leq \varepsilon + \frac{\varepsilon + \tilde{k}_{hyd} \frac{\nu}{\tilde{K}_c + \nu} \xi_3 \xi_4}{k_{d3}} \quad \forall t \gg t_1. \quad (104)$$

For the above choice of t_1 and $t \gg t_1$,

$$\begin{aligned}
x_5(t) &= e^{-\int_0^t k_{d3} ds} x_5(0) + \int_0^{t_1} e^{-\int_s^t k_{d3} ds} \tilde{k}_{hyd} \frac{x_8(t)}{\tilde{K}_c + x_8(t)} x_3(t) x_4(t) ds \\
&\quad + \int_{t_1}^t e^{-\int_s^t k_{d3} ds} \tilde{k}_{hyd} \frac{x_8(t)}{\tilde{K}_c + x_8(t)} x_3(t) x_4(t) ds \\
&\geq \int_{t_1}^t e^{-\int_s^t k_{d3} ds} \tilde{k}_{hyd} \frac{x_8(t)}{\tilde{K}_c + x_8(t)} x_3(t) x_4(t) ds \\
&\geq \frac{\tilde{k}_{hyd} \frac{\nu}{\tilde{K}_c + \nu} \xi_3 \xi_4 - \varepsilon}{k_{d3}} [1 - e^{-k_{d3}(t-t_1)}] \\
&\geq \frac{\tilde{k}_{hyd} \frac{\nu}{\tilde{K}_c + \nu} \xi_3 \xi_4 - \varepsilon}{k_{d3}} [1 - \varepsilon].
\end{aligned}$$

In combination with (104), this gives

$$\frac{\tilde{k}_{hyd} \frac{\nu}{\tilde{K}_c + \nu} \xi_3 \xi_4 - \varepsilon}{k_{d3}} [1 - \varepsilon] \leq x_5(t) \leq \varepsilon + \frac{\varepsilon + \tilde{k}_{hyd} \frac{\nu}{\tilde{K}_c + \nu} \xi_3 \xi_4}{k_{d3}} \quad \forall t \gg t_1.$$

Sending $\varepsilon \rightarrow 0$ forces $t \rightarrow \infty$, giving the desired result:

$$\lim_{t \rightarrow \infty} x_5(t) = \frac{\tilde{k}_{hyd} \frac{\nu}{\tilde{K}_c + \nu} \xi_3 \xi_4}{k_{d3}} = \xi_5.$$

In order to study the global stability of ξ_6 , we first need to investigate the stability properties of ξ_7 .

Case D: Global stability of ξ_7 . From

$$x_7'(t) = -k_{dp2} x_7(t) + k_{ap2} (1 - x_7(t)),$$

variation of parameters gives

$$x_7(t) = e^{-\int_0^t (k_{ap1} + k_{ap2}) ds} x_7(0) + \int_0^t e^{-\int_s^t (k_{ap1} + k_{ap2}) ds} k_{ap2} ds.$$

Thus

$$\begin{aligned}
\lim_{t \rightarrow \infty} x_7(t) &= \lim_{t \rightarrow \infty} \left(e^{-\int_0^t (k_{ap1} + k_{ap2}) ds} x_7(0) + \int_0^t e^{-\int_s^t (k_{ap1} + k_{ap2}) ds} k_{ap2} ds \right) \\
&= \lim_{t \rightarrow \infty} \int_0^t e^{-\int_s^t (k_{ap1} + k_{ap2}) ds} k_{ap2} ds \\
&= \lim_{t \rightarrow \infty} \left(\frac{k_{ap2}}{k_{ap1} + k_{ap2}} \right) e^{-(k_{ap1} + k_{ap2})t} \left[e^{(k_{ap1} + k_{ap2})t} - 1 \right] \\
&= \lim_{t \rightarrow \infty} \left(\frac{k_{ap2}}{k_{ap1} + k_{ap2}} \right) \left[1 - e^{-(k_{ap1} + k_{ap2})t} \right] = \frac{k_{ap2}}{k_{ap1} + k_{ap2}} = \xi_7.
\end{aligned}$$

Therefore ξ_7 is globally asymptotically stable. Now we can investigate the stability of ξ_6 .

Case E: Global stability of ξ_6 . Since

$$x'_6(t) = \tilde{k}_{hyd} \frac{x_8(t)}{\tilde{K}_c + x_8(t)} x_3(t) x_4(t) + k_{dp2} \zeta x_7(t) - k_{dp1} x_6(t), \quad (105)$$

variation of parameters gives

$$\begin{aligned}
x_6(t) &= e^{-\int_0^t k_{dp1} ds} x_6(0) \\
&\quad + \int_0^t e^{-\int_s^t k_{dp1} ds} \left(\tilde{k}_{hyd} \frac{x_8(t)}{\tilde{K}_c + x_8(t)} x_3(t) x_4(t) + k_{dp2} \zeta x_7(t) \right) ds. \quad (106)
\end{aligned}$$

Given $\varepsilon > 0$, we choose a $t_1 > 0$ such that for all $t > t_1 > 0$,

$$\left| \left(\tilde{k}_{hyd} \frac{x_8(t)}{\tilde{K}_c + x_8(t)} x_3(t) x_4(t) + k_{dp2} \zeta x_7(t) \right) - \left(\tilde{k}_{hyd} \frac{\nu}{\tilde{K}_c + \nu} \xi_3 \xi_4 + k_{dp2} \zeta \xi_7 \right) \right| < \varepsilon. \quad (107)$$

Such a t_1 exists by (45), (93), (98), and (105). Note also for t sufficiently larger than t_1 , the following conditions hold:

- (i) $e^{-\int_0^t k_{dp1} ds} x_6(0) < \frac{\varepsilon}{2}$
- (ii) $\frac{\tilde{k}_{hyd} + k_{dp2}}{k_{dp1}} e^{-k_{dp1}t} \left[e^{k_{dp1}t_1} - 1 \right] < \frac{\varepsilon}{2}$
- (iii) $e^{-k_{dp1}(t-t_1)} < \varepsilon$.

From (106), we can write

$$x_6(t) = e^{-\int_0^t k_{dp1} ds} x_6(0) + \int_0^{t_1} e^{-\int_s^t k_{dp1} ds} \left(\tilde{k}_{hyd} \frac{x_8(t)}{\tilde{K}_c + x_8(t)} x_3(t)x_4(t) + k_{dp2} \zeta x_7(t) \right) ds \\ + \int_{t_1}^t e^{-\int_s^t k_{dp1} ds} \left(\tilde{k}_{hyd} \frac{x_8(t)}{\tilde{K}_c + x_8(t)} x_3(t)x_4(t) + k_{dp2} \zeta x_7(t) \right) ds.$$

Notice for the above choice of t_1 in (107) and for $t \gg t_1$ such that conditions (i) – (iii) hold, we have

$$e^{-\int_0^t k_{dp1} ds} x_6(0) + \int_0^{t_1} e^{-\int_s^t k_{dp1} ds} \left(\tilde{k}_{hyd} \frac{x_8(t)}{\tilde{K}_c + x_8(t)} x_3(t)x_4(t) + k_{dp2} \zeta x_7(t) \right) ds \\ \leq \frac{\varepsilon}{2} + \frac{\tilde{k}_{hyd} + k_{dp2}}{k_{dp1}} e^{-k_{dp1} t} \left[e^{k_{dp1} t_1} - 1 \right] < \frac{\varepsilon}{2} + \frac{\varepsilon}{2} = \varepsilon. \quad (108)$$

Then for the same choice of t_1 and $t \gg t_1$,

$$\int_{t_1}^t e^{-\int_s^t k_{dp1} ds} \left(\tilde{k}_{hyd} \frac{x_8(t)}{\tilde{K}_c + x_8(t)} x_3(t)x_4(t) + k_{dp2} \zeta x_7(t) \right) ds \\ = \int_{t_1}^t e^{-\int_s^t k_{dp1} ds} \left[\left(\tilde{k}_{hyd} \frac{x_8(t)}{\tilde{K}_c + x_8(t)} x_3(t)x_4(t) + k_{dp2} \zeta x_7(t) \right) \right. \\ \left. - \tilde{k}_{hyd} \frac{\nu}{\tilde{K}_c + \nu} \xi_3 \xi_4 - k_{dp2} \zeta \xi_7 \right] + \tilde{k}_{hyd} \frac{\nu}{\tilde{K}_c + \nu} \xi_3 \xi_4 + k_{dp2} \zeta \xi_7 ds \\ \leq \int_{t_1}^t e^{-\int_s^t k_{dp1} ds} \left(\varepsilon + \tilde{k}_{hyd} \frac{\nu}{\tilde{K}_c + \nu} \xi_3 \xi_4 + k_{dp2} \zeta \xi_7 \right) ds \\ = \frac{\varepsilon + \tilde{k}_{hyd} \frac{\nu}{\tilde{K}_c + \nu} \xi_3 \xi_4 + k_{dp2} \zeta \xi_7}{k_{dp1}} \left[1 - e^{-k_{dp1}(t-t_1)} \right] \\ \leq \frac{\varepsilon + \tilde{k}_{hyd} \frac{\nu}{\tilde{K}_c + \nu} \xi_3 \xi_4 + k_{dp2} \zeta \xi_7}{k_{dp1}}. \quad (109)$$

Hence (108) and (109) together give

$$x_6(t) \leq \varepsilon + \frac{\varepsilon + \tilde{k}_{hyd} \frac{\nu}{\tilde{K}_c + \nu} \xi_3 \xi_4 + k_{dp2} \zeta \xi_7}{k_{dp1}} \quad \forall t \gg t_1. \quad (110)$$

For the above choice of t_1 and $t \gg t_1$,

$$\begin{aligned}
x_6(t) &= e^{-\int_0^t k_{dp1} ds} x_6(0) + \int_0^{t_1} e^{-\int_s^t k_{dp1} ds} \left(\tilde{k}_{hyd} \frac{x_8(t)}{\tilde{K}_c + x_8(t)} x_3(t) x_4(t) + k_{dp2} \zeta x_7(t) \right) ds \\
&\quad + \int_{t_1}^t e^{-\int_s^t k_{dp1} ds} \left(\tilde{k}_{hyd} \frac{x_8(t)}{\tilde{K}_c + x_8(t)} x_3(t) x_4(t) + k_{dp2} \zeta x_7(t) \right) ds \\
&\geq \int_{t_1}^t e^{-\int_s^t k_{dp1} ds} \left(\tilde{k}_{hyd} \frac{x_8(t)}{\tilde{K}_c + x_8(t)} x_3(t) x_4(t) + k_{dp2} \zeta x_7(t) \right) ds \\
&\geq \frac{\tilde{k}_{hyd} \frac{\nu}{\tilde{K}_c + \nu} \xi_3 \xi_4 + k_{dp2} \zeta \xi_7 - \varepsilon}{k_{dp1}} [1 - e^{-k_{dp1}(t-t_1)}] \\
&\geq \frac{\tilde{k}_{hyd} \frac{\nu}{\tilde{K}_c + \nu} \xi_3 \xi_4 + k_{dp2} \zeta \xi_7 - \varepsilon}{k_{dp1}} [1 - \varepsilon].
\end{aligned}$$

Together with (110), this gives

$$\begin{aligned}
\frac{\tilde{k}_{hyd} \frac{\nu}{\tilde{K}_c + \nu} \xi_3 \xi_4 + k_{dp2} \zeta \xi_7 - \varepsilon}{k_{dp1}} [1 - \varepsilon] &\leq x_6(t) \\
&\leq \varepsilon + \frac{\varepsilon + \tilde{k}_{hyd} \frac{\nu}{\tilde{K}_c + \nu} \xi_3 \xi_4 + k_{dp2} \zeta \xi_7}{k_{dp1}} \quad \forall t \gg t_1.
\end{aligned}$$

Once again, taking $\varepsilon \rightarrow 0$ forces $t \rightarrow \infty$, giving the desired result:

$$\lim_{t \rightarrow \infty} x_6(t) = \frac{\tilde{k}_{hyd} \frac{\nu}{\tilde{K}_c + \nu} \xi_3 \xi_4 + k_{dp2} \zeta \xi_7}{k_{dp1}} = \xi_6.$$

■

We have therefore concluded global asymptotic stability of the unique steady state solution ξ within the region defined in Propositions III.2.1 and III.2.2.

CHAPTER IV

NUMERICAL MODEL ANALYSIS

IV.1 Introduction

We now turn our focus to the numerical analysis of our model. The first half of this chapter is devoted to the techniques of nonlinear parameter estimation used to estimate unknown rate parameters from experimental data. We then provide a comparison of model simulations with empirical data followed by a discussion of which parameters were used to fit which aspects of the experimental data.

In the second half of this chapter we focus on the sensitivity of our model output to the rate parameters, which here we will refer to as *input variables*. Sensitivity analysis techniques are valuable tools designed to answer questions regarding which of the uncertain input variables is more important in determining the uncertainty in the model output. Likewise, sensitivity analysis can provide insight into which parameters should be studied in more detail in order to reduce the most variance in the model output [65]. The ability to answer these types of questions could lead to important insight into the design of new experiments and in determining which experiments would give us the most valuable information.

The most frequently used sensitivity analysis techniques consist of *local* measures of the effect of a given input variable on a particular output of the model [66]. This type of analysis is usually obtained by either directly or indirectly computing system derivatives $S_j = \partial Y / \partial M_j$, where Y is the output of interest and M_j , $j = 1, \dots, k$, is an input variable [38, 75]. This technique provides the effect of varying one input variable while all other variables remain fixed, thus falling under the class of the one-factor-at-a-time (OAT) methods. These methods are only effective if the model is linear in all of its input variables and therefore have limited use and can often provide misleading information for nonlinear models. Therefore, we have instead chosen to use

the Standardized Regression Coefficients (SRCs) obtained by performing regression analysis as a means of sensitivity analysis, since the use of SRCs is considered to be more of a *global* technique, offering a measure of sensitivity that is multi-dimensionally averaged over the entire space of parameter values. Indeed, SRCs are preferable over the normal derivatives, S_j , as they give insight into the degree of nonlinearity in the model and also provide a measure of the effect of a particular input variable, M_j , averaged over a range of possible values for M_j , instead of being computed at a single fixed value of M_j , as is the case for the S_j .

This technique of calculating SRCs first requires the generation of a sample matrix of dimension $n \times k$, where n is the user-defined number of samples to be taken from the sample space (the space consisting of the probability distributions of each parameter value), and k is the total number of input variables considered in the sensitivity analysis. We first discuss our choice of sample generation, followed by the methodology behind regression analysis as a means of calculating sensitivity. We conclude with an explanation of our particular implementation of these methods and a discussion of the results from our analysis.

IV.2 Estimation of Unknown Rate Parameters from Experimental Data

IV.2.1 Numerical Methods

Our system of ordinary differential equations was integrated using the MATLAB solver `ode15s`, which is a variable order solver based on the numerical differentiation formulas (NDFs) [71]. Once an exhaustive search through the literature for known rate parameters was performed, unknown rates were estimated using SIMULINK, which estimates the parameters by minimizing a user-specified cost function via a user-specified optimization method [44]. We chose the nonlinear least squares optimization method of Levenberg-Marquardt to minimize a sum of squared errors cost function of the empirical observations and model predictions for IP_3 , Ca^{2+} , and multiple species of DAG.

In order to perform the nonlinear parameter estimation in SIMULINK, we first created the SIMULINK model shown in Figure 4 to recreate our original (dimensionalized) system of nonlinear ordinary differential equations.

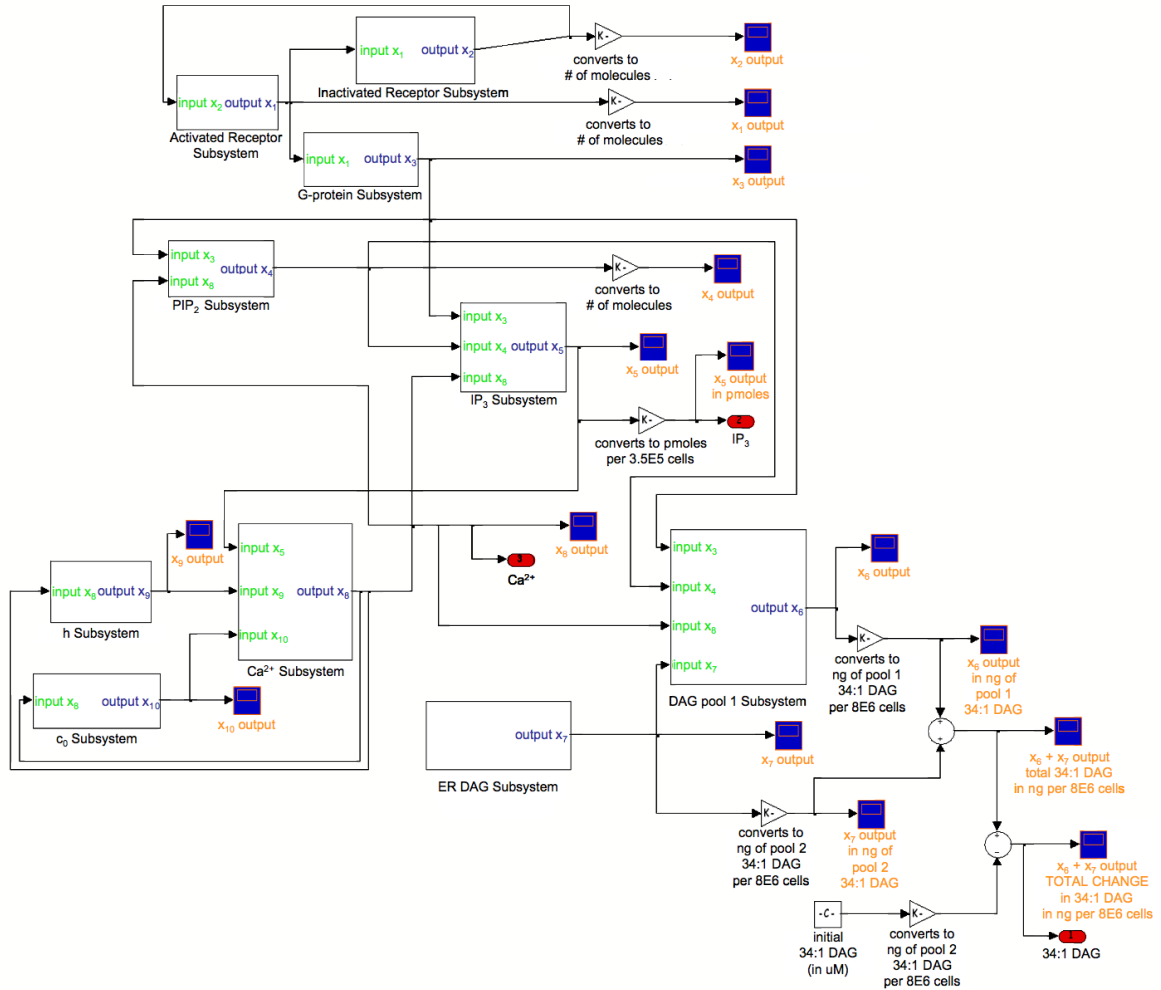


Figure 4: SIMULINK model used in the estimation of unknown rate parameters to simultaneously fit IP_3 , Ca^{2+} , and DAG data.

Each “subsystem” in the SIMULINK model represents an ODE for each variable in the original model. Interactions within each subsystem are shown in Appendix A, Figures 32 through 41. Each block joined by connectors performs a specific function on the value fed into the block and outputs the result from the specific operation. A

list of blocks used in our SIMULINK model along with the function of each is shown in Figure 42 of Appendix A.

IV.2.2 Experimental Methods

In this section we provide a detailed explanation of the experimental methods used to obtain the time-based data for DAG, IP₃, and Ca²⁺.

For the diacylglycerol assay, RAW 264.7 cells used by the Alliance for Cellular Signaling (AfCS) were obtained from the American Type Culture Collection (ATCC catalog number TIB-71, lot number 2263775). For ligand stimulation, 4×10^6 RAW 264.7 cells were plated in 4 ml RAW Growth Medium 1 (DMEM supplemented with 10% FBS, 2 mM L-glutamine, and 20 mM NaHEPES, pH 7.4) per 60 mm TC-treated dish (Falcon). Cells were grown overnight in 5% CO₂ and the medium replaced with 3.6 ml serum-free assay medium (DMEM containing 2 mM L-glutamine, 20 mM NaHEPES, pH 7.4, and 0.1 mg/ml bovine serum albumin) for 1 hr. After 1 hr serum-starvation, cells were stimulated with 0.4 ml serum-free medium (control) or 10x ligand (25 μ M UDP) in a 37°C glove box for the indicated times. The medium was aspirated on ice, cells were washed with 2 ml ice-cold PBS, aspirated again and resuspended in 0.8 ml ice-cold PBS by scraping. The cell suspension was transferred to a cold 1.5 ml PCR tube (Laboratory Products) and centrifuged for 5 min at 1000 x g, 4°C. The PBS was aspirated and the pellets were frozen and stored in dry ice. Phospholipids were extracted using a modified Bligh/Dyer procedure [5]. Ice-cold 1:1 0.1N HCl:CH₃OH (800 μ L) was added to each cell pellet, and the suspensions were transferred to individual cold 12 \times 75 mm borosilicate glass test tubes. 24:0 DAG (10 μ L, 10 μ g/mL, Avanti Polar Lipids) was added to all samples as an internal standard. After addition of 400 μ L ice-cold CHCl₃ and thorough mixing, phospholipids were collected from the lower (organic) phase after layer separation by centrifugation. Diacylglycerol isolation from phospholipid extracts and species-specific diacylglycerol

quantification using electrospray ionization mass spectrometry was achieved according to the procedures described in Callender et al. [10].

Next, for the IP₃ binding assay, lysates from RAW 264.7 cells were assayed using the [³H] Biotrak assay kit from GE Healthcare, based on a competitive radioreceptor assay [53]. RAW 264.7 cells were grown in 60 mm dishes and stimulated as described in Callender et al. [10]. Cells were washed with 2 ml ice-cold PBS, aspirated and lysed by scraping in 250 μ l 5.4% perchloric acid on ice. Cell lysates were transferred to 1.5 ml microfuge tubes and assayed according to the manufacturer’s instructions. [IP₃] is calculated as pmols/100 μ l lysate.

Finally, for the intracellular free calcium assay, data were obtained by measuring the fluorescent emission at 538 nM of RAW 264.7 cells loaded with fluo-3 acetoxymethyl (Molecular Probes). Fluorescence measurements were performed using a Fluoroskan Ascent microplate fluorometer with the Ascent software (Thermo-Labsystems), according to AfCS Procedure Protocol PP00000176, described in detail on the AfCS website: <http://www.signaling-gateway.org>. Intracellular free calcium data for RAW 264.7 cells stimulated with 25 μ M UDP were obtained from the AfCS single ligand screen [49], and are also available on the AfCS website.

All IP₃ and Ca²⁺ data were collected by the AfCS cell laboratory at the University of Texas Southwestern.

IV.2.3 Parameter Estimation

Experimental observations of P2Y₆ receptor dynamics from Brinson and Harden in 1321N1 astrocytoma cells [6] and IP₃, Ca²⁺, and species-specific DAG measurements of the response to 25 μ M UDP in RAW 264.7 cells are all used to compare with the simulations obtained from the system of ten nonlinear ordinary differential equations described in Chapter II (using equations (25) and (26) for the DAG module) and to aid in the estimation of unknown rate parameters. Table 4 includes a list of all model parameters, their values, and a reference for those taken from the literature.

Table 4: Time-independent model variables

Parameter	Value	Reference
[L]	25 μM	
N_{RT}	20000	[21, 43]
K_1	5 μM	[39, 41]
K_2	100 μM	[39]
k_r	$1.75 \times 10^{-4} s^{-1}$	[39]
k_p	$1.75 \times 10^{-3} s^{-1}$	see text
k_e	$6 \times 10^{-3} s^{-1}$	[39]
N_{GT}	3×10^5	[19]
k_a	$0.137 \mu\text{M}^{-1} s^{-1}$	[19]
k_d	$0.02 s^{-1}$	[43]
N_{PIP_2T}	9×10^6	see text
v	$5 \times 10^{-13} L$	[68]
K_c	0.4 μM	[19, 39]
\hat{k}_{hyd}	$1 \times 10^{-5} \# \text{mol}^{-1} s^{-1}$	see text
k_{rep}	$0.014 s^{-1}$	see text
k_{d3}	$6 \times 10^{-3} s^{-1}$	see text
N_{DAGp_2T}	480 (500) μM	see text
k_{dp1}	$7.37 \times 10^{-3} s^{-1}$	see text
	$(1.2 \times 10^{-3} s^{-1})^a$	
k_{dp2}	$5.4 \times 10^{-3} s^{-1}$	see text
	$(1.71 \times 10^{-3} s^{-1})^a$	
k_{ap2}	$1.08 \times 10^{-2} s^{-1}$	see text
	$(1.96 \times 10^{-3} s^{-1})^a$	
η	0.66 (0.45) ^a	see text
ϵ	0.01	[16, 40]
d_{IP_3}	0.2 μM	[40]
d_{act}	0.4 μM	[40]
d_{inh}	0.02 μM	[39]
a	$3.1 s^{-1}$	see text
ν_1	$40 s^{-1}$	[40]
ν_2	$5.08 \times 10^{-3} s^{-1}$	see text
ν_3	$0.24 \mu\text{M} s^{-1}$	[40]
ν_4	$1.4 \mu\text{M} s^{-1}$	see text
k_{er}	0.4 μM	[39]
k_{pl}	$1.56 \times 10^{-2} \mu\text{M}$	see text
j_{in}	$0.447 \mu\text{M} s^{-1}$	see text
c_1	0.185	[16]

^aParameter values not in parentheses correspond to 38:4 DAG, while those in parentheses are for 34:1 DAG.

Of these 34 parameters, 18 are taken from the literature, 2 are directly measured, and 14 are estimated from experimental data.

The primary focus of this work is on the differential mechanisms of species-specific DAG production and degradation. Time-series data for the 38:4 DAG and 34:1 DAG responses to 25 μM UDP are shown in Figures 5a and 5b, respectively. Solid grey

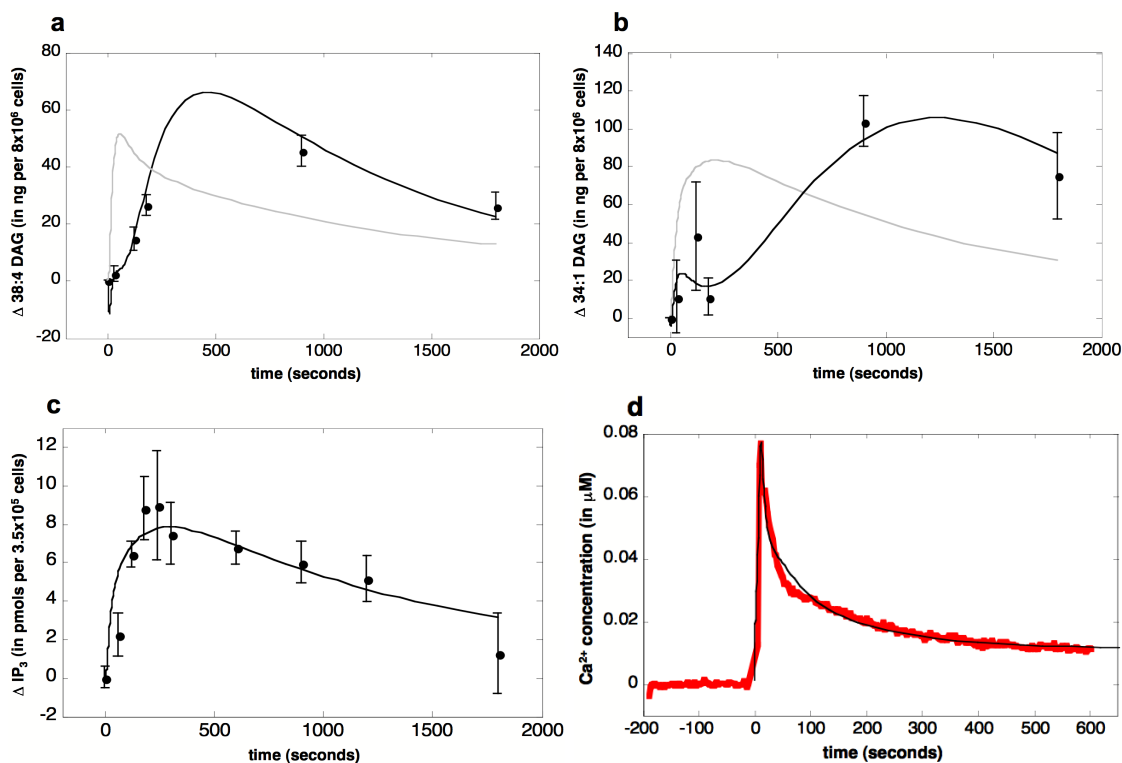


Figure 5: Timecourse of stimulation with 25 μM UDP in RAW 264.7 cells. Solid black lines represent model simulations for the system of equations using the two-pool model (with equations (25) and (26)), while gray lines represent simulations using the canonical pathway for DAG (equation (24)). (a) 38:4 DAG response (representative of the response of most poly unsaturated fatty acid-containing DAG species). (b) 34:1 DAG response (representative of the response of most mono- and di-unsaturated fatty acid-containing DAG species). Data points in (a) and (b) contain nine replicates performed on three different experimental days, with error bars = 1 SEM. Units are total change in ng over baseline levels in $\sim 8 \times 10^6$ cells. (c) IP_3 response in pmols per $\sim 3.5 \times 10^5$ cells. Points represent the average of four experiments, and error bars are 1 SEM. (d) Ca^{2+} response in μM . Red curve is a representative Ca^{2+} trace taken from the UDP experiments within the AfCS single ligand screen as described in the “Intracellular free calcium assay” portion of Section IV.2.2.

lines are derived from numerical simulations of our initial DAG model (using equation (24)), while solid black lines are derived from numerical simulations of the combined effect of DAG from pools 1 and 2, as described in Section II.3. As the method used for quantification of DAG species measures change in total cellular DAG over baseline levels, DAG response is simulated by adding the outputs from equations (25) and (26). Data points and error bars correspond to experimental values obtained using the DAG assay as described in Section IV.2.2. Although the second and larger rise phase is observed in most of the DAG species, the early kinetic behavior, within the first three minutes of stimulation, varies quite drastically between PUFA-containing DAGs and mono- and di-unsaturated DAGs. PUFA-containing DAGs, such as 38:4 DAG, are consistently seen as increasing immediately upon stimulation, while mono- and di-unsaturated species, such as 34:1 DAG, display an immediate and small peak (~ 43 ng for 34:1 DAG) two minutes after stimulation and then exhibit a brief yet almost full recovery by 3 minutes which is followed by a larger production (~ 104 ng for 34:1 DAG) at 15 minutes. All DAG species have begun to recover by the 30 minute time point.

We make note here that in approximately 30% of the experimental cases, total DAG levels in many of the mono- and di-unsaturated species are seen to actually decrease significantly below baselines levels within the first 3 minutes of stimulation (data not shown). Although the reason for this variation in response could not be determined, according to the two-pool model structure, this would suggest a more rapid phosphorylation of DAG_{p2} such that initial production of DAG_{p1} is more than offset by early conversion of DAG_{p2} resulting in a net loss of total DAG until enough DAG_{p2} has been converted to aid in PIP_2 replenishment. By increasing the value of k_{dp2} , our model can accurately reproduce this kinetic behavior.

As seen in Figure 5, different species of DAG have been shown to respond differently to P2Y_6 stimulation, suggesting different rates of conversion or degradation from both pools as well as different initial values and rates of production of DAG

from the second pool. The rate of degradation of DAG_{p2}^i , k_{dp2}^i (where, as mentioned earlier in Section II.3, the superscript i refers to a particular species of DAG), was estimated to fit the early behavior of different DAG species. In particular, for species showing an early rise phase followed by a recovery to baseline by ~ 3 minutes, such as 34:1 DAG (Fig. 5b), k_{dp2}^i sets the level and time of recovery. The degradation rate of DAG_{p1}^i , k_{dp1}^i , and production rate of DAG_{p2}^i , k_{ap2}^i , were then used to set the size and time of the peak observed at later time points. As η^i represents the fraction of DAG_{p2}^i contributing to the resynthesis of DAG_{p1}^i through the two-pool model (Fig. 2), this parameter was chosen to fit the overall magnitude of DAG response throughout the timecourse. The initial concentration of resting DAG_{p2}^i levels in the RAW 264.7 cell, $N_{\text{DAG}_{p2}^i}$, was estimated from the methods developed in Callender et al. [10].

Figure 5c displays the total synthesis of IP_3 over baseline levels in response to $25\mu\text{M}$ UDP over a timecourse of 30 minutes. The solid line represents the solution to equation (23) with initial condition $N_{\text{IP}_3}(t) = 0$, as we assume no change in number of IP_3 molecules for times $t \leq 0$ (i.e., before ligand addition). Data points with error bars are experimental values obtained from the IP_3 assay described in Section IV.2.2. Results show that IP_3 peaks within the first 3-4 minutes (~ 9 pmoles) and remains above baseline levels throughout the tested timecourse, suggesting prolonged stimulation of receptors and hydrolysis of PIP_2 molecules.

Total PIP_2 per cell, N_{PIP_2T} , was determined by direct infusion mass spec using a 16:0 PIP_2 standard. The rate of IP_3 degradation, k_{d3} , was used to fit the IP_3 peak time and height observed from the experimental data, while the rates of receptor phosphorylation, k_p , effective PIP_2 hydrolysis, \hat{k}_{hyd} ($= k_{hyd}\lambda$), and PIP_2 replenishment, k_{rep} , were all used to simultaneously fit the experimental observations of IP_3 and multiple species of DAG. The parameter k_p was chosen to match the height of recovery at later time points in both IP_3 and DAG. The overall magnitude of DAG throughout the timecourse and the shape of the IP_3 response were fit with \hat{k}_{hyd} , while k_{rep} was taken to match the size of the DAG response after the initial peak and the

peak height of IP_3 .

Parameters for the Ca^{2+} module were either taken from Li and Rinzel [40] or Lemon [39], or they were estimated to obtain a best fit to the experimental data in Figure 5d. Three of the five estimated Ca^{2+} parameters were chosen to lie within ranges of parameters chosen by Li and Rinzel [40]. These include the following: the receptor binding constant for Ca^{2+} -dependent inhibition, a , which sets the size of Ca^{2+} peak; the maximum Ca^{2+} flux out of the cell across the plasma membrane, ν_4 , which helps to determine peak height and width; and Ca^{2+} flux through the plasma membrane, j_{in} , which controls overall magnitude of the Ca^{2+} response. The remaining two parameters are the maximum Ca^{2+} leak flux through the ER, ν_2 , used to help fit the peak height and shape, and the Michaelis constant for Ca^{2+} flux out of the cell across the plasma membrane, k_{pl} , which affects the peak height as well as the sustained level of Ca^{2+} .

Predictions for the remaining model variables, including activated and inactivated P2Y_6 , activated G-proteins, and available PIP_2 , are obtained by solving equations (19) through (22). Figure 6 shows model simulations for these four remaining variables, all in response to $25 \mu\text{M}$ UDP.

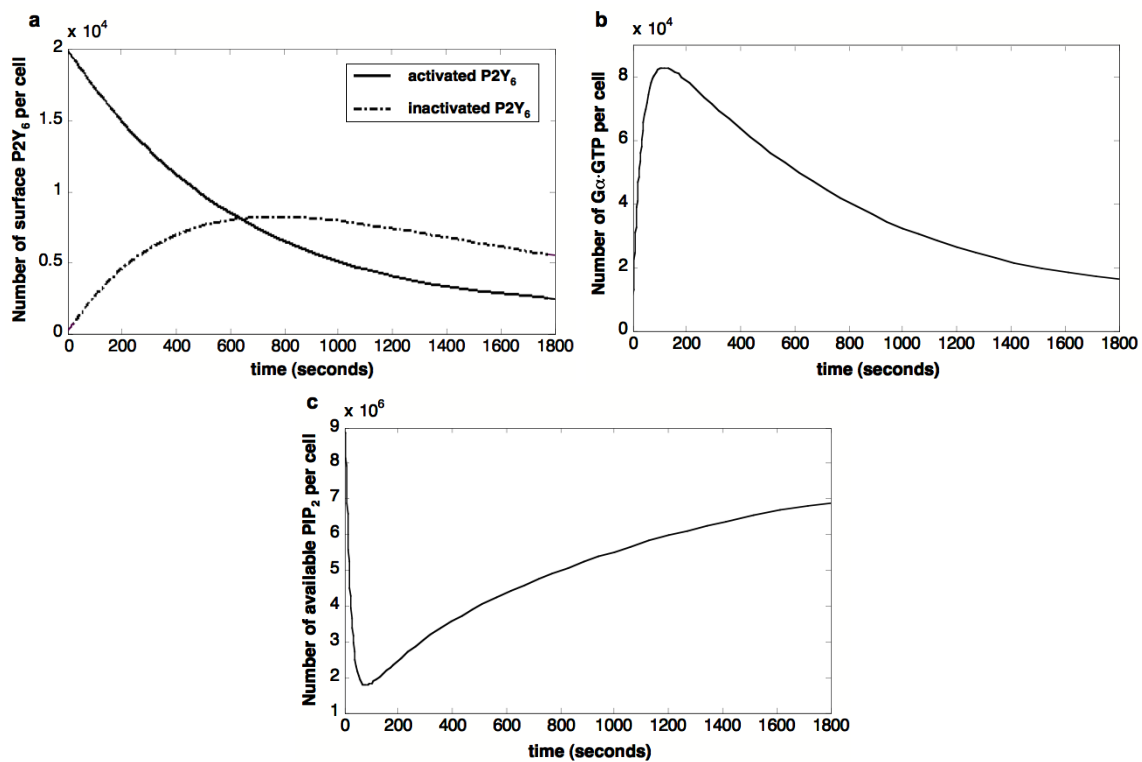


Figure 6: Model simulations for timecourse of stimulation with 25 μM UDP in a single RAW 264.7 cell for remaining model variables. (a) Activated (solid line) and inactivated (dashed line) P2Y₆ surface receptors. (b) Total number of activated G α ·GTP. (c) Total number of PIP₂ available for hydrolysis.

IV.3 Sensitivity Analysis

IV.3.1 Sampling Method and Sensitivity Technique

As mentioned in the previous section, several of the rate parameters could not be obtained from the literature and therefore had to be estimated. Thus, we now examine which parameters in the model are most responsible for model output uncertainty. This can then guide us in determining the parameters for which we may need to obtain better measurements in order to reduce output uncertainty.

In order to perform such a sensitivity analysis, we first generate a random sample of our space of input variables over a ten percent variation from each parameter's nominal value using the Latin Hypercube Sampling (LHS) method. LHS may be considered to be a particular case of stratified sampling, whose main goal is to achieve a better coverage of the sample space of the input variables [28, 47]. In LHS the range of each input variable, denoted M_j , $j = 1, 2, \dots, k$, is divided into n subintervals of equal marginal probability, $1/n$, and one observation of each input variable is taken from each interval using random sampling within that interval. This technique results in n non-overlapping realizations for each of the k input variables. To obtain the first sample, denoted m_1 , one of the realizations on M_1 is randomly selected (each observation is equally likely to be selected), paired with a randomly selected realization of M_2 , and so on all the way out to M_k . For the next sample, m_2 , one of the remaining realizations of M_1 is paired at random with one of the remaining observations of M_2 , and so on. Continuing this procedure, we obtain the remaining samples m_3, \dots, m_n , which exhausts the observations and results in a latin hypercube sample $\mathbf{m} = (m_{ij})$, where $i = 1, \dots, n$ and $j = 1, \dots, k$.

One of the advantages of this sampling method is that it ensures each input variable has all portions of its distribution (which in our case is a uniform distribution) represented by input values. LHS performs better than random (Monte Carlo) sampling when the output is dominated by a few components of the input factors. The method ensures that each of these components is represented in a fully strati-

fied manner, no matter which components might turn out to be important. LHS is also designed to accurately recreate the input distribution through sampling in fewer iterations when compared with the Monte Carlo method.

Once the sample \mathbf{m} is created, propagation of the sample through the model creates a mapping from analysis inputs to analysis results of the form

$$[y_i, m_{i1}, m_{i2}, \dots, m_{ik}] \quad i = 1, \dots, n, \quad (111)$$

where k is the number of input variables (rate parameters), n is the sample size, and y_i is the model output corresponding to sample m_i . Once this mapping is generated and stored, it can be explored in many ways to determine the sensitivity of model predictions to individual input variables.

One of the most common and simplest of sensitivity analysis techniques is the generation of scatter plots, where a plot is generated of the points (m_{ij}, y_i) , $i = 1, \dots, n$, for each independent input variable M_j . Although this technique can provide important information regarding the relationships between model input and model predictions, one disadvantage is that it requires the generation and inspection of a large number of plots. Indeed, one needs at least one plot per input variable, and in our case this needs to be multiplied by the number of time points since our model output is time-dependent. Furthermore, scatterplots offer only a qualitative measure of the sensitivity, as the relative importance of each variable cannot be quantified.

In order to obtain a more quantitative global sensitivity analysis, we have chosen the measure of standardized regression coefficients (SRCs) determined from multiple regression analysis. Here the multivariate sample \mathbf{m} of the input variables is generated by the LHS sampling strategy (dimension $n \times k$), and the corresponding sequence of n output values is computed using our model equations, resulting in the mapping

discussed above (111). We then seek a linear regression model of the form

$$y_i = b_0 + \sum_j b_j m_{ij} + \varepsilon_i$$

where y_i , $i = 1, \dots, n$, are the output values of the model, b_j , $j = 1, \dots, k$, are coefficients to be determined and ε_i is the error, or *residual*, due to the approximation. A common way of determining the coefficients b_j is to use the method of least squares, where the coefficients b_j are determined so as to minimize the function

$$F(b) = \sum_i \varepsilon_i^2.$$

After the b_j , $j = 1, \dots, k$, are computed, they can be used to indicate the importance of individual input variables M_j with respect to the uncertainty in the output y . Since the b_j are dimensionalized coefficients, it is common practice to rewrite the regression model in its nondimensionalized form:

$$\frac{(\hat{\mathbf{y}} - \bar{y})}{\hat{s}} = \sum_j \left(\frac{b_j \hat{s}_j}{\hat{s}} \right) \left(\frac{\mathbf{m}_j - \bar{m}_j}{\hat{s}_j} \right),$$

where

$$\begin{aligned} \bar{y} &= \sum_i \frac{y_i}{n}, & \bar{m}_j &= \sum_i \frac{m_{ij}}{n} \\ \hat{s} &= \left[\sum_i \frac{(y_i - \bar{y})^2}{n-1} \right]^{1/2} \\ \hat{s}_j &= \left[\sum_i \frac{(m_{ij} - \bar{m}_j)^2}{n-1} \right]^{1/2}, \end{aligned}$$

and where $\hat{\mathbf{y}}$ is the vector of regression model predictions, and \mathbf{m}_j is the j^{th} column vector in the LHS sample matrix. The coefficients $b_j \hat{s}_j / \hat{s}$ are the SRCs that we will use for sensitivity analysis. The SRCs enable us to quantify the effect of varying each input variable away from its mean by a fixed fraction of its variance while maintaining all other variables at their expected values.

We make note here that in order to use the SRCs as a measure of sensitivity, it is also important to consider the *model coefficient of determination*, R_y^2 , given by

$$R_y^2 = \frac{\sum_{i=1}^n (\hat{y}_i - \bar{y})^2}{\sum_{i=1}^n (y_i - \bar{y})^2}$$

where \hat{y}_i is the estimate of y_i obtained from the regression model. R_y^2 gives a way of determining how close the linear regression model based on the SRCs comes to reproducing the actual model output y . It represents the fraction of the variance of the output explained by the regression, and the closer it is to one, the better is the regression model's performance and the more valid SRCs are in determining sensitivity of input variables. Therefore, in order to be able to use SRCs as a measure of sensitivity, one must first determine the R_y^2 values, for if any of the R_y^2 (one is computed for each time point in time-dependent models) are less than some threshold value, typically 0.7, the SRCs are not accurate indicators of sensitivity. In this case, *model-free* methods can be used. Examples of such methods include but are not limited to the following methods described in detail in [65, 67]: the method of Morris, the FAST method, the importance measure, and the method of Sobol'.

IV.3.2 Implementation of the Sensitivity Methods

An LHS sample matrix was found using the coding environment `SIMLAB 3.0.x`, which consists of a `MATLAB` m-file that, when called, will create a sample matrix based on a user-specified sampling method. We therefore created an m-file which loaded parameters and their probability distributions (uniform distribution with 10% variation from nominal value) and subsequently called the Latin Hypercube sampling code, thus generating the LHS sample matrix. The m-file for this sample creation can be found in Appendix B.

Another m-file was created to take as input each row, m_i , $i = 1, \dots, n$ of the sample matrix and output the corresponding outputs, $y_i^{(l)}$, $l = 1, \dots, 10$, for each of the original ten variables in the dimensionalized form of the model equations. R_y^2

values and SRCs were then computed using the MATLAB *regress* function. R_y^2 values for all model outputs and all time points from 0 to 30 minutes were greater than 0.8 and in most cases were very close to one (see, for example, the insets in Figures 8 and 7, which show graphs of the time-dependent R_y^2 values for DAG and IP₃, respectively), ensuring that the SRCs are good measures of sensitivity. The most sensitive parameters are therefore those whose SRCs, in absolute value, are the largest. As different input variables affect the model output differently at different times, certain parameters are seen to be more sensitive at early time points, while others are more sensitive at later time points. The time-dependent SRCs corresponding to the most sensitive parameters for IP₃ and DAG = DAG_{p1} + DAG_{p2} are shown in Figures 7 and 8, respectively.

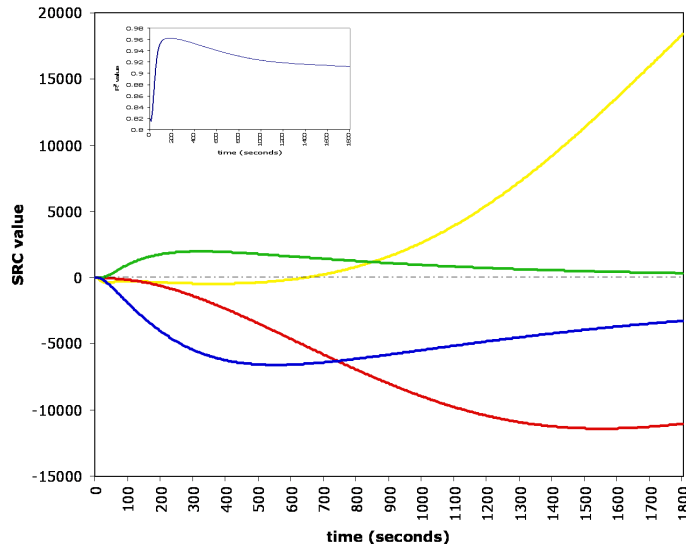


Figure 7: Standardized Regression Coefficients (SRCs) corresponding to most sensitive parameters for IP₃. Most sensitive parameters are as follows: receptor rate of phosphorylation, k_p (■), receptor recycling rate, k_r (■), PIP₂ replenishment rate, k_{rep} (■), and IP₃ degradation rate, k_{d3} (■). Inset: R_y^2 values for all time points are ≥ 0.8 , ensuring that the SRCs for IP₃ are good measures of sensitivity.

Figure 7 reveals that early IP₃ output is most sensitive to changes in the rate of degradation of IP₃, k_{d3} , which has a negative effect, and the PIP₂ replenishment

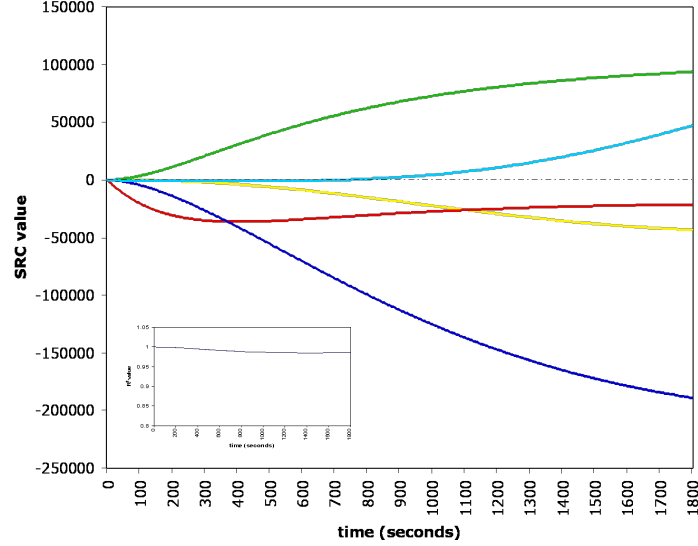


Figure 8: Standardized Regression Coefficients (SRCs) corresponding to most sensitive parameters for DAG. Most sensitive parameters are as follows: degradation rate of DAG_{p1} , k_{dp1} (■), production rate of DAG_{p2} , k_{ap2} (■), degradation rate of DAG_{p2} , k_{dp2} (■), receptor rate of phosphorylation, k_p (■), and receptor recycling rate, k_r (■). Inset: Since R_y^2 values for all time points are ≥ 0.95 , the SRCs for DAG are good measures of sensitivity.

rate, k_{rep} , which has a positive effect. At early time points (0 to 650 seconds) the receptor recycling rate, k_r , shows a slight negative effect; however, from 850 to 1800 seconds, k_r becomes the parameter with the strongest positive influence on IP_3 . The parameter most negatively affecting IP_3 production at later time points is the rate of receptor phosphorylation, k_p .

As shown in Figure 8, the dynamics of DAG are mostly driven by the DAG kinetic parameters of activation and degradation. For the first ~ 400 seconds after stimulation, output of DAG is most sensitive to the rate of degradation of DAG_{p2} , k_{dp2} , with this parameter having a negative influence on DAG production. Although the receptor phosphorylation rate, k_p , shows a small yet significant negative effect at later time points, the most sensitive parameter with negative effects from 400 to 1800 seconds is the DAG_{p1} degradation rate, k_{dp1} . Those parameters with the strongest positive influence are the DAG_{p2} production rate, k_{ap2} , and to a lesser extent the receptor recycling rate, k_r .

Since from the sensitivity analysis k_{dp2} , k_{ap2} , and k_{dp1} were determined to be the most sensitive parameters for DAG output, Figures 9, 10, and 11 were generated to better visualize the effects of varying each of these parameters about its nominal value given in Table 4. Each figure displays the change in 34:1 DAG response to a 50% fluctuation in one of these three parameters. From Figure 9, we see that the rate of phosphorylation in the second pool of DAG, k_{dp2} , greatly affects the level of early decrease in DAG levels over baseline. Further, while the effects of the rates of pool 2 DAG replenishment and pool 1 DAG degradation resemble one another, their effects are negatives of one another, as reflected by the SRC graph from Figure 8. Indeed, a *rise* in the activation rate k_{ap2} causes an overall increase in DAG and a slower recovery to baseline at later time points, where a similar DAG increase is found by a *decrease* in the degradation parameter k_{dp1} .

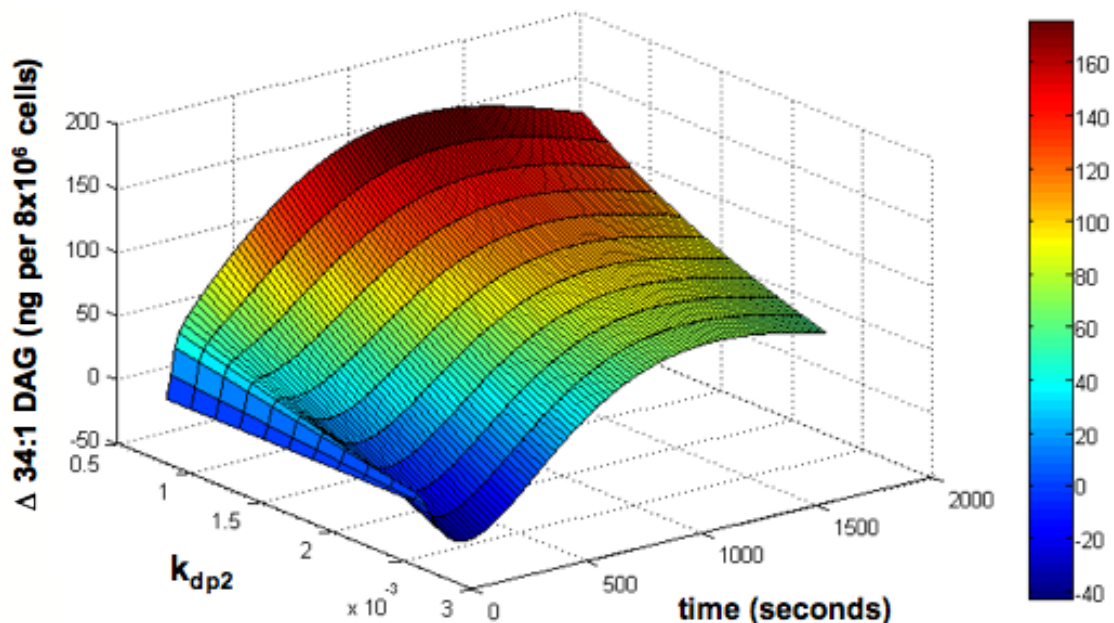


Figure 9: Changes in 34:1 DAG response to 50% variations in k_{dp2} , the rate of degradation of pool 2 DAG, from its nominal value of 1.71×10^{-3} .

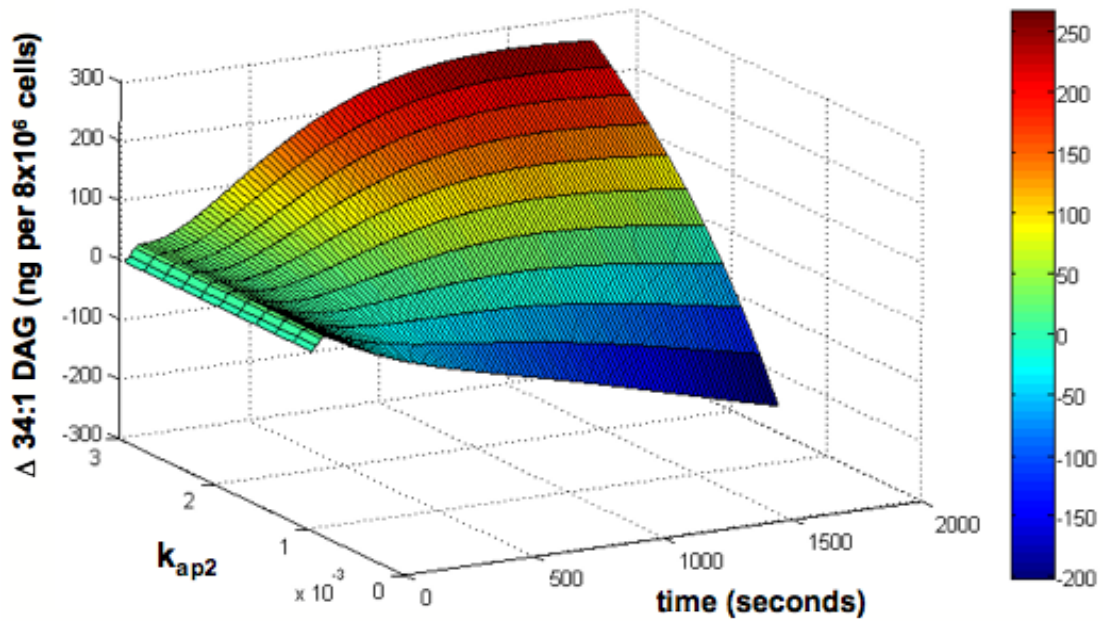


Figure 10: Changes in 34:1 DAG response to 50% variations in k_{ap2} , the rate of degradation of pool 2 DAG, from its nominal value of 1.96×10^{-3} . Note here that the axis for k_{ap2} is in reverse order from the axes for k_{dp2} and k_{dp1} as shown in Figures 9 and 11, respectively.

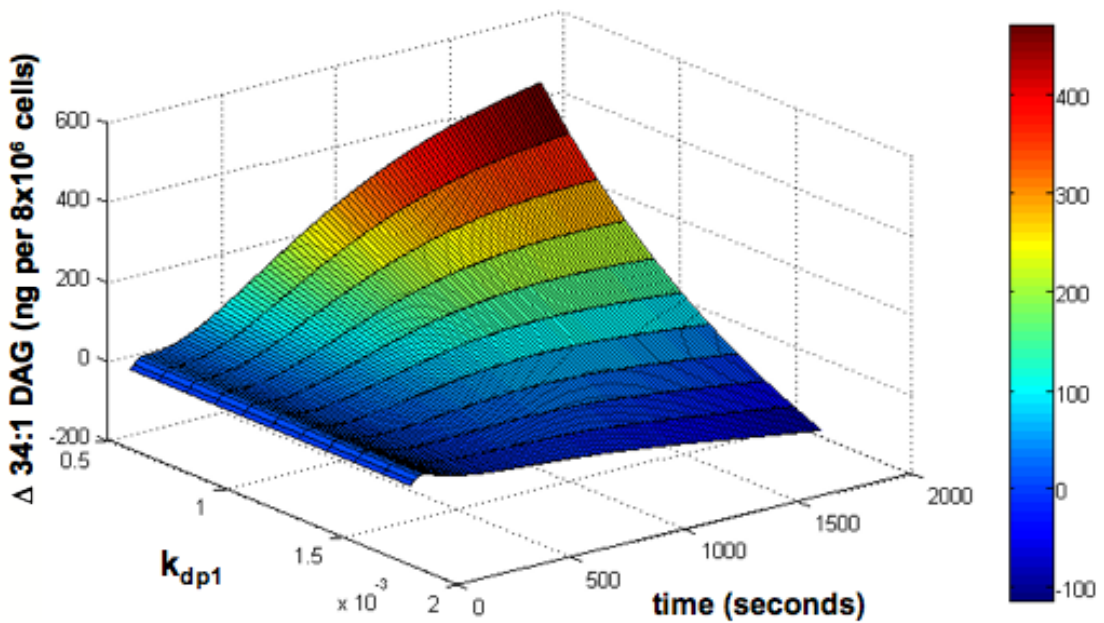


Figure 11: Changes in 34:1 DAG response to 50% variations in k_{dp1} , the rate of degradation of pool 2 DAG, from its nominal value of 1.2×10^{-3} .

CHAPTER V

DIACYLGLYCEROL PATHWAY ANALYSIS

V.1 Introduction

In this chapter we present experimental evidence that supports the two-pool DAG model shown in Figure 2 and described in Section II.3. The data were obtained from experiments performed on RAW 264.7 macrophages in collaboration with Paul Sternweis and Dianne DeCamp at the University of Texas Southwestern. The data discussed in Section V.2 include a comparison of the DAG response from two doses of UDP (250 nM and 25 μ M). The second data set, covered in Section V.3, includes results from our investigation of the role of DAG kinase (DAGk) in DAG production over the timecourse of 30 minutes, through inhibition of this enzyme with the DAGk inhibitor II, also called R59949. In Section V.4 we discuss the third data set containing results from a multiple inhibitors study, where we have tested several different inhibitors of DAG metabolism, including U73122 (inhibits phosphoinositol (PI)-specific PLC activity), U73433 (inactive analog of U73122), Propranolol (most widely known as a beta-adrenergic receptor antagonist, but also inhibits conversion of PA to DAG via lipid phosphate phosphatase (LPP)), R59949 (DAGk inhibitor II), and Thimerosal (inhibits conversion of monoacylglycerol (MAG) to DAG via monoacylglycerol acyltransferase (MGAT) as well as CoA-independent and CoA-dependent acyl transferases [64]). The results of the experiments from Section V.4 suggested further studies on the effects of Propranolol, which are discussed in Section V.5. For these experiments we ran the same time course as for R59949 in Section V.3, with and without 25 μ M UDP, with and without 150 μ M Propranolol.

V.2 Two-Dose UDP Experiments

The graphs of several DAG species in response to UDP stimulation are shown in Figure 12. Each graph shows the total change in DAG (in ng) over baseline levels, for two concentrations of UDP: 250 nM (in green squares) and 25 μ M (in red triangles). The cells were stimulated for 30s, 2min, 3min, 15min, and 30min. This timecourse was chosen after preliminary experiments revealed these times to display the most significant aspects of the cellular DAG response (e.g., the DAG response from 3 to 15 minutes was essentially linear). Each data point is the average of nine experimental repeats performed on three different experimental days. Error bars represent 1 SEM.

For all 29 DAG species measured, the fold changes and p-values for all time points and for both doses of UDP are given in Figures 13 and 14.

In this data set, no species was found to be significantly decreasing over baseline levels at any point in the tested timecourse. The most notable difference in the two doses is at the 15 minute time point, where the higher dose produces a larger increase in most of the responding DAG species. Furthermore, for the higher dose of UDP, the response peaks at 15 minutes and begins to recover by 30 minutes. For the lower dose, however, many species are either still increasing or not decreasing as rapidly by 30 minutes. This suggests that with the lower dose the cells are responding more slowly than with the higher dose.

V.3 DAG Kinase Inhibitor II (R59949) Experiments

In order to further investigate the origin of DAG responses to UDP, we collected data on the DAG response to UDP with and without pretreatment of the DAG kinase inhibitor II (R59949). Purkiss and Boarder [58] suggest the existence of two pathways by which purinergic-receptor-mediated stimulation (in endothelial cells) may give rise to PA: sequential activation of PLC and DAGk, or directly via PLD. They then have evidence showing that PA derived from both routes is readily metabolized to DAG. This could explain why we are seeing DAG levels rising at later time points than the

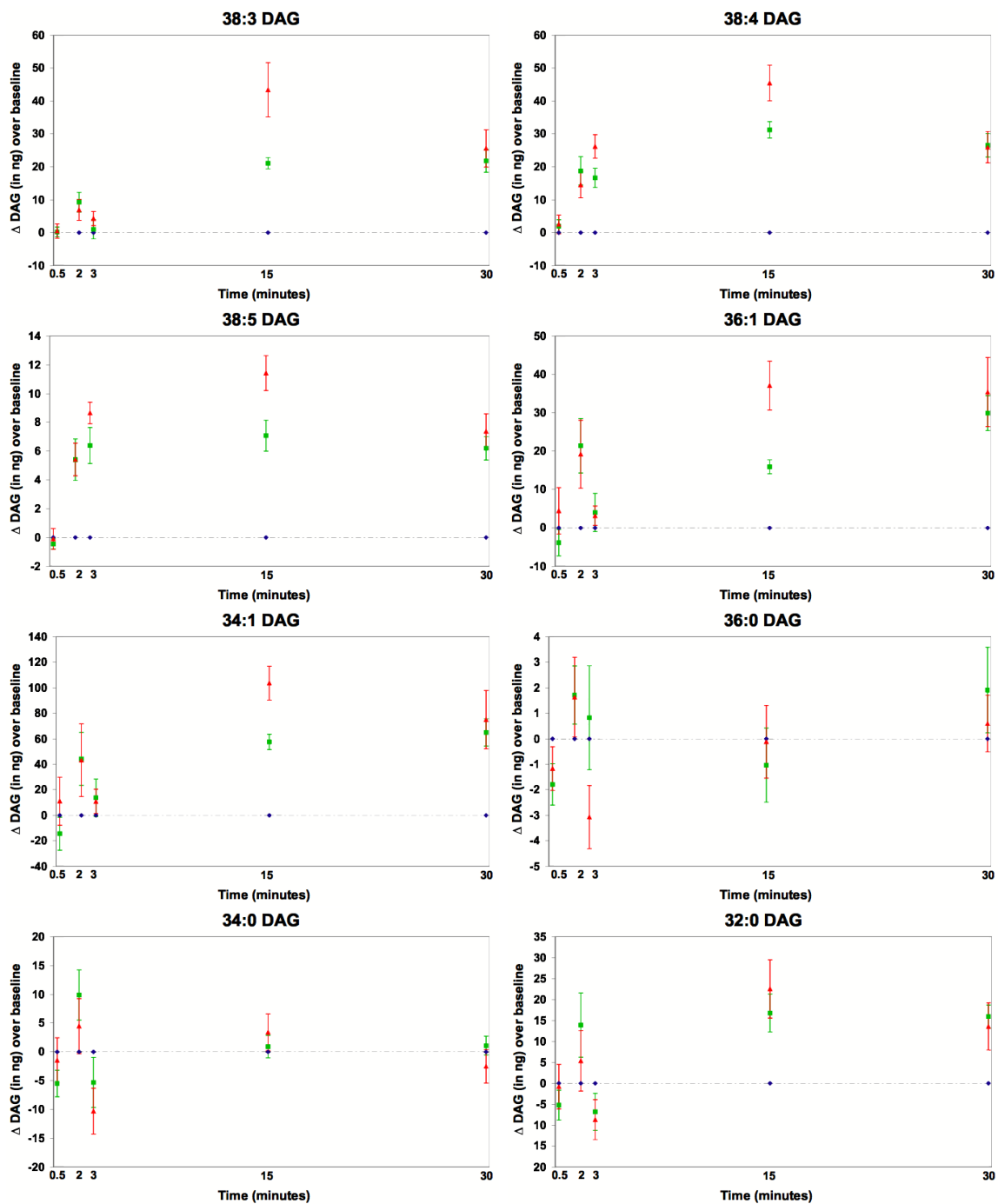


Figure 12: Total change in DAG (in ng) over baseline levels, for two concentrations of UDP: 250 nM (in green squares) and 25 μM (in red triangles). The cells were stimulated for 30s, 2min, 3min, 15min, and 30min. Each data point is the average of nine experimental repeats performed on three different experimental days. Error bars represent 1 SEM.

250nM UDP vs basal												
	fold change		p-value		fold change		p-value		fold change		p-value	
	0.5min	0.5min	2min	2min	3min	3min	15min	15min	30min	30min		
38:0 DAG	1.00	0.97	1.07	0.27	1.15	0.46	1.06	0.57	1.13	0.19		
38:1 DAG	0.95	0.11	1.05	0.23	1.00	0.94	0.97	0.26	0.98	0.49		
38:2 DAG	0.96	0.10	1.13	0.01	1.02	0.62	1.01	0.78	1.03	0.38		
38:3 DAG	1.01	0.81	1.22	0.00	1.09	0.43	1.55	0.00	1.53	0.00		
38:4 DAG	1.03	0.54	1.33	0.00	1.36	0.00	1.67	0.00	1.52	0.00		
38:5 DAG	0.98	0.46	1.31	0.00	1.44	0.00	1.47	0.00	1.37	0.00		
38:6 DAG	0.98	0.75	1.16	0.05	1.23	0.15	1.16	0.04	1.31	0.02		
36:0 DAG	0.93	0.20	1.07	0.17	1.04	0.72	0.96	0.68	1.09	0.35		
36:1 DAG	0.98	0.45	1.14	0.00	1.04	0.45	1.13	0.00	1.21	0.00		
36:2 DAG	0.98	0.60	1.13	0.01	1.13	0.01	1.29	0.00	1.27	0.00		
36:3 DAG	1.00	0.97	1.16	0.09	1.18	0.02	1.29	0.00	1.32	0.00		
36:4 DAG	1.05	0.37	1.24	0.02	1.34	0.00	1.42	0.00	1.35	0.00		
36:5 DAG	1.06	0.35	1.12	0.19	1.39	0.04	1.16	0.02	1.21	0.00		
34:0 DAG	0.94	0.12	1.11	0.03	0.98	0.74	1.01	0.73	1.01	0.74		
34:1 DAG	0.97	0.45	1.10	0.03	1.04	0.33	1.17	0.00	1.18	0.00		
34:2 DAG	1.00	0.99	1.10	0.07	1.10	0.07	1.19	0.01	1.21	0.00		
34:3 DAG	1.01	0.82	1.12	0.13	1.24	0.02	1.10	0.13	1.21	0.00		
34:4 DAG	1.03	0.59	1.33	0.09	1.11	0.76	1.05	0.46	1.78	0.25		
34:1 DAGe/p	0.97	0.54	1.01	0.87	1.02	0.78	1.02	0.58	1.11	0.06		
32:0 DAG	0.96	0.29	1.11	0.07	0.96	0.40	1.16	0.00	1.17	0.00		
32:1 DAG	0.98	0.64	1.11	0.02	1.03	0.46	1.16	0.00	1.17	0.00		
32:2 DAG	1.04	0.44	1.13	0.04	1.14	0.25	1.09	0.44	1.10	0.15		
32:3 DAG	0.98	0.77	1.11	0.15	1.40	0.21	0.84	0.18	1.08	0.44		
30:0 DAG	0.96	0.34	1.16	0.02	1.11	0.37	1.16	0.01	1.09	0.11		
30:1 DAG	0.97	0.35	1.15	0.01	0.98	0.59	1.00	0.98	1.05	0.15		
30:2 DAG	1.07	0.42	1.14	0.02	1.16	0.35	1.05	0.72	1.05	0.54		
30:3 DAG	0.97	0.71	0.93	0.49	1.19	0.19	0.78	0.25	1.34	0.15		
28:0 DAG	1.00	0.95	1.18	0.04	1.05	0.53	1.06	0.10	1.14	0.00		
28:1 DAG	0.99	0.83	1.11	0.34	1.17	0.08	0.96	0.38	1.21	0.21		

Figure 13: Fold changes and p-values for the response of 29 different DAG species to 250 nM UDP vs basal. Cells highlighted in pink show a fold increase with p-value < 0.01, and cells highlighted in red show a fold increase with p-value < 0.001.

25μM UDP vs basal												
	fold change		p-value		fold change		p-value		fold change		p-value	
	0.5min	0.5min	2min	2min	3min	3min	15min	15min	30min	30min		
38:0 DAG	1.01	0.92	1.10	0.24	0.81	0.10	1.12	0.14	1.20	0.11		
38:1 DAG	0.93	0.03	0.97	0.32	0.96	0.33	1.05	0.11	0.98	0.69		
38:2 DAG	0.98	0.56	1.07	0.10	1.05	0.29	1.11	0.01	1.05	0.29		
38:3 DAG	1.01	0.80	1.16	0.04	1.15	0.17	2.16	0.00	1.60	0.00		
38:4 DAG	1.04	0.51	1.27	0.00	1.56	0.00	1.97	0.00	1.53	0.00		
38:5 DAG	1.00	0.99	1.31	0.00	1.57	0.00	1.75	0.00	1.45	0.00		
38:6 DAG	1.00	0.97	1.17	0.04	1.10	0.35	1.26	0.00	1.33	0.05		
36:0 DAG	0.95	0.40	1.07	0.32	0.88	0.19	1.00	0.97	1.04	0.64		
36:1 DAG	1.02	0.64	1.13	0.03	1.02	0.54	1.27	0.00	1.24	0.00		
36:2 DAG	1.02	0.71	1.12	0.08	1.15	0.00	1.49	0.00	1.32	0.00		
36:3 DAG	1.06	0.32	1.15	0.15	1.24	0.00	1.47	0.00	1.42	0.00		
36:4 DAG	1.07	0.17	1.22	0.02	1.44	0.00	1.61	0.00	1.49	0.00		
36:5 DAG	1.06	0.22	1.17	0.05	1.25	0.00	1.34	0.02	1.28	0.00		
34:0 DAG	0.97	0.55	1.07	0.28	0.91	0.11	1.05	0.39	0.96	0.41		
34:1 DAG	1.02	0.72	1.11	0.09	1.04	0.37	1.29	0.00	1.18	0.00		
34:2 DAG	1.05	0.32	1.11	0.14	1.09	0.03	1.32	0.00	1.26	0.00		
34:3 DAG	1.05	0.32	1.15	0.15	1.20	0.00	1.18	0.01	1.35	0.00		
34:4 DAG	1.08	0.09	1.15	0.12	0.85	0.65	1.15	0.22	2.43	0.25		
34:1 DAGe/p	1.00	0.99	1.06	0.36	1.00	0.99	1.12	0.05	1.19	0.01		
32:0 DAG	0.98	0.66	1.06	0.32	0.95	0.34	1.23	0.01	1.11	0.04		
32:1 DAG	1.03	0.56	1.10	0.09	1.02	0.71	1.25	0.00	1.18	0.00		
32:2 DAG	1.06	0.35	1.17	0.07	1.00	0.95	1.03	0.80	1.24	0.02		
32:3 DAG	1.03	0.53	1.16	0.13	1.01	0.93	0.81	0.08	1.20	0.18		
30:0 DAG	1.02	0.72	1.20	0.07	0.96	0.51	1.14	0.02	1.13	0.12		
30:1 DAG	0.96	0.39	1.06	0.23	0.97	0.53	1.07	0.15	1.05	0.23		
30:2 DAG	1.02	0.77	1.20	0.08	0.95	0.60	0.89	0.43	1.14	0.18		
30:3 DAG	1.04	0.48	0.99	0.83	1.00	0.99	0.88	0.61	1.62	0.25		
28:0 DAG	1.02	0.56	1.13	0.05	1.00	0.97	1.08	0.36	1.11	0.02		
28:1 DAG	1.04	0.33	1.07	0.31	1.07	0.40	1.03	0.70	1.36	0.20		

Figure 14: Fold changes and p-values for the response of 29 different DAG species to 250 μM UDP vs basal. Cells highlighted in pink show a fold increase with p-value < 0.01, and cells highlighted in red show a fold increase with p-value < 0.001.

timeframe for PIP₂ hydrolysis. If these are the only two (or the major two) pathways for PA production upon stimulation with UDP in the RAW 264.7 cells, since we do not see PLD activity in the RAW 264.7 cells upon stimulation by UDP, inhibition of DAGk would presumably decrease the DAG response of all DAGs coming from PA production.

For these experiments, cells were pretreated with either 0.05% DMSO or 10 μ M R59949 (in DMSO) for 1 hour, and were stimulated with 25 μ M UDP for 30s, 3min, 15min, and 30min, each in triplicate. The graphs of some of the DAG species showing responses representative of a certain population of DAGs are shown in Figure 15. The graphs on the left show total ng DAG produced for the following: UDP over basal (in green squares), UDP + R59949 over basal (in red triangles), and R59949 over basal (in cyan x's). Each graph on the right represents the total change in DAG levels over baseline for one of two conditions: UDP stimulation without inhibitor compared to basal without inhibitor (shown in green) and UDP stimulation with R59949 compared to basal with R59949 (shown in red).

For many of the DAG species, the DAGk inhibitor R59949, lowered the basal levels of DAG at all time points. The differences between basal levels and R59949 levels of DAG are shown in Figure 16. Due to the decrease in basal DAGs with R59949, DAGk appears to play an important role in the level of resting DAGs in the RAW 264.7 cell.

Figure 17 includes the differences between DAG produced from UDP alone (over basal) and DAG produced from UDP with R59949 (over DAG levels with R59949 alone). The cells in Figure 17 are highlighted according to the following conditions: pink shows an increase over baseline with p-value less than 0.05; red shows an increase over baseline with p-value less than 0.01; light blue shows a decrease over baseline with pvalue less than 0.05; and dark blue shows a decrease over baseline with p-value less than 0.01.

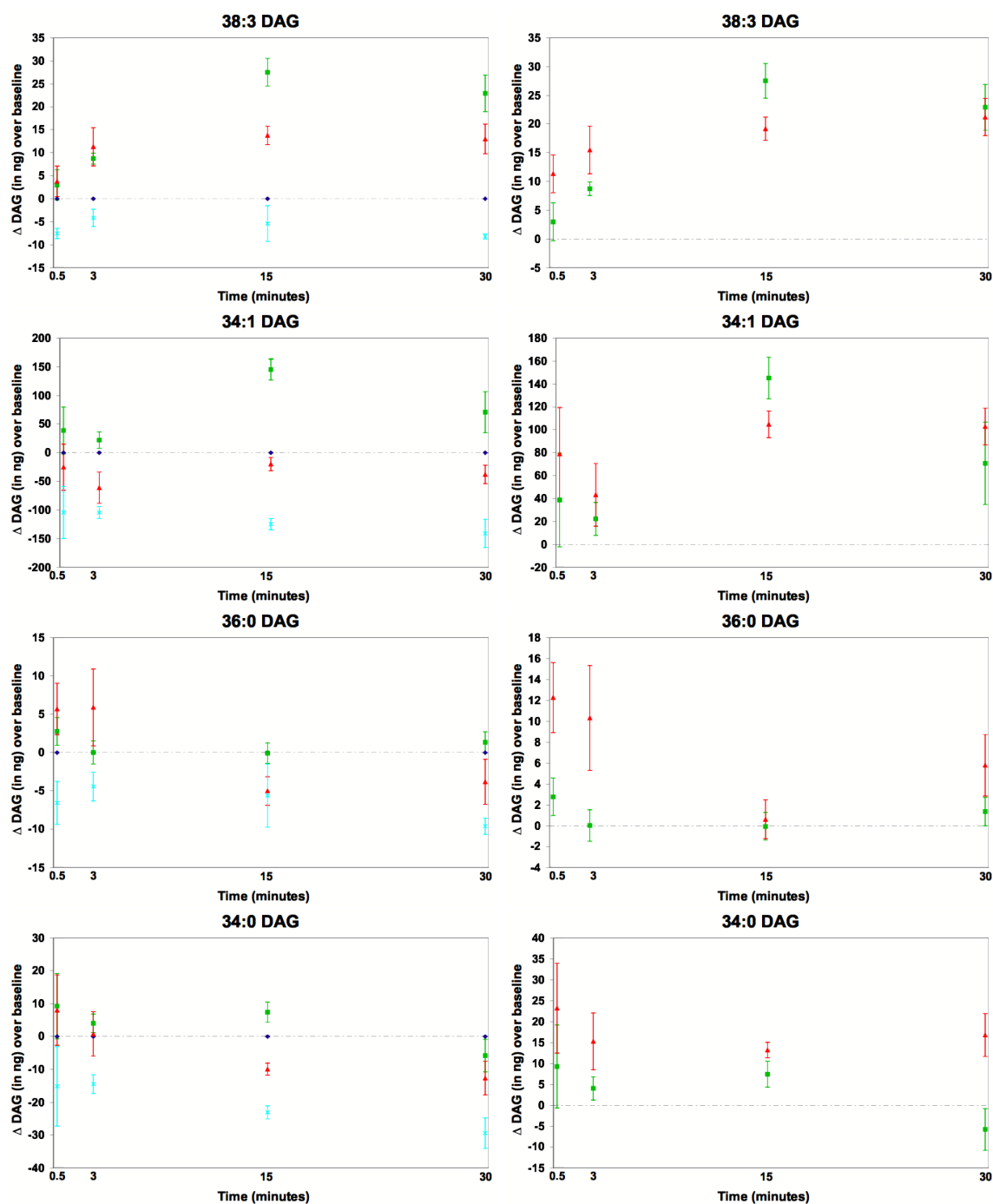


Figure 15: Results from stimulation of RAW 264.7 cells \pm 25 μ M UDP and \pm 10 μ M R59949. Graphs on the left show total ng DAG produced for the following: UDP over basal (green squares), UDP + R59949 over basal (red triangles), and R59949 over basal (cyan squares). Graphs on the right represent the total change in DAG levels over baseline for one of two conditions: UDP stimulation without inhibitor compared to basal without inhibitor (green squares) and UDP stimulation with 10 μ M R59949 compared to basal with 10 μ M R59949 (red triangles).

		Basal vs R59949							
		difference	p-value	difference	p-value	difference	p-value	difference	p-value
		0.5min	0.5min	3min	3min	15min	15min	30min	30min
38:0 DAG		-5.60	0.03	-4.02	0.30	-4.59	0.28	-8.33	0.00
38:1 DAG		-11.56	0.05	-8.74	0.24	-16.23	0.02	-13.74	0.04
38:2 DAG		-12.41	0.02	-5.50	0.09	-8.68	0.13	-14.27	0.03
38:3 DAG		-8.71	0.00	-4.09	0.22	-5.39	0.09	-8.21	0.01
38:4 DAG		-8.37	0.00	-4.97	0.29	-4.70	0.13	-6.13	0.08
38:5 DAG		-4.55	0.01	-3.32	0.14	-4.45	0.02	-3.78	0.00
38:6 DAG		-2.38	0.05	-2.49	0.22	-3.06	0.07	-4.12	0.00
36:0 DAG		-4.55	0.19	-4.04	0.18	-5.62	0.15	-9.61	0.00
36:1 DAG		-43.06	0.04	-23.99	0.04	-23.81	0.25	-39.84	0.05
36:2 DAG		-59.60	0.00	-43.49	0.00	-50.57	0.00	-51.57	0.00
36:3 DAG		-9.98	0.00	-7.34	0.13	-8.36	0.00	-9.06	0.00
36:4 DAG		-4.16	0.00	-2.57	0.17	-3.51	0.01	-3.34	0.00
36:5 DAG		-0.96	0.01	-0.54	0.60	-1.27	0.20	-1.88	0.01
34:0 DAG		-26.24	0.08	-12.81	0.19	-23.11	0.10	-29.43	0.09
34:1 DAG		-153.32	0.02	-101.87	0.00	-124.74	0.03	-140.86	0.03
34:2 DAG		-33.89	0.00	-25.31	0.00	-31.08	0.00	-31.05	0.00
34:3 DAG		-1.82	0.60	-3.45	0.41	-7.95	0.04	-9.08	0.00
34:4 DAG		-1.85	0.15	0.20	0.90	-0.24	0.90	-1.31	0.09
34:1 DAGe/p		-65.87	0.13	-48.39	0.01	-32.04	0.32	-84.56	0.08
32:0 DAG		-38.13	0.10	-20.24	0.17	-28.78	0.18	-36.95	0.14
32:1 DAG		-43.29	0.00	-30.52	0.00	-35.56	0.00	-42.00	0.01
32:2 DAG		-5.29	0.02	-3.76	0.11	-1.47	0.72	-5.59	0.00
32:3 DAG		0.58	0.54	1.79	0.30	-0.72	0.63	0.40	0.65
30:0 DAG		-10.69	0.18	-7.62	0.08	-3.49	0.72	-13.22	0.04
30:1 DAG		-4.60	0.15	0.61	0.78	-0.12	0.97	-4.11	0.26
30:2 DAG		-0.44	0.72	0.98	0.33	1.40	0.42	-0.74	0.29
30:3 DAG		-1.65	0.21	0.74	0.54	-0.27	0.83	-0.63	0.50
28:0 DAG		0.48	0.35	4.63	0.03	1.38	0.39	0.76	0.64
28:1 DAG		1.93	0.65	2.55	0.51	-0.09	0.98	0.77	0.62

Figure 16: DAG levels (in ng) and corresponding p-values for differences between cells pretreated with and without 10 μ M R59949 throughout the tested timecourse. Cells highlighted in light blue show a decrease with p-value < 0.05, and cells highlighted in dark blue show a decrease with p-value < 0.01. Cells highlighted in pink show an increase with p-value < 0.05.

This figure includes two panels. The left panel shows the fold changes and p-values for UDP stimulation versus basal levels. Species are grouped according to their response to 25 μ M UDP. There were three basic trends observed from these data: 1) species did not produce a significant change from baseline levels throughout the tested timecourse, 2) species remained near baseline initially and then by 3 minutes were increasing over baseline levels and continued to increase until 15 minutes, where the response peaked and therefore levels dropped slightly by 30 minutes but were still significantly above baseline, and 3) species responded similarly as in case two, except the initial response was a significant decrease over baseline levels. Most of the

Fold changes and p-values for UDP vs basal										Difference of UDP+R59949 over R59949 vs UDP over basal (in ng)									
fold	p-value	fold	p-value	fold	p-value	fold	p-value	fold	p-value	fold	p-value	fold	p-value	fold	p-value	fold	p-value	fold	p-value
0.5min	0.5min	3min	3min	15min	15min	30min	30min	0.5min	0.5min	3min	3min	15min	15min	30min	30min	0.5min	0.5min	3min	3min
38:0 DAG	1.10	1.2E-01	1.00	9.6E-01	1.03	5.5E-01	1.09	8.9E-02	38:0 DAG	4.51	2.7E-01	4.93	2.1E-01	1.76	2.5E-01	1.03	4.6E-01		
38:6 DAG	0.98	7.0E-01	1.02	7.9E-01	1.04	5.0E-01	1.06	2.2E-01	38:6 DAG	1.83	1.1E-01	3.44	1.7E-01	3.02	1.2E-03	1.75	1.0E-01		
36:0 DAG	0.97	6.8E-01	1.00	9.9E-01	0.98	6.8E-01	1.02	6.1E-01	36:0 DAG	5.50	2.0E-01	6.36	1.9E-01	4.32	4.7E-02	4.42	4.6E-02		
34:3 DAG	1.02	7.0E-01	1.03	4.8E-01	0.97	6.5E-01	1.06	2.8E-01	34:3 DAG	1.45	4.2E-01	4.22	3.7E-01	9.90	1.2E-02	1.38	4.8E-01		
34:4 DAG	0.96	4.9E-01	1.09	1.9E-01	0.96	5.5E-01	0.94	3.8E-01	34:4 DAG	2.92	5.4E-02	2.01	3.5E-01	3.44	1.9E-01	2.33	1.0E-01		
32:3 DAG	1.05	3.6E-01	1.13	2.1E-01	0.97	5.5E-01	0.89	1.5E-01	32:3 DAG	0.93	4.5E-01	3.21	4.3E-01	4.64	4.3E-03	2.03	1.5E-01		
30:2 DAG	1.02	7.7E-01	1.06	6.2E-01	1.01	8.9E-01	0.92	1.8E-01	30:2 DAG	1.94	2.4E-01	2.22	4.4E-01	0.93	4.1E-01	1.91	1.1E-01		
30:3 DAG	0.94	4.3E-01	0.98	8.7E-01	0.94	4.7E-01	0.87	6.5E-02	30:3 DAG	1.88	5.4E-02	0.73	6.7E-01	0.92	3.9E-01	1.14	2.6E-01		
28:1 DAG	1.00	1.0E+00	1.07	2.9E-01	0.91	2.0E-01	0.89	1.5E-01	28:1 DAG	1.74	3.1E-01	10.26	2.2E-01	12.68	2.9E-03	5.88	7.2E-02		
38:1 DAG	0.94	1.6E-02	0.98	7.0E-01	0.99	9.1E-01	1.03	6.1E-01	38:1 DAG	12.41	1.1E-01	25.30	1.0E-01	22.80	1.0E-03	14.27	3.0E-03		
34:0 DAG	0.89	4.1E-03	1.04	3.2E-01	1.08	1.1E-01	0.97	5.7E-01	34:0 DAG	26.46	9.8E-03	10.26	2.3E-01	15.96	9.2E-05	20.69	9.7E-03		
38:3 DAG	0.95	3.2E-01	1.26	7.9E-06	1.69	3.4E-09	1.58	4.1E-04	38:3 DAG	9.42	4.5E-03	3.39	3.4E-01	-6.40	3.4E-01	3.80	4.2E-01		
38:4 DAG	0.95	3.0E-01	1.44	1.5E-05	1.72	4.7E-08	1.48	1.0E-03	38:4 DAG	7.67	3.4E-03	3.20	2.8E-01	-7.49	4.1E-01	1.61	6.9E-01		
38:5 DAG	0.93	9.0E-02	1.31	1.4E-07	1.42	1.1E-06	1.33	7.7E-03	38:5 DAG	3.02	1.5E-02	2.10	3.9E-01	0.75	6.2E-01	0.37	7.1E-01		
36:3 DAG	0.97	5.8E-01	1.21	9.0E-06	1.48	2.9E-09	1.40	2.0E-03	36:3 DAG	7.48	2.8E-03	1.32	5.6E-01	-5.45	2.5E-01	2.67	5.4E-01		
36:4 DAG	0.93	1.0E-01	1.29	2.6E-06	1.43	7.8E-08	1.34	7.1E-03	36:4 DAG	3.37	1.9E-03	1.94	1.4E-01	-0.88	4.9E-01	1.55	1.2E-01		
36:2 DAG	0.91	4.4E-02	1.11	2.4E-02	1.50	2.1E-07	1.38	9.1E-03	36:2 DAG	40.91	1.5E-03	11.41	3.2E-01	-4.23	7.9E-01	19.40	2.7E-01		
34:2 DAG	0.92	5.2E-02	1.13	9.4E-03	1.44	1.0E-07	1.32	9.6E-03	34:2 DAG	25.12	2.6E-04	3.77	5.1E-01	-8.35	4.1E-01	8.16	2.6E-01		
36:1 DAG	0.89	9.3E-03	1.06	1.9E-01	1.29	1.2E-06	1.22	4.6E-02	36:1 DAG	44.45	9.1E-03	17.30	1.7E-01	2.25	8.2E-01	32.97	2.5E-02		
34:1 DAG	0.87	2.8E-03	1.05	3.0E-01	1.39	2.5E-07	1.26	3.9E-02	34:1 DAG	122.84	3.3E-03	22.54	4.8E-01	4.06	8.6E-01	64.35	8.9E-02		
32:1 DAG	0.90	8.5E-03	1.07	5.4E-02	1.33	1.2E-07	1.21	4.1E-02	32:1 DAG	36.58	1.5E-03	9.84	2.7E-01	4.12	5.9E-01	20.55	5.2E-02		
34:1 DAGe/p	0.86	1.2E-02	1.00	9.4E-01	1.14	1.0E-02	1.32	2.5E-02	34:1 DAGe/p	43.96	1.5E-02	8.76	5.7E-01	14.31	3.1E-01	31.87	1.3E-01		
38:2 DAG	0.90	9.9E-03	1.06	6.3E-02	1.13	2.1E-03	1.14	7.5E-02	38:2 DAG	16.38	8.9E-03	8.61	2.2E-01	3.30	5.6E-01	9.71	1.2E-01		
32:0 DAG	0.88	2.7E-03	1.07	2.1E-01	1.26	8.6E-06	1.15	8.4E-02	32:0 DAG	36.31	8.4E-03	7.97	5.0E-01	12.78	1.9E-02	21.32	2.9E-02		
30:1 DAG	0.91	1.6E-02	1.08	5.0E-02	1.12	2.5E-04	1.04	4.5E-01	30:1 DAG	10.54	1.5E-02	7.18	2.9E-01	2.22	3.4E-01	7.02	4.6E-02		
36:5 DAG	1.00	9.9E-01	1.15	1.1E-02	1.13	3.8E-02	1.07	2.6E-01	36:5 DAG	0.86	1.7E-01	0.78	4.9E-01	0.48	3.6E-01	0.88	7.4E-02		
32:2 DAG	1.00	9.4E-01	1.02	8.3E-01	1.23	1.8E-06	1.13	8.5E-02	32:2 DAG	6.37	1.8E-01	6.15	5.3E-02	-2.82	4.2E-01	3.40	8.0E-02		
30:0 DAG	0.94	2.0E-01	1.01	8.4E-01	1.11	2.0E-03	1.07	3.5E-01	30:0 DAG	16.42	1.1E-01	13.04	3.6E-02	3.37	4.3E-01	12.39	1.4E-03		
28:0 DAG	0.90	1.1E-01	1.26	1.6E-02	1.02	8.1E-01	0.93	2.4E-01	28:0 DAG	2.82	1.4E-03	0.84	8.0E-01	0.70	6.4E-01	3.41	3.4E-02		

Figure 17: Comparison of UDP response to response with UDP and R59949. The left panel displays fold changes and p-values for UDP versus basal levels, and species are grouped according to the nature of their response. The right panel displays DAG levels (in ng) and corresponding p-values for differences between cells stimulated with UDP in the presence and absence of R59949. The species in this panel are aligned with the species from the left panel.

higher-carbon PUFA-containing DAGs fell into the second category, while most of the mono- and di-unsaturated DAGs fell into the third category. The saturated DAG species either gave no significant change or produced small changes at one or two of the four time points.

The right panel shows the total difference, in ng, between the amount of DAG produced with UDP + R59949 (over amount from cells pretreated with R59949) and the amount produced from UDP alone (over the amount from basal cells). The species are listed in the same order as the panel on the left in order to compare the effects of R59949 on the UDP response with the type of response each species exhibited from UDP alone. For the species in category 1, the inhibitor produced slightly higher levels of DAG, predominantly at the 15 minute time point. However, for the species in categories 2 and 3, the cells pretreated with R59949 produced a much higher level of DAG at 30 seconds than the cells with UDP alone (where for these species of DAG, levels either remained near baseline or dropped below baseline, which is a behavior we have seen previously but has not been very reproducible). This suggests a heavy dependence on DAGk activity in the UDP pathway for high-carbon PUFAs and mono- and di-unsaturated DAGs, especially at the early time points. If PIP₂ hydrolysis is the only other means of DAG production at early time points, the immediate increase in DAG levels from categories 2 and 3 observed in the presence of R59949 is a result of PIP₂ hydrolysis, and the reason we are not seeing this rise in DAGs without the inhibitor is a result of rapid phosphorylation of resting DAGs (in categories 2 and 3) via DAGk activity. For most of the species which gave robust increases at later time points, the overall shape of the curve with UDP + R59949 was also subdued slightly, where we did not observe as robust an increase from the 3 minute to 15 minute time point as we see with UDP alone, suggesting a combined role for DAGk and LPP at the later time points.

V.4 Multiple DAG Inhibitors Experiments

In order to further investigate the origin of both resting DAG and DAG produced post UDP stimulation in the RAW 264.7 cells, we tested several different pharmacological inhibitors and their affect on the UDP response at 15 minutes, the time point where we see most DAG production in most DAG species. The inhibitors included in this study and the concentrations used are as follows: 10 μM U73122 (inhibits PI-PLC activity), 10 μM U73433 (inactive analog of U73122), 150 μM Propranolol (inhibits conversion of PA to DAG via LPP), 10 μM R59949 (DAGk inhibitor II), and 50 μM Thimerosal (inhibits conversion of MAG to DAG via MGAT). Figures 18 - 22 show the results from three experimental repeats, each with three replicates.

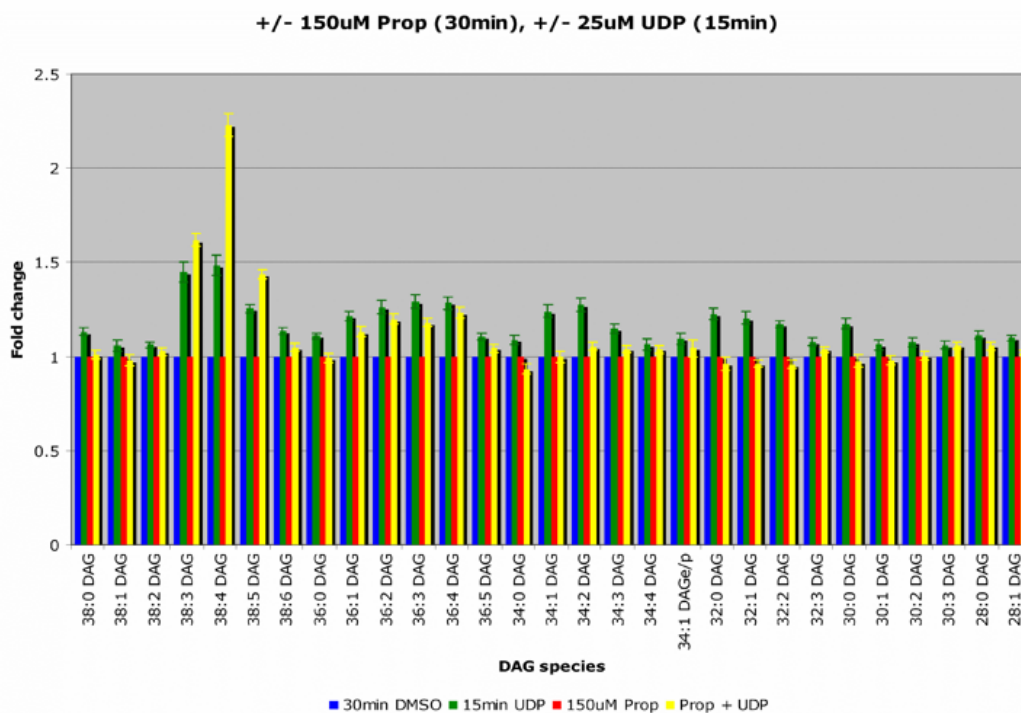


Figure 18: Fold changes of DAG in response to a 15 minute stimulation of 25 μM UDP +/- 30min pretreatment with 150 μM Propranolol.

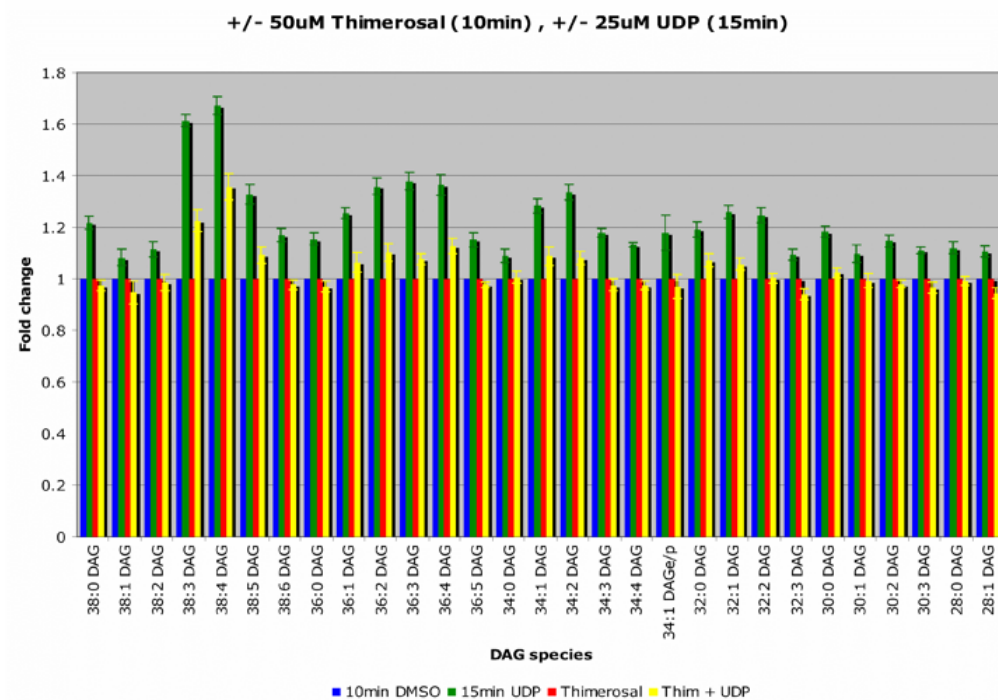


Figure 19: Fold changes of DAG in response to a 15 minute stimulation of 25 μM UDP +/- 10min pretreatment with 50 μM Thimerosal.

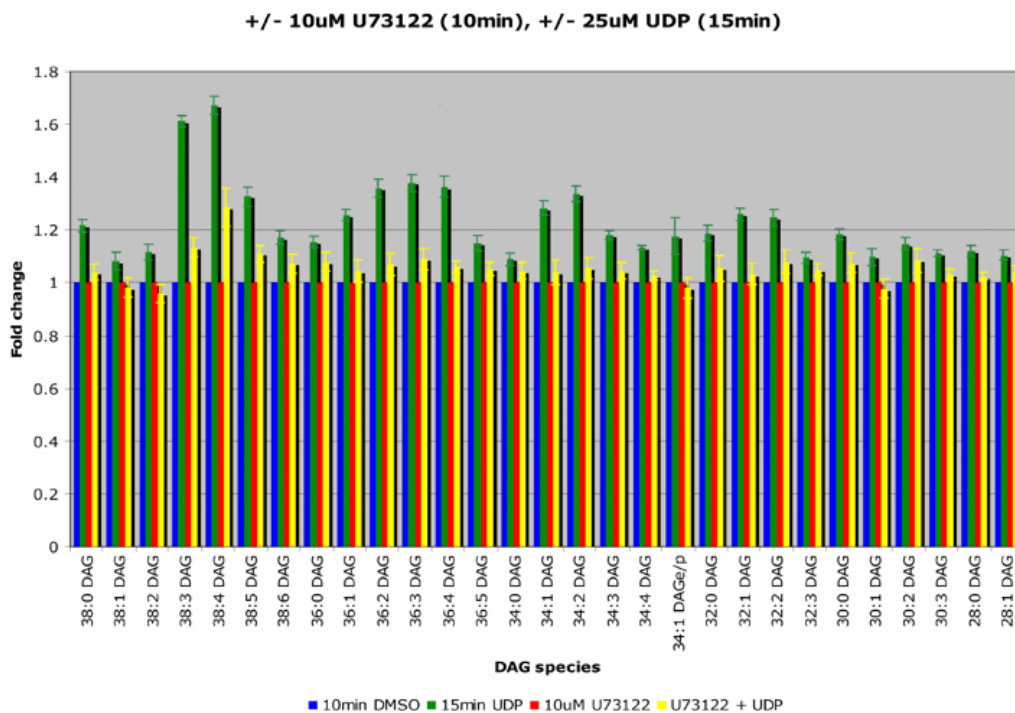


Figure 20: Fold changes of DAG in response to a 15 minute stimulation of 25 μM UDP +/- 10min pretreatment with 10 μM U73122.

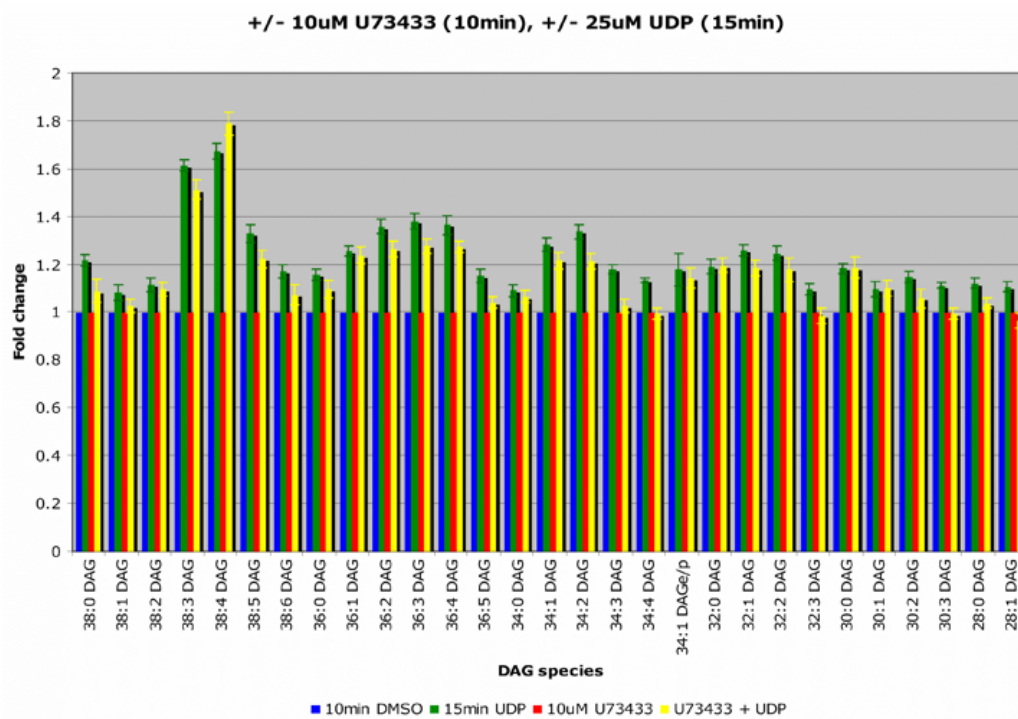


Figure 21: Fold changes of DAG in response to a 15 minute stimulation of 25 μM UDP +/- 10min pretreatment with 10 μM U73433.

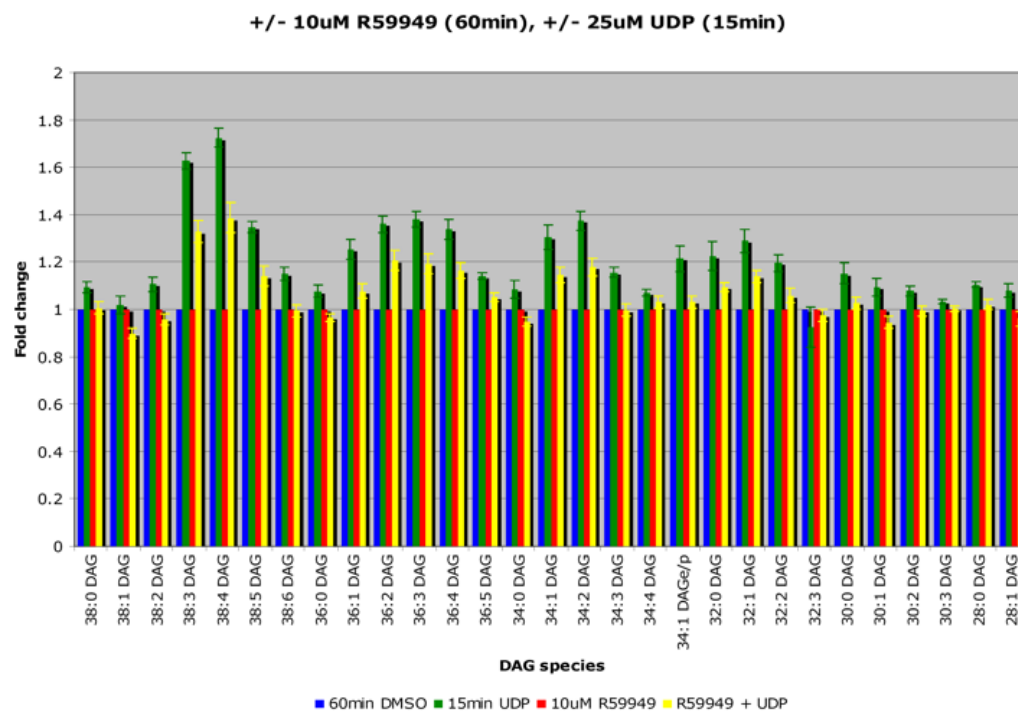


Figure 22: Fold changes of DAG in response to a 15 minute stimulation of 25 μM UDP +/- 60min pretreatment with 10 μM R59949.

Propranolol is perhaps the most interesting as far as differential effects are concerned, as it is enhancing UDPs ability to produce 38:3, 38:4, and 38:5 DAGs, slightly inhibiting the UDP response for the 36 carbon-containing DAG series, and is almost eliminating the UDP response in the lower carbon chain DAGs. Thimerosal and U73122 appear to have a similar effect as they are significantly inhibiting the UDP response across the board. Aside from a few obscure DAGs, U73433 does not have a significant effect on the UDP response, which is what one would hope to see, as U73433 is the inactive analog of U73122. Finally, R59949 gives the same effect as we had seen before with the timecourse experiments, where the response at 15 minutes is slightly inhibited for most DAGs. Although the results of these multiple inhibitor experiments do not seem to point to one source of DAG production, this does reemphasize the complexity of this signaling pathway and the need for further study.

V.5 Propranolol Experiments

Next we tested a timecourse of the DAG response to 25 μM UDP with and without pretreatment of 150 μM Propranolol, since out of all the tested inhibitors it was providing us with the most interesting differential responses. These data include four experiments performed in triplicate. Cells were pretreated with either 0.05% DMSO or 150 μM Propranolol (in DMSO) for 1 hour, and were stimulated with 25 μM UDP for 30s, 3min, 15min, and 30min, each in triplicate. The graphs of four of the DAG species showing responses representative of a certain population of DAGs are shown in Figure 23. As in the R59949 experiments, the graphs on the left show total ng DAG produced for the following: UDP over basal (in green squares), UDP + Propranolol over basal (in red triangles), and Propranolol over basal (in cyan x's). Each graph on the right represents the total change in DAG levels over baseline for one of two conditions: UDP stimulation without inhibitor compared to basal without inhibitor (shown in green) and UDP stimulation with Propranolol compared to basal with Propranolol (shown in red).

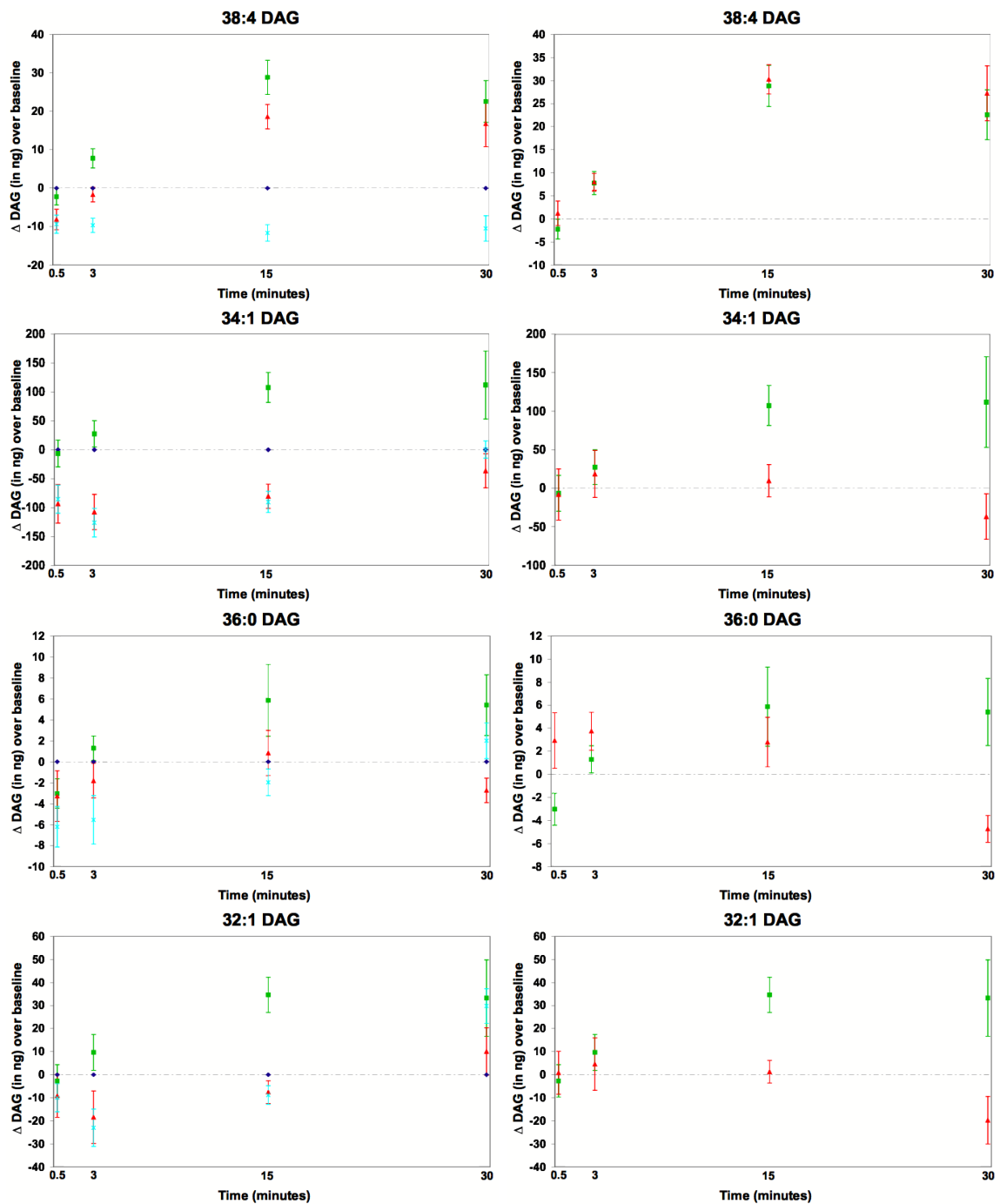


Figure 23: Results from stimulation of RAW 264.7 cells +/- 25 μM UDP and +/- 150 μM Propranolol. Graphs on the left show total ng DAG produced for the following: UDP over basal (in green squares), UDP + Propranolol over basal (in red triangles), and Propranolol over basal (in cyan x's). Graphs on the right represent the total change in DAG levels over baseline for one of two conditions: UDP stimulation without inhibitor compared to basal without inhibitor (shown in green squares) and UDP stimulation with 150 μM Propranolol compared to basal with 150 μM Propranolol (shown in red triangles).

Propranolol had little or no effect on the PUFA-containing DAG response to UDP throughout the tested timecourse, with the least effect on 38:4 DAG. We make note that this result is slightly different than what we saw in the multiple inhibitor experiment, where 38:4 DAG levels with Propranolol + UDP were significantly higher than with UDP alone. In most other species, Propranolol greatly reduced or even completely eliminated the DAG response to UDP throughout the tested timecourse. One trend that appeared in a few species was a decrease in DAG levels over baseline with Propranolol at the 30 minute time point. For these species, we also observed an increase in the Propranolol only (no UDP) samples (see the left graphs, cyan data points for 34:1 DAG, 36:0 DAG and 32:1 DAG). This data suggests that 38:4 DAG and, to a lesser extent, most PUFA-containing DAGs are not coming from PA via LPP. For most other DAGs, however, under the assumption that Propranolol is only inhibiting LPP and not activation other enzymes, one could propose that these DAGs are directly or indirectly coming from LPP activity.

To compliment our studies of the Propranolol effect on the DAG response, we also completed a set of three experiments testing the effects of Propranolol on the UDP response of PA over the same timecourse as above. Each experimental condition was performed in triplicate. The ratiomic analysis of these experiments is shown in Figure 24. Each cell in this figure displays the number of times a certain condition was seen to be significantly above or below the basal condition (or, in some cases, a specific condition noted in the figure). For example, in the 0.5 minute time block, a number of 3 for 34:1 DAG in the first column reveals that in all three experimental repeats, the triplicate average of DAG levels in the cells pretreated with propranolol was shown to be significantly increasing over the triplicate average for basal cells (no propranolol).

The results were in direct agreement with the two-pool DAG model. Propranolol had little effect on the PUFA-containing PAs, but had a profound effect on the mono- and di-unsaturated and saturated PAs. For this latter group of PAs, Propranolol

25uM UDP +/- 150uM Propranolol		0.5 min					3 min				
		vs Ctrl (0.5)			vs U	vs P	vs Ctrl (3)			vs U	vs P
	m/z	P	U	U+P	U+P	U+P	P	U	U+P	U+P	U+P
30:1PA, 20:5LPI, 36:3E	617.5	0	0	0	0	0	0	0	0	0	0
20:4LPI, 30:0PA, 36:2E	619.4	2	-1	2	3	0	2	1	2	3	0
32:3 PA	641.5	-2	-2	-1	0	0	-1	0	0	0	1
32:2 PA	643.5	-1	-1	0	0	0	0	0	1	0	0
32:1PA, 22:5LPI	645.5	3	0	3	3	0	3	1	3	3	1
32:0PA, 22:4LPI, 38:2E	647.4	3	1	3	2	0	3	0	3	2	0
34:2PA	671.5	2	0	3	3	0	2	1	2	2	0
34:1PA	673.5	3	1	3	3	0	3	1	3	3	0
34:0PA	675.5	3	0	2	2	0	3	2	3	2	-1
36:4PA	695.5	0	0	0	0	0	1	2	1	0	1
36:3PA	697.5	0	0	0	-1	0	1	2	3	0	1
36:2PA	699.6	2	2	2	0	0	2	2	2	1	1
36:1PA	701.5	2	1	2	1	0	2	1	2	0	0
36:0 PA	703.5	0	0	0	1	0	0	1	1	0	0
32:1PG, 38:6 PA	719.4	1	0	1	1	0	3	1	3	3	0
32:0PG, 38:5 PA	721.5	1	0	2	1	0	3	1	3	2	0
38:4PA	723.5	0	0	0	0	0	2	2	2	0	0
38:3PA	725.5	0	0	0	0	0	0	1	1	0	1
38:2PA	727.5	0	-1	0	0	0	0	0	1	0	1

		15 min					30 min				
		vs Ctrl (15)			vs U	vs P	vs Ctrl (30)			vs U	vs P
	m/z	P	U	U+P	U+P	U+P	P	U	U+P	U+P	U+P
30:1PA, 20:5LPI, 36:3E	617.5	0	0	0	0	0	-1	-1	-1	0	0
20:4LPI, 30:0PA, 36:2E	619.4	3	0	3	3	0	3	0	3	3	0
32:3 PA	641.5	0	0	0	-1	0	-2	-1	-3	-2	0
32:2 PA	643.5	0	0	0	0	0	-1	-1	-1	0	0
32:1PA, 22:5LPI	645.5	3	0	3	3	0	3	0	3	3	0
32:0PA, 22:4LPI, 38:2E	647.4	3	0	3	3	1	3	0	3	3	0
34:2PA	671.5	1	0	3	2	1	2	0	2	2	0
34:1PA	673.5	3	0	3	3	1	3	0	3	3	0
34:0PA	675.5	3	0	3	3	0	3	0	3	3	0
36:4PA	695.5	0	2	3	0	3	0	0	1	1	0
36:3PA	697.5	0	1	2	0	2	0	0	1	1	2
36:2PA	699.6	1	1	3	1	2	1	1	2	0	2
36:1PA	701.5	0	0	2	1	1	3	1	2	0	0
36:0 PA	703.5	0	0	0	0	0	1	2	1	0	0
32:1PG, 38:6 PA	719.4	1	0	3	3	1	2	-1	1	2	-1
32:0PG, 38:5 PA	721.5	2	1	3	3	3	3	-1	2	3	0
38:4PA	723.5	1	3	3	1	3	2	2	2	2	2
38:3PA	725.5	0	3	2	0	2	1	2	2	0	3
38:2PA	727.5	0	1	1	2	2	0	1	1	0	1

Figure 24: Lipid array for PA response to 25 μ M UDP +/- 150 μ M Propranolol at 30s, 3min, 15min, and 30min. Cells highlighted in red (blue) show a significant increase (decrease) in that PA species for a particular condition in all three data sets. The first column lists the PA species along with any other species sharing the same m/z (mass to charge) ratio. The second column lists the m/z values. The first three columns of each time point block represent Propranolol, UDP, and UDP + Propranolol, respectively, each vs control. The fourth column in the block represents UDP + Propranolol vs UDP, and the fifth and final column represents UDP + Propranolol vs Propranolol.

caused a large increase in unstimulated cells, suggesting that these PAs were coming from mono- and di-unsaturated and saturated DAGs via a constitutively active DAGk. Since the DAG assays with Propranolol revealed that Propranolol completely eliminated the UDP response (for mono- and di-unsaturated and saturated DAGs), this suggests that Propranolol may be affecting part of the pathway of the two-pool DAG model, where PA generated from an intracellular pool of DAG is not allowed to participate in the resynthesis of PIP₂.

CHAPTER VI

QUANTIFICATION OF MOLECULAR SPECIES OF DIACYLGLYCEROL

VI.1 Introduction

In this chapter we discuss the method of DAG quantification used to collect all data on species-specific DAG changes in response to UDP. As stated in Chapter I, diacylglycerols are important cellular second messengers which play a significant role in initiating changes in cell behavior. DAGs differ from other well characterized second messengers (such as IP_3) as they are a heterologous population, with over 50 different species of DAG identified based on their varying acyl chain lengths and degrees of unsaturation. With evidence of differential roles for these species in cellular processes [14, 55], the need arises for a sensitive method for quantification of individual species of DAG in order to elucidate both the function and source of these second messengers in the complex background of several thousand cellular lipids.

Traditional methods for quantitative analysis of DAGs include radiolabeling assays where *E. coli* DAG kinase is used to convert DAG in neutral lipid fractions of various cell types to [^{32}P]-labeled phosphatidic acid [56, 57, 78]. Disadvantages of this method include the low resolution analytical techniques such as thin layer chromatography [14, 17] and the inability to identify acyl chain composition of DAGs. The identification of the molecular species of agonist-stimulated DAG production has also been studied using component fatty acid analysis [9, 22], as well as argentation (silver ion) chromatography [61]. Although both of these approaches provide interesting information, neither determines the exact molecular species that are present. To address the issue of detecting individual molecular species, capillary gas chromatography has also been used [54]. Unfortunately, all these strategies are time-consuming due to the process of derivatization via chemical reactions and involve larger amounts

of sample which makes them unsuitable for high throughput analyses. DAG is a key component of glycerophospholipid intermediate metabolism and serves as a cellular second messenger, hence a new analytical method was needed to achieve comprehensive molecular species analysis.

Mass spectrometry is the most sensitive and specific method for lipid analysis to date [48]. The combination of gas chromatography-negative ion chemical ionization mass spectrometry has been applied to a single species of DAG analysis from biological samples, but this method has a limitation in the number of detected molecular species and requires a multi-step derivatization prior to analysis [27]. As little as 30 fmol of 1-stearoyl-2-arachidonoyl-sn-3-glycerol can be analyzed in a sample.

New ionization techniques such as electrospray ionization mass spectrometry (ESI-MS) or matrix-assisted laser desorption/ionization (MALDI) enable the detection and identification of lipids with minimal fragmentation and direct data collection. With MALDI, which has been previously applied to the analysis of DAGs [3], the sample preparation is easy and fast and no derivatization is required. Despite its advantages, however, MALDI is more suitable for high molecular weight biomolecules (peptides and proteins). Due to their low molecular weight, lipids require special matrices and considerations such as compatibility between matrix and analyte to achieve high homogeneity between sample and matrix crystals; matrix ions are also detected and might interfere with the interpretation of the spectra.

Here we describe a method that overcomes some of these challenges and is based on soft ESI-MS. Introducing Na^+ to the sample results in the formation of charged Na^+ -DAG adducts rendering detection by ESI-MS possible. Separation of DAG species from the more polar phospholipids results in higher sensitivity which makes this method suitable for analysis of complex lipid mixtures and adaptable to medium- to high-throughput assays. A multiple linear regression model for the construction of calibration curves for specific DAG species based on their molecular characteristics is also shown. As a result, we offer the first method for the simultaneous detection and

quantification of up to 28 individual molecular species of DAG from the extract of a macrophage-derived cell.

VI.2 Experimental Materials and Methods

VI.2.1 Materials

The materials used in this method of DAG quantification are listed in Table VI.2.1 below. RAW 264.7 cells, which are a macrophage-like, Abelson leukemia virus-

Table 5: Materials used in the method of quantification of multiple species of DAG.

Material	Source
1,2-dilauroyl-sn-glycerol (24:0 DAG)	Avanti Polar Lipids (Alabaster, AL)
1,2-dimyristoyl-sn-glycerol (28:0 DAG)	Avanti Polar Lipids (Alabaster, AL)
1,2-dipalmitoyl-sn-glycerol (32:0 DAG)	Avanti Polar Lipids (Alabaster, AL)
1-octadecanoyl-2-hexadecanoyl-rac-glycerol (34:0 DAG)	Avanti Polar Lipids (Alabaster, AL)
1-palmitoyl-2-oleoyl-sn-glycerol (34:1 DAG)	Avanti Polar Lipids (Alabaster, AL)
1,2-dioctadecanoyl-rac-glycerol (36:0 DAG)	Avanti Polar Lipids (Alabaster, AL)
1,2-dioleoyl-sn-glycerol (36:2 DAG)	Avanti Polar Lipids (Alabaster, AL)
1-eicosanoyl-2-octadecanoyl-rac-glycerol (38:0 DAG)	Avanti Polar Lipids (Alabaster, AL)
1-stearoyl-2-arachidonoyl-sn-glycerol (38:4 DAG)	Avanti Polar Lipids (Alabaster, AL)
1-O-hexadecyl-2-acetoyl-sn-glycero-3-phosphocholine (C16 PAF)	Avanti Polar Lipids (Alabaster, AL)
Silica gel 60 (230-400 mesh)	EMD Chemicals Inc. (Gibbstown,NJ)
methanol (MeOH)	EMD Chemicals Inc. (Gibbstown,NJ)
chloroform (CHCl ₃)	EMD Chemicals Inc. (Gibbstown,NJ)
Sodium acetate	Sigma-Aldrich (St. Louis, MO)

transformed cell line derived from BALB/c mice, were obtained from the American Type Culture Collection (ATCC catalog number TIB-71, lot number 2263775), expanded, and stored in aliquots for use by the Alliance for Cellular Signaling (AfCS) laboratories (<http://www.signaling-gateway.org>). Stock vials of frozen AfCS cells were thawed and maintained in DMEM supplemented with 10% heat-inactivated fetal bovine serum, 20 mM HEPES, and 2 mM L-glutamine at 37°C in a humidified atmosphere with 5% CO₂. For routine maintenance in culture (passage), cells were seeded at a confluence of approximately 10% (1×10^6 and 3^6 cells on 100 and 150 mm plates, respectively) and grown to a confluence of approximately 50%.

VI.2.2 Extraction of glycerophospholipids from stimulated cells

Cells were seeded at 4×10^6 cells on 60 mm-diameter dishes and incubated for 24 hours in 10% serum. Before stimulation the medium was changed to DMEM supplemented with 20 mM HEPES, 2 mM L-glutamine, and 0.1 mg/mL BSA. Platelet-activating factor (PAF, dissolved in ethanol) was added to the medium at a final concentration of 100 nM, and cells were incubated at 37 °C for the indicated times. After treatment plates were placed on ice, medium was aspirated and cells were washed with 2 mL of ice-cold PBS, pelleted, and PBS aspirated. Phospholipids were extracted by a modified Bligh/Dyer procedure [5]. Ice-cold 1:1 0.1N HCl:CH₃OH (800 μL) was added to each cell pellet, and the suspensions were transferred to individual cold 12 × 75 mm borosilicate glass test tubes. 24:0 DAG (10 μL, 10 μg/mL) was added to all samples as an internal standard. After addition of 400 μL ice-cold CHCl₃ and thorough mixing, phospholipids were collected from the lower (organic) phase after layer separation by centrifugation.

VI.2.3 Diacylglycerol isolation and recovery

Diacylglycerol isolation from total phospholipids extracts was achieved by separation using silica gel column chromatography by means of an isocratic elution with 65:35:0.7 CHCl₃:CH₃OH:H₂O. Each sample was applied to a glass Pasteur pipette column plugged with glass wool and packed with a 6 cm bed of silica gel 60Å equilibrated with 10 mL of eluent. DAG molecular species were recovered in the first 3 mL of eluent, and solvents were evaporated in a vacuum centrifuge (Labconco Centrivap Concentrator, Kansas City, MO). Samples were dissolved in 105 μL of 9:1 CH₃OH:CHCl₃ containing 5 μL of 100 mM CH₃COONa and analyzed by mass spectrometry.

To evaluate the accuracy of the method and the recovery of DAG during extraction and separation procedures, cell extracts were spiked with known amount of 2 DAGs (200ng each of 36:0 and 36:2) and 100ng of the internal standard 24:0 DAG. For RAW 264.7 cell extracts the recovery was 98-103%. The basal level of total DAG (all

detected species) in RAW 264.7 cells was 1.69 ± 0.08 nmol/mg protein, calculated by using a conversion factor of 1.27 mg protein / 10^7 cells [62]. The reported abundance of DAG in other cell types was of similar value (1.47 ± 0.33 nmol/mg protein in SK-N-SH neuroblastoma cells [37] and about 1.5 nmol/mg protein in pheochromocytoma PC12 cells [2]).

VI.2.4 Mass spectrometric analysis of DAG extracts

Mass spectral analysis was performed on a Finnigan TSQ Quantum triple quadrupole mass spectrometer (ThermoFinnigan, San Jose, CA) equipped with a Harvard Apparatus syringe pump and an Ion Max electrospray ionization source. Samples were analyzed at an infusion rate of 10 μ L/min in positive ionization mode over the range of m/z 400 to 900. Since DAGs ionize poorly under normal electrospray conditions, Na^+ adducts were utilized to better detect the individual DAG species. Peaks corresponding to known DAG species were fragmented to confirm the identity of the species (Fig.25, A and B). Data were collected with the Xcalibur software package (ThermoFinnigan).

VI.3 Results and Discussion

VI.3.1 Isotopic correction

Figure 26 shows a typical spectrum of the DAG species isolated from a RAW 264.7 cell extract. The ESI-MS analysis provides peaks corresponding to the molecular ion of the sodiated adduct of each DAG. We recall here that the various species are distinguished by the total number of carbons in the acyl chains and their degree of unsaturation. Consequently, the DAGs are conveniently assigned a two-number system xx:y (i.e., 38:4 DAG) in which xx designates the total number of carbons in the acyl chains and y specifies the total number of double bonds.

The signals occur in clusters of peaks representing multiple species of DAGs having the same total number of carbons and different degrees of saturation separated by two

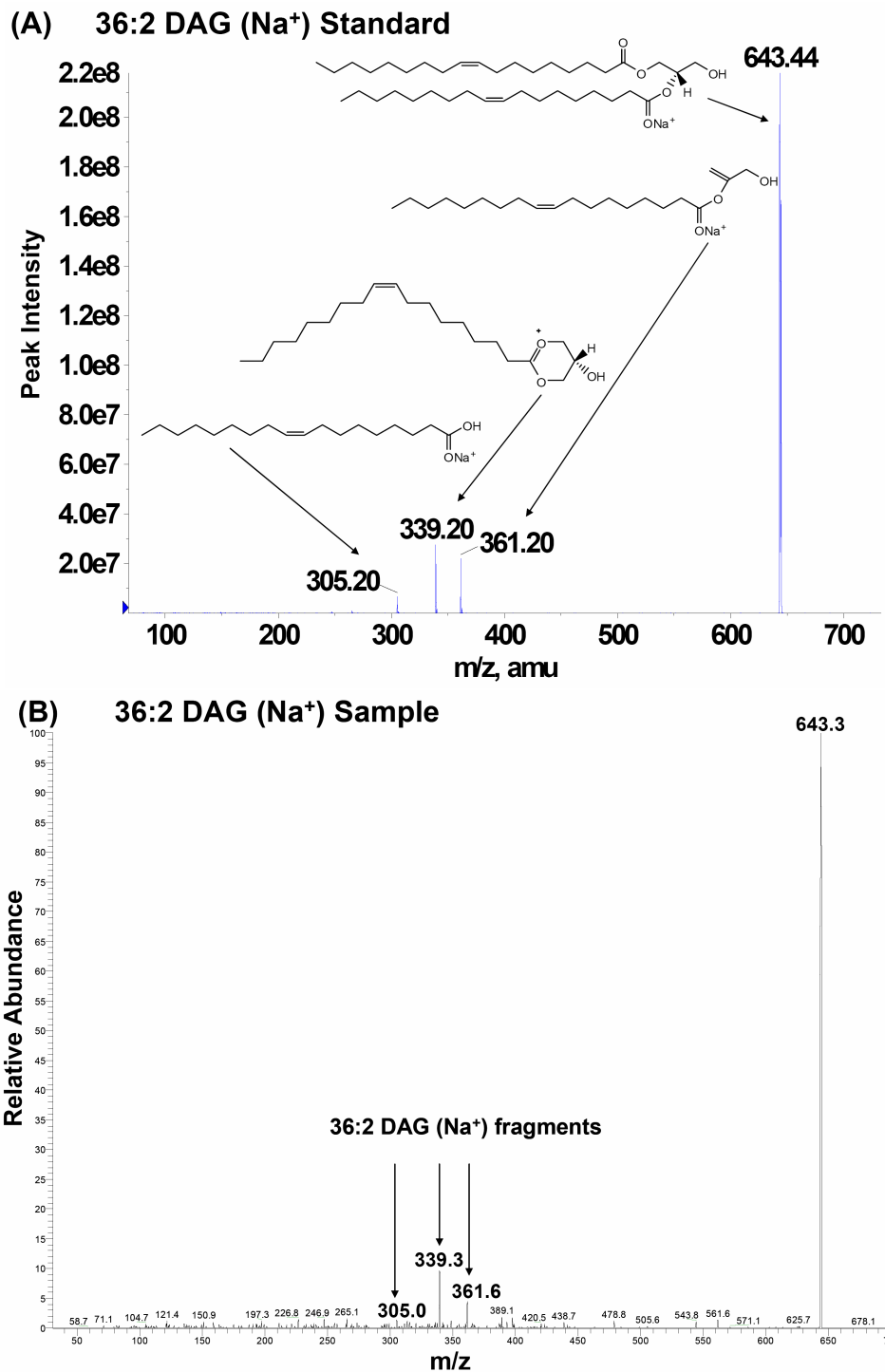


Figure 25: Identification of DAG sodium adducts. Identification of DAG lipid species was accomplished by MS/MS analysis of biological samples and synthetic standards when possible. As an example, the MS/MS fragmentation pattern for synthetic 36:2 DAG (A) compares favorably to that of naturally occurring 36:2 DAG (B).

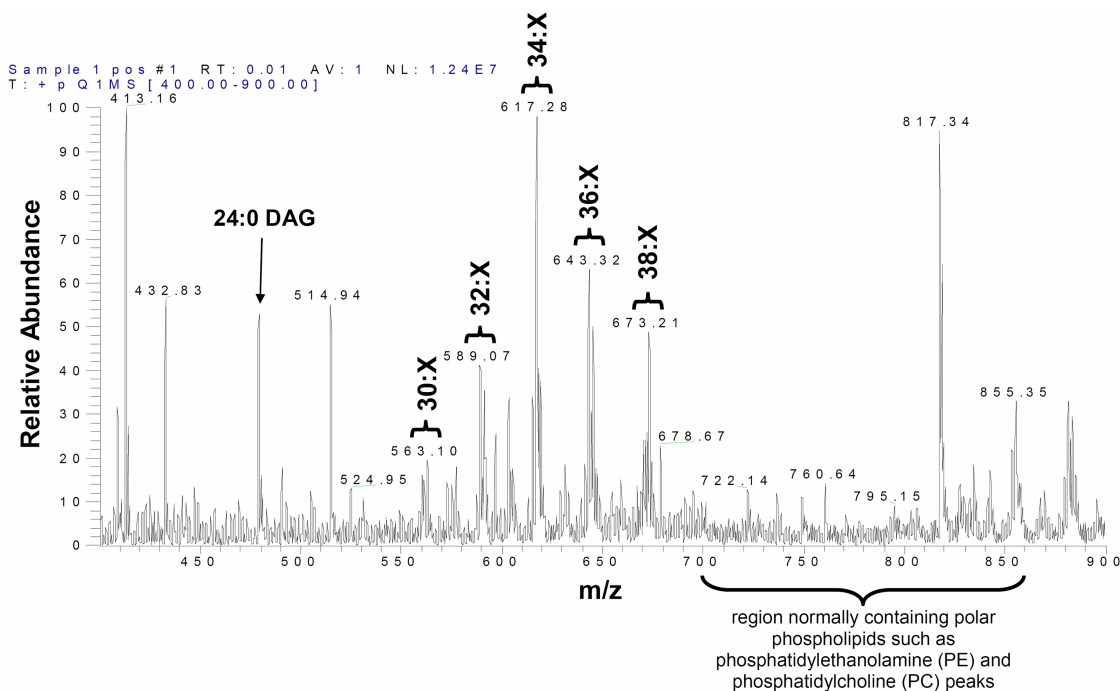


Figure 26: Positive ESI mass spectrum from a RAW 264.7 cell extract after chromatographic separation on a silica gel column to remove the polar phospholipids. The peaks for various DAG series appear in the center of the spectrum and the internal standard (24:0 DAG) is shown (m/z 479). The series numbers indicate the total number of carbons in the acyl chains on the DAG molecule. The PE and PC peaks, which usually dominate the spectrum in positive mode, have been functionally decreased as a result of chromatographic separation.

mass units. Spectra are complicated by the naturally occurring molecules containing known fractions of heavy isotopes, e.g. 1.10% ^{13}C and 0.2% ^{18}O (Fig. 27). Thus, each individual DAG produces two or more peaks for each of the molecular ions. One peak is at the exact molecular mass and the others are one or more mass units higher reflecting the natural abundance of ^{13}C , ^{18}O etc. In the case of DAG, contributions to the mass distribution are made from carbon, hydrogen and oxygen atoms. These multiple peaks lead to errors particularly for the peak that is two mass units higher, due to interference with the species that has one less double bond. To correct for this isotopic signal on neighboring peaks, the relative distribution of mass for each DAG molecule is computed. For example, 38:4 DAG has the formula $\text{C}_{41}\text{H}_{72}\text{O}_5$ which produces the distribution of mass for 38:4 DAG displayed in Table 6. Data in Table

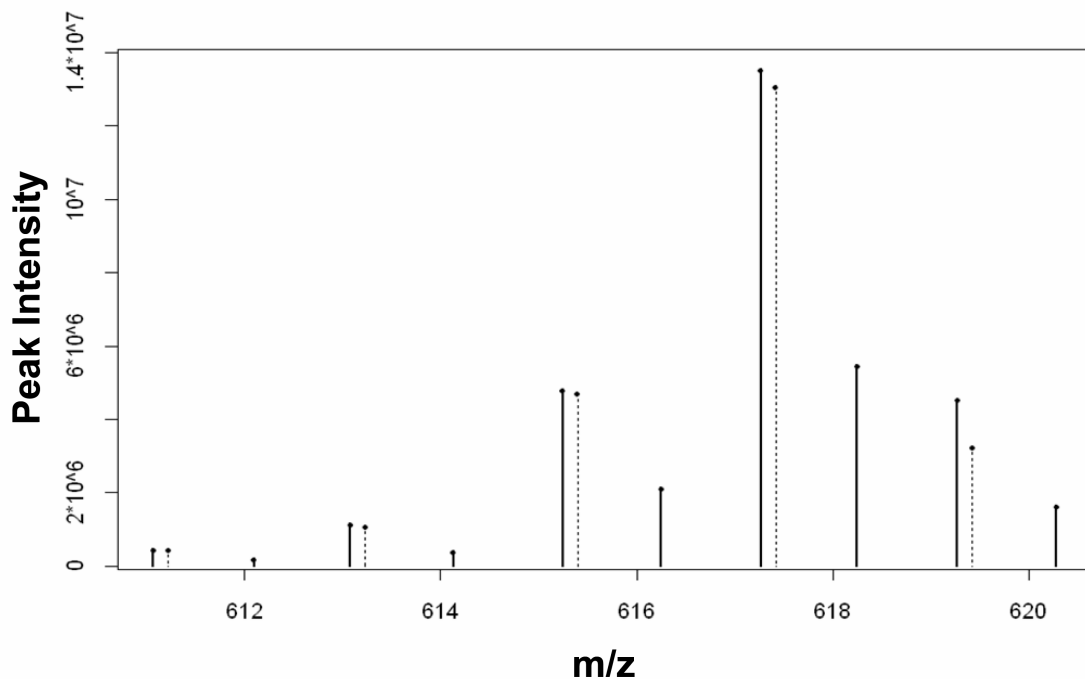


Figure 27: Example of isotopic correction for the m/z range of 611 to 620. This region contains several species of DAG containing 34 carbons in their acyl chains. Solid lines represent the uncorrected signals while the dashed lines are the corrected signals. Isotopic corrections are made from left-to-right, beginning with the species having the second lowest m/z value within the particular group (here, the group of DAGs containing 34 carbons), by subtracting the appropriate proportion of the signal occurring two mass units to the left as explained in Section VI.3.1. Once this signal has been adjusted, it is then used in the same manner to correct the signal for the DAG species having m/z value two units higher. This iterative process continues until the remaining members within the group are corrected.

Table 6: % Total abundance of masses of naturally occurring 38:4 DAG derived from the distributions of isotopes of the constituting elements (carbon, hydrogen, and oxygen).

% total abundance	MW	m/z $[M+Na^+]^+$
0.6211	644.536	667.524
0.2900	645.539	668.527
0.0735	646.542	669.530
0.0132	647.545	670.533
0.0018	648.548	671.536
0.0002	649.551	672.539

6 shows that 62.11% of the total signal generated by sodium adducts of this molecule is observed at m/z 667.52, while 7.35% of the signal appears at m/z 669.53. This is the same m/z value where the primary signal (62.09%) for the 38:3 DAG sodium adduct appears, thus complicating the quantification of these peaks.

Isotopic corrections are made from left-to-right (lower to higher m/z) to the signals within a group of DAG molecules containing the same number of carbons. Beginning with the signal for the DAG species having the second lowest m/z value within a group, the intensity is corrected by subtracting a correction factor based on the signal for the DAG species having m/z value two units less than this species. Figure 27 displays the centroid output for the m/z range 611 to 621; this region contains five species of DAG: 34:4, 34:3, 34:2, 34:1, and 34:0. In the case of 34:3 DAG, the correction factor is calculated by multiplying the intensity at m/z 611.47 (34:4 DAG) by the fraction $.0639/.6500$ representing the ratio of the $[M+Na^{++2}]^+$ to $[M+Na^+]^+$ portion of the 34:4 DAG signal. This factor is subtracted from the intensity at m/z 613.48 (34:3 DAG). This process is then repeated from left-to-right on the remaining members of the 34:X DAG species. The results of these corrections are displayed as dashed lines to the left of each signal line in Figure 27.

VI.3.2 Chromatographic separation and DAG detection

The importance of DAG species in the signaling pathways of cellular networks requires a sensitive method for their efficient detection and quantification. Lipids that do not possess a head group and therefore no electric charge (such as DAGs and triacylglycerols) cannot be detected under normal ESI-MS conditions [25, 29] unless there is a presence of a cation to provide sufficient dipole potential for ionization through complexation. The addition of CH_3COONa (5 mM final concentration) ensures the formation of predominantly Na^+ adducts.

In order to improve detection of DAGs, normal phase chromatography was utilized to separate the DAGs from polar phospholipids (such as phosphatidylcholine (PC))

and phosphatidylethanolamine (PE)), which would otherwise dominate the spectra. Another possible obstacle in DAG quantification is the fact that other products of ligand stimulation could produce peaks at the same m/z as some of the DAG species, thereby obscuring the quantitative results. For that reason the separation technique was also designed to reduce the presence of such products, leaving mainly cellular DAG in the sample. The effectiveness of this technique is illustrated in Figure 26. The m/z range where most PC and PE peaks appear is essentially void of detectable peaks. Because of the high level of sensitivity of the methods for analysis (ESI-MS) and the low levels of DAGs present in the samples, many contaminant peaks were detected at the same or close m/z values as the peaks of interest. With the use of glassware throughout the process of isolation and separation of DAGs and the addition of CH_3COONa , impurity peaks are eliminated, and predominantly $[\text{M}+\text{Na}]^+$ adduct peaks are observed.

VI.3.3 Mathematical analysis of data and development of standard curves

From the analysis of a mixture of DAG standards in the cellular (RAW 264.7) extract background (Fig. 28) in positive ionization ESI-MS, the sensitivity for each DAG species varies greatly between the tested species. This indicates a variable ionization efficiency of individual DAG species. Therefore, the need for normalization of each individual species toward an internal standard was evident since it is well known that peak intensities are dependent on acyl chain and degree of unsaturation [34]. Thus, all samples included 100 ng of 24:0 DAG as an internal standard. This lipid is present in negligible amounts in resting RAW 264.7 cells and was not detected in response to several ligands tested including PAF (data not shown). The intensities for all observed species of DAG in the cellular extracts are expressed in terms of this fixed internal standard. Consequently, the intensity of each species is replaced with the ratio (intensity/24:0 DAG intensity) for modeling purposes.

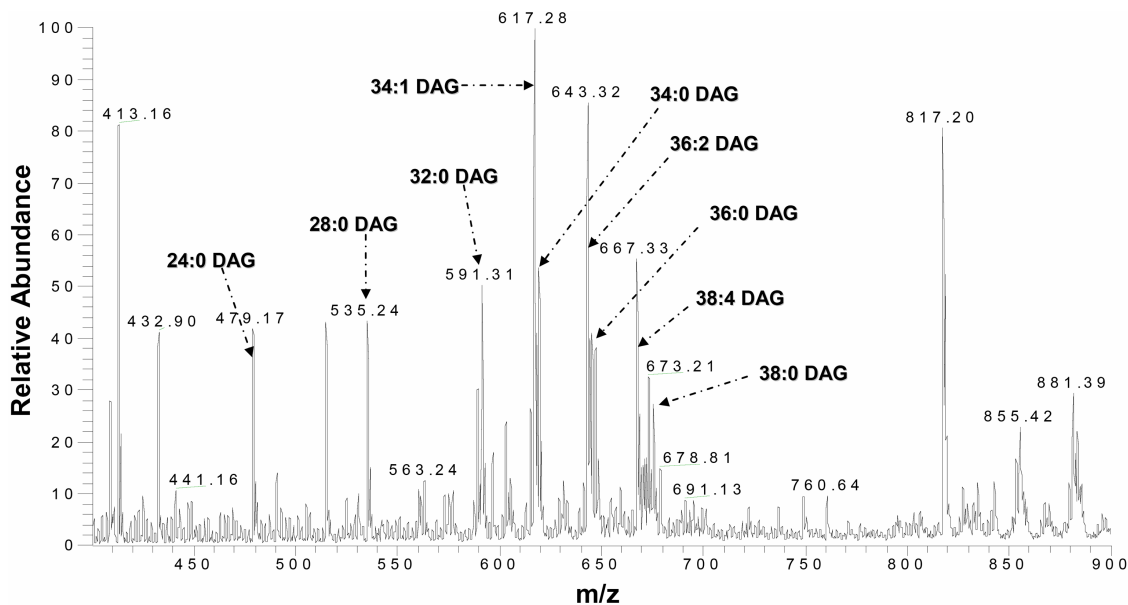


Figure 28: Positive ESI mass spectrum after adding a mixture of 9 diacylglycerol standards to a RAW 264.7 cell background, extracting the phospholipids and then performing a chromatographic separation on a silica gel column to remove the polar phospholipids. 100 ng of each of the following standards was added: 24:0 DAG ($M + Na^+ = 479$), 28:0 DAG ($M + Na^+ = 535$), 32:0 DAG ($M + Na^+ = 591$), 34:1 DAG ($M + Na^+ = 617$)*, 34:0 DAG ($M + Na^+ = 619$), 36:2 DAG ($M + Na^+ = 643$), 36:0 DAG ($M + Na^+ = 647$), 38:4 DAG ($M + Na^+ = 667$), and 38:0 DAG ($M + Na^+ = 675$). *For example, for 34:1 DAG, this corresponds to a concentration of 1.6 pmol/ μ L.

For the development of standard curves, 8 synthetic DAG standards with chemically defined acyl chains were used. The standards included 38:4, 38:0, 36:2, 36:0, 34:1, 34:0, 32:0, and 28:0 DAG, representing a broad range of acyl chain length and degree of unsaturation. To determine the working curves for the 8 DAG species in the presence of a RAW 264.7 cell background, titrations of these compounds were added to cellular preparations. Three separate experiments each with twelve samples containing approximately 3×10^6 RAW 264.7 cells were generated, and these samples were spiked with varying amounts of the 8 DAG standards at 4 different levels in triplicate. Standard additions included 0, 25, 50, and 100 ng in the first two experiments and 0, 10, 75 and 150 ng in the third experiment. In addition, all samples had 100 ng of 24:0 DAG as an internal standard. Samples were extracted and chromatographically

separated as described above, redissolved in 9:1 chloroform:methanol and analyzed by mass spectrometry. After data collection and isotopic correction, the intensities were scaled using the intensity of the 24:0 DAG internal standard and plotted. For each of the 8 standards, the following linear model was utilized to analyze the data:

$$Y_i = \beta_0 + \beta_1 X_{1i} + \beta_{2j} X_{2ji} + \beta_{3j} X_{1i} X_{2ji} + \varepsilon_i, \quad (112)$$

where

Y_i = normalized intensity of sample i ;

X_{1i} = amount of standard added to sample i in ng;

X_{2ji} = factor for experiment containing sample i ;

ε_i = error term for sample i .

In equation (112), the index j runs from 1 to 3 representing the three different experiments, while the index i runs from 1 to 36 for the individual samples in these experiments (i.e., the i indexes 1-12 describe the first experiment, 13-24 the second, and 25-36 the third.). The variable X_{2ji} is an indicator variable (either a 0 or a 1) that takes the value 1 if the index i is an element of experiment j and 0 otherwise. For example, $X_{2,1,11} = 1$ since the 11th sample is part of the first experiment while $X_{2,3,21} = 0$ since the 21st sample is not part of the 3rd experiment. This initial model of the normalized signal intensity fits a total of 8 parameters: β_0 , which represents a global constant term, β_1 which represents a global slope term, β_{21} , β_{22} , and β_{23} which represent corrections to the y-intercept for the individual experiments, and β_{31} , β_{32} , and β_{33} which represent corrections to the slope for the individual experiments. The interaction term $X_{1i} X_{2ji}$ was included to find possible interactions between the experimental preparation and the slope of the working curve for the internal standard, therefore allowing an examination of the effects of cell culture conditions and instrument variability on this slope.

For all examined standards, when this more comprehensive model was compared to the model where $\beta_{31} = \beta_{32} = \beta_{33} = 0$ (no interaction between experiment and slope) using the appropriate F-statistic, there was found to be no significant improvement in the sum of squared deviations. That is, over the tested ranges, the slope for the addition of standard over the background level in the RAW 264.7 cells was not affected by the initial signal level for the tested species, and the simpler linear model with no interaction term was found to be appropriate for modeling purposes. Thus, the lines for the standard additions are statistically parallel, regardless of fluctuations in the initial signal strength. An example of this result is seen in Figure 29.

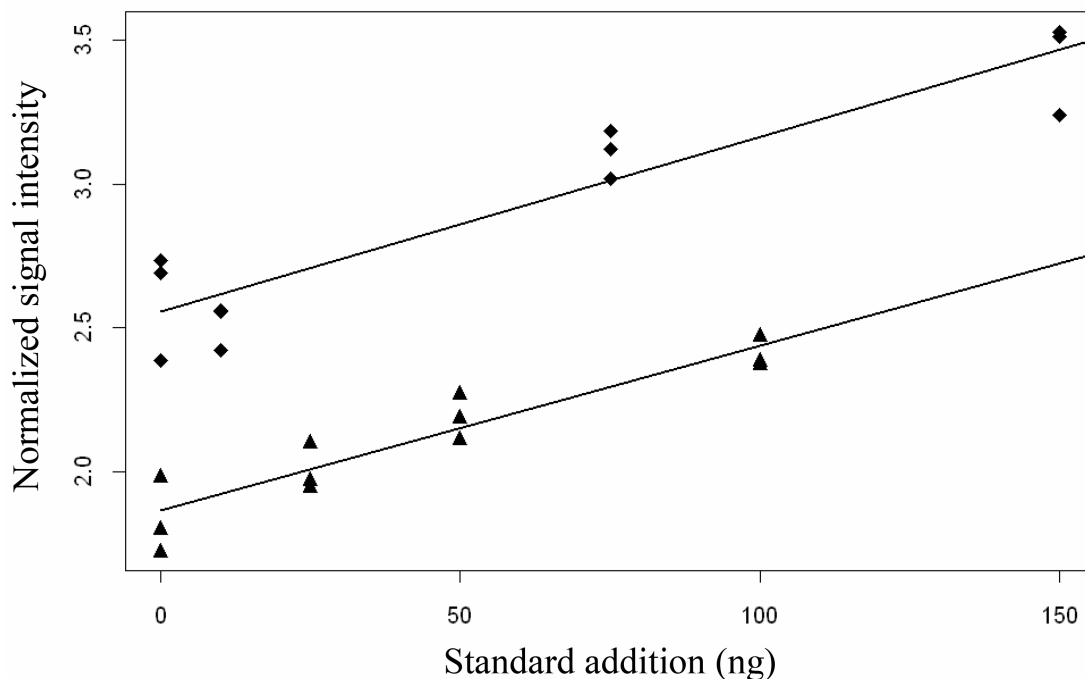


Figure 29: Effects on normalized signal strength of additions of 34:1 DAG to lipid extracts from RAW 264.7 cells. Three separate experiments, each with 12 samples, were performed where RAW 264.7 cells were seeded at 1.5×10^6 cells per well and grown to 80% confluence ($\sim 3.0 \times 10^6$ cells). Prior to addition of chloroform for extraction, 100 ng (0.2 nmol) of 24:0 DAG and varying amounts (10, 25, 50, 75, 100, and 150 ng) of 8 other DAG standards (28:0, 32:0, 34:0, 34:1, 36:0, 36:1, 38:0, and 38:4) were added to samples. Results for the normalized signal strength for 34:1 from experiment 1 (▲) and experiment 3 (◆) are presented with individual best fit lines. The lines are essentially parallel but have different intercepts.

In contrast, the coefficients for the experimental factor representing a correction to the intercept values, β_{21} , β_{22} , and β_{23} , were significant for several of the standards, and may represent variation in cell-culture or the initial signaling state of the preparations.

Using the multiple parameter linear model, the slopes for the 8 DAG species titrated into the RAW 264.7 cell background were computed. These slopes and their associated standard errors are given in Table 7. Multiple parameter linear modeling [70] was accomplished using the S-Plus[®] Version 3.3 for Windows software suite (StatSci division of Mathsoft Inc. Seattle, Washington).

Table 7: Slopes (in normalized signal/ng DAG) for the eight DAG standards determined for the addition to background in a cellular system.

DAG	MW	m/z [M+Na ⁺] ⁺	Multiple R ² ^a	Slope	Std. Error ^b
38:0	652.59	675.59	0.9804	0.00464	0.00012
38:4	644.54	667.53	0.9940	0.01168	0.00017
36:0	624.57	647.56	0.9810	0.00594	0.00015
36:2	620.54	643.53	0.9919	0.01044	0.00025
34:0	596.54	619.53	0.9851	0.00592	0.00015
34:1	594.52	617.51	0.9869	0.00657	0.00038
32:0	568.51	591.50	0.9879	0.00610	0.00016
28:0	512.44	535.43	0.9933	0.01016	0.00015

^aMultiple R² for the overall model fit. ^bStandard error for the slope coefficient.

A single sample of the 36 analyzed was removed from each of these regressions because it displayed a large Cooks distance for seven of the 8 standard curves. Cooks distance [12] provides a method for the identification of points with abnormally high influence in a regression setting. The differences in the slopes for the various DAG species are likely due to solubility/ionization differences in the delivery and ionization of the compounds into the mass spectrometer.

To expand this analysis to encompass all the detectable DAG species, we employed a multiple linear regression model to predict the slope of the working curve for a specific DAG species based on its molecular characteristics. That is, we used the

information obtained with the 8 synthetic standards to predict the behavior of the other DAG species. Specifically, the total number of carbons in the acyl chains and their degree of unsaturation were utilized as independent variables and the slope of the working curve was the dependent variable. This model has functional form:

$$S_i = \alpha_0 + \alpha_1 C_{1i} + \alpha_2 C_{2i} + \varepsilon_i, \quad (113)$$

where

S_i = slope for the i th DAG species observed intensity;

C_{1i} = total number of carbons present in the acyl chains minus 24;

C_{2i} = degree of unsaturation in the acyl chains
(total number of double bonds present);

ε_i = error term.

Our analysis included DAG species containing at least 24 total carbons in their acyl chains, since shorter acyl chains are uncommon in mammalian cells, and the variable C_{1i} is adjusted to reflect this value as 0 (e.g. for a 38 carbon-containing DAG species, the value of C_{1i} is $38 - 24 = 14$). This multiple parameter linear model was based on the results from the 8 standards, and had a multiple R^2 -value of .851, indicating that over 85% of the variation in the slopes for the various DAG species can be accounted for with these two variables. The coefficients of this model for the assay system are presented in Table 8.

The predicted slopes for the 8 synthetic standards were calculated for comparison with those observed empirically (Table 9). Using the model, the predicted slopes for the other 20 DAG species in our assay panel were computed. For example, the predicted slope for 34:2 DAG would be calculated as: $0.01103 - 0.00048(34 - 24) + .00190(2) = .01003$. A range of total carbons from 28 to 38 and 0 to 6 double bonds were considered.

Table 8: Coefficients for the multiple parameter linear model in equation (113) used to estimate the slopes of the calibration curves for species of DAG not included in the titration analysis.

Coefficient	Value	Std. Error
α_0^a	0.01103	0.00157
α_1^b	-0.00048	0.00016
α_2^c	.00190	0.00036

^aGlobal intercept. ^bSlope coefficient for the acyl chain length.

^cSlope coefficient for degree of unsaturation.

Slopes shown in Table 9 were incorporated into a program written in S-Plus[®] for the rapid quantitative analysis of a total of 28 DAG species. For the 8 species for which the slopes were directly measured, this value was utilized in the software. The other 20 species were measured using the estimated slope value from the linear model. To estimate the level of detection for the method, we employed the Residual Standard Error (RSE) of the model used in the determination of the slope of the calibration curve, which estimates the variance around the calibration curve, and the slope of the curve, from which the detectable amount of each lipid species can be computed. That is, the detectable limit for a two sample t-test was calculated with equal variances set to the RSE, and this number was divided by the slope of the calibration curve. This produces an approximation to the minimum amount of lipid which can be detected with the method. The results for the 8 internal standards are presented in Table 10.

Approximate limit of detection (LOD) values for the other 20 DAG species were computed in a similar manner, using the predicted slope from Table 9 and the baseline variability of each DAG species in place of the RSE. The differences in the detection limit are likely caused by a variance in the sample preparation, and the larger limits of detection correlate with the species (e.g. 34:1) present in larger quantities in resting RAW 264.7 cells.

The method is applicable to other cellular extracts with different lipid compositions and backgrounds (e.g., presence of other neutral lipids in the analyzed fractions)

Table 9: Predicted slopes for the 28 species of DAG determined from the linear model whose coefficients are displayed in Table 8.

DAG Species	MW	m/z [M+Na ⁺] ⁺	Observed Slope ^a	Predicted slope ^b
38:0	652.60	675.59	0.00464	0.00431
38:1	650.58	673.57	N/A	0.00621
38:2	648.57	671.56	N/A	0.00811
38:3	646.55	669.54	N/A	0.01001
38:4	644.54	667.53	0.01168	0.01191
38:5	642.52	665.51	N/A	0.01381
38:6	640.51	663.50	N/A	0.01571
36:0	624.57	647.56	0.00594	0.00527
36:1	622.55	645.54	N/A	0.00717
36:2	620.54	643.53	0.01044	0.00907
36:3	618.52	641.51	N/A	0.01097
36:4	616.51	639.50	N/A	0.01287
36:5	614.49	637.48	N/A	0.01477
34:0	596.54	619.53	0.00592	0.00623
34:1	594.52	617.51	0.00657	0.00813
34:2	592.51	615.50	N/A	0.01003
34:3	590.49	613.48	N/A	0.01193
34:4	588.48	611.47	N/A	0.01383
32:0	568.51	591.50	0.00610	0.00719
32:1	566.49	589.48	N/A	0.00909
32:2	564.48	587.47	N/A	0.01099
32:3	562.46	585.45	N/A	0.01289
30:0	540.48	563.47	N/A	0.00815
30:1	538.46	561.45	N/A	0.01005
30:2	536.44	559.43	N/A	0.01195
30:3	534.43	557.42	N/A	0.01385
28:0	512.44	535.43	0.01016	0.00911
28:1	510.43	533.42	N/A	0.01101

^aEmpirically observed slope calculated for the assay conditions.

^bSlope estimate calculated from the linear model.

Table 10: Approximation for the limit of detection (ng) for the 8 internal standards used in the titration experiments^a.

DAG	RSE ^b	slope ^c	LOD ^a					
			1- β = .50			1- β = .75		
			power of test number of replicates	3	6	9	3	6
38:0	0.03052	0.00464	11.44 ^d	6.88	5.41	15.43	9.55	7.56
38:4	0.04271	0.01168	6.36	3.66	3.01	8.58	5.3	4.2
36:0	0.03866	0.00594	11.32	6.8	5.35	15.27	9.44	7.47
36:2	0.06476	0.01044	10.79	6.49	5.11	14.55	8.99	7.13
34:0	0.03911	0.00592	11.5	6.91	5.44	15.49	9.58	7.58
34:1	0.09741	0.00657	25.81	15.51	12.21	34.78	21.77	17.03
32:0	0.0403	0.0061	11.49	6.92	5.44	15.49	9.59	7.59
28:0	0.03886	0.01016	6.65	4.01	3.15	8.97	5.55	4.39

^aLimit of detection for the method was based on a two-sample t-test for a test with power (1 - probability of a Type II error) of 0.50 and 0.75, with three, six, and nine replicates respectively. The alpha level for all results was 0.05. ^bResidual Standard Error for the linear model. ^cSlope of the calibration curve. ^dA limit of detection of 11.44 ng for 38:0 DAG corresponds to a concentration of 167 fmol/ μ l (or 17.5 pmol/sample).

after recalculating the slopes for the standard curves as described above and then performing the linear regression technique using the newly defined slopes. Figure 30A illustrates the linear relationship between the spiked and detected amounts of DAGs in different cell extracts despite differences in the DAG peaks environment in the mass spectra (Fig. 30B). By contrast a plasma preparation was analyzed by the same approach. Short carbon chain DAG internal standards demonstrate good linearity, while significant problems were encountered in accurate quantification of long-chain polyunsaturated DAG species. Whether this was the result of selective enzymatic processes that survived typical heat inactivation protocols (data not shown) or more complex contaminants present in plasma (relative to cell extracts) that contribute to ion suppression is unknown. This is the focus of ongoing investigation.

VI.3.4 Quantification of DAG species in RAW 264.7 cells after PAF stimulation

To illustrate the method, RAW 264.7 cells were stimulated with 100 nM PAF, for 30 s, 1 min, 2 min, 3 min, and 5 min. PAF is a proinflammatory phospholipid affecting various processes, including increasing cell permeability of blood vessels and contracting assorted involuntary muscles. PAF stimulates G-protein coupled receptors which activate phospholipase C and phospholipase A2 enzymes inducing the formation of DAG and arachidonic acid, respectively.

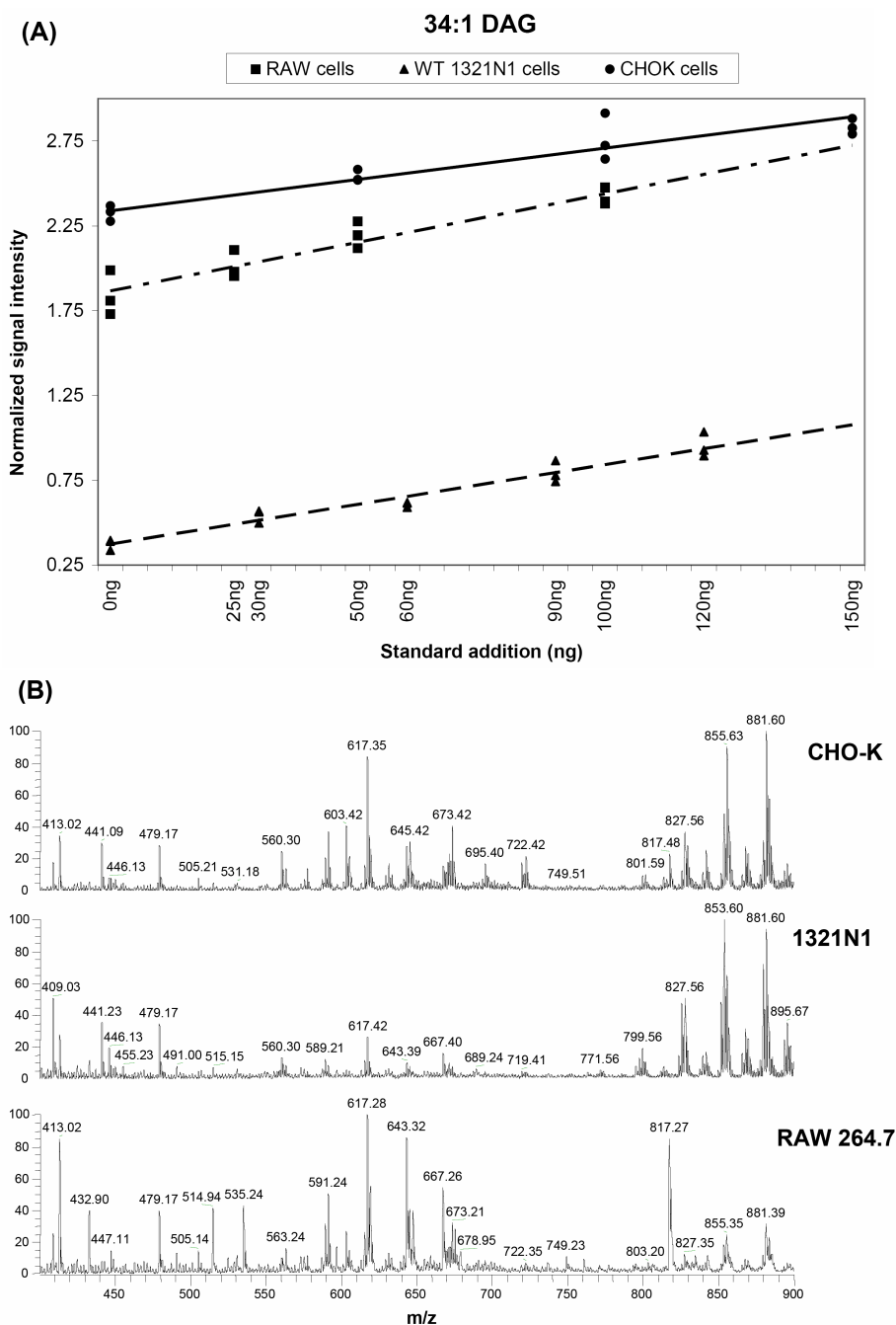


Figure 30: Illustration of differences in standard curves among different cellular extracts. Three different cellular extracts (RAW 264.7 macrophages, 1321N1 astrocytoma cells, and CHO-K ovarian cells) were tested using the method, by adding the indicated amounts of DAG standards (see panel A) to the extracts. Though the slopes for the standard curves may be different for each cellular extract, as is the case for 34:1 DAG (A), the relationships remain linear and the method of multiple linear regression may still be applied to determine slopes of the remaining DAG species. The spectra of the three cellular extracts with addition of 24:0 DAG internal standards are shown in panel B.

The graphical results for 4 of the 28 DAG species measured are shown in Figure 31. Panels 31A and 31B show the kinetic behavior of 32:0 and 34:1 DAG. Both species depict a slight initial decrease from baseline, followed by an increase at 1 minute, and a subsequent and sustained decrease to levels below baseline. This response was observed in most of the saturated and mono- and di-unsaturated fatty acid containing DAG species.

In contrast, the PUFA-containing 38:4 and 38:5 DAG species in panels 31C and 31D display a drastically different trend, which was representative of all of the PUFA-containing DAGs. They remain near baseline levels at 30 seconds and then exhibit a sustained increase over baseline throughout the time course. These results demonstrate species-dependent differential metabolism of DAGs suggesting specificity in DAG metabolic pathways determined by acyl chain composition. Clearly, a full understanding of DAG metabolism requires an analytical method that provides the detection and quantification of the individual species.

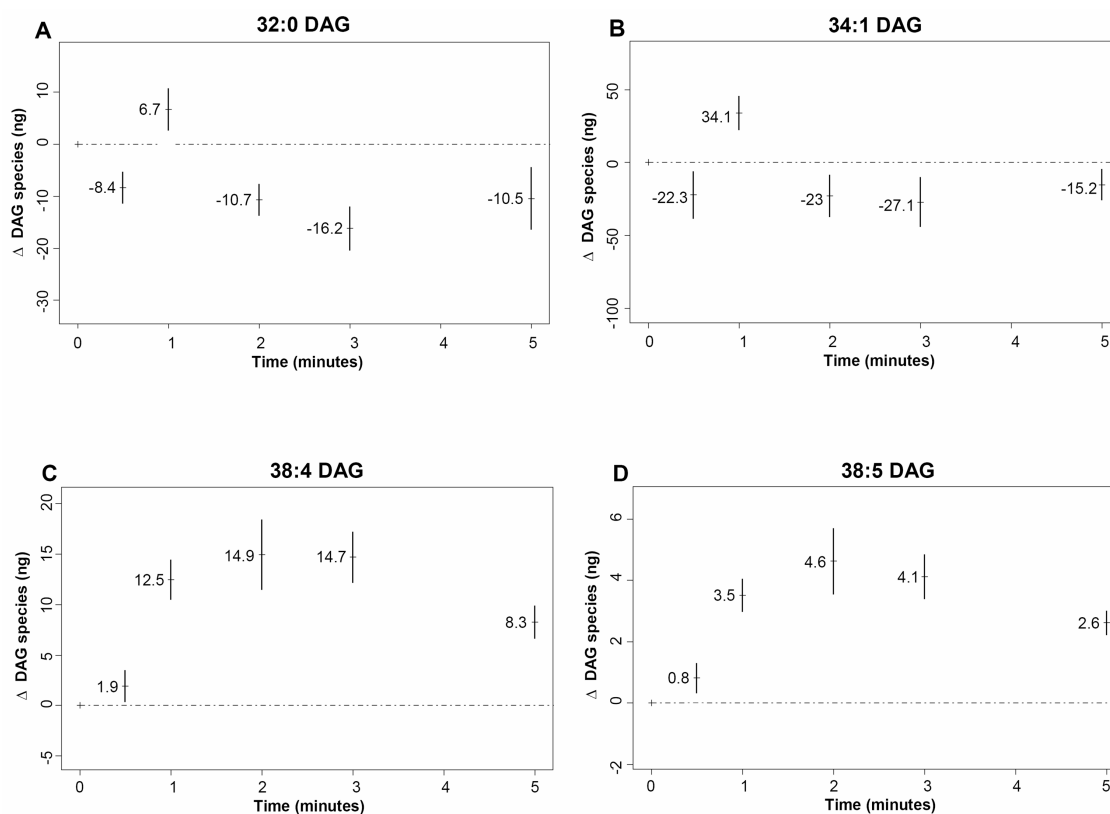


Figure 31: Time-based behavior of four DAG species, with varying numbers of carbons and double bonds, after addition of 100 nM PAF. The cellular DAG levels were measured as described in Section VI.3.3, using ESI-MS after chromatographic separation. Time points contain a minimum of 9 replicates performed on three different experimental days. Error bars represent 2 SEM. In panels A and B PAF addition results in an initial decrease in total cellular DAG content that is followed by a brief increase and subsequent decrease over baseline levels. In panels C and D, however, PAF addition results in an immediate increase in total cellular DAG that is maintained throughout the tested time course.

CHAPTER VII

CONCLUSIONS AND FUTURE DIRECTIONS

VII.1 Modeling Results

A mathematical model of the UDP signaling pathway in RAW 264.7 macrophages has been developed to better understand the underlying mechanisms of species-specific DAG production and degradation. In order to capture the necessary elements and behaviors of this complex signaling pathway while also maintaining a certain degree of simplicity, a minimalistic yet realistic approach has been taken, and a successful quantitative representation of the events downstream activation of the P2Y₆ receptor has been achieved.

The mechanisms of receptor activation and desensitization were modified for the P2Y₆ receptor from a detailed description given by Lemon in P2Y₂ receptors [39] in order to accurately represent the slow receptor internalization of surface P2Y₆ receptors seen by Brinson and Harden [6].

There are multiple pathways which could be involved in the production of IP₃ and DAG, as multiple G-protein subunits and isoforms can activate multiple isoforms of PLC. This often depends on the cell type under consideration as well as the receptor or receptors undergoing stimulation. Since P2Y₆ receptors have been shown to couple to the G α_q isoform [86], and PLC β -3 isoforms have been shown to exhibit strongest sensitivity to G α_q [72], we have assumed a single mechanism for PIP₂ hydrolysis: activation of G α_q and PLC β -3.

As modeling Ca²⁺ dynamics was not been a focus of this work, Ca²⁺ contribution in the signaling pathway was formed after a model previously developed by Li and Rinzel [40] and was handled in such a way as to treat Ca²⁺ more as an input into the model. Therefore, parameter values for the Ca²⁺ module were chosen so as to

most accurately mimic the experimental Ca^{2+} data in the RAW 264.7 population data from the Alliance for Cellular Signaling (<http://www.signaling-gateway.org>).

Initial efforts using the canonical pathway for DAG production and degradation (via PIP_2 hydrolysis only) were unsuccessful, as we were unable to reproduce the behavior seen experimentally from different species of DAG. In particular, the biphasic dynamics of mono- and di-unsaturated DAGs could not be reproduced for any choice of parameter values. Furthermore, the general theory that later DAG production originates from PLD activity does not hold true in RAW 264.7 macrophages stimulated with UDP, as we found there to be no PLD activity in these cells post agonist stimulation with UDP. Instead, upon incorporating into this canonical pathway a known pathway in DAG metabolism involving a second pool of DAG present in high concentrations in resting cells, we were able to obtain *in silico* results comparable to those seen empirically. Under this two-pool model structure for DAG kinetics shown in Figure 2, we could reproduce differential kinetics among multiple species of DAG, holding all parameters fixed except those directly related to the production and degradation associated with different DAG species. For the same choice of all remaining rate parameters, we obtained a good fit for the experimental results of IP_3 and Ca^{2+} .

Sensitivity analysis of model output to variations in model parameters was performed using a multiple linear regression model. The vast majority of model coefficients of determination, R_y^2 , were all sufficiently close to one for all time points and for all model outputs, with the smallest values being greater than 0.8. Thus, the standardized regression coefficients were proven to be appropriate measures of parameter sensitivity. Both IP_3 and DAG were shown to be sensitive to the rate of receptor phosphorylation, k_p , and the rate of PIP_2 replenishment, k_{rep} , suggesting that the uncertainty in the output of these two variables could be significantly reduced by obtaining a better estimate of these two rate parameters. DAG was seen to be most sensitive to the activation and degradation parameters of DAG_{p2} and the degradation

rate of DAG_{p1}, which were all directly estimated from the experimental data.

Rigorous analysis of the model behavior proved the local existence and uniqueness of the full system of nonlinear ODEs, while global existence as well as positivity and boundedness of solutions was established for the simplified model. Steady states for the simplified model were also shown to be globally asymptotically stable within the region of biological interest.

Ongoing work involves investigation of stability behavior for the full model, involving the three-equation system for Ca²⁺ dynamics. We would also like to relax the assumption of a well-mixed cell to include the spacial aspects of the UDP signaling pathway through incorporation of partial differential equations as well as inclusion of delay terms to better represent what is seen experimentally and known to be true biologically.

VII.2 Pathway Analysis Results

As the mathematical modeling suggested the addition of another branch in the signaling pathway, we conducted a set of experiments to test this hypothesis. First, the two-dose UDP data showed that both levels of UDP produce a similar DAG response out to 15 minutes. For the higher UDP dose, the level of DAGs produced at 15 minutes was slightly higher than in the lower dose. Furthermore, the response from the higher dose peaked at 15 minutes and was recovering by 30 minutes, whereas the levels for the lower dose at 30 minutes were either similar to those at 15 minutes or slightly higher. This suggests that for the higher dose, the cells are responding more rapidly.

Next, there were two major results from the R59949 study: 1) the inhibitor caused a decrease in DAG levels over baseline, though not all of these decreases were seen to be significant, and 2) for most of the PUFA-containing and mono- and di-unsaturated DAGs, the inhibitor had the greatest effect at the 30 second time point, where levels were significantly higher with cells pretreated with 10 μ M R59949 and stimulated

with 25 μ M UDP compared to non-pretreated cells stimulated with 25 μ M UDP. This data suggests a role for DAG kinase in these DAG species immediately after UDP stimulation.

Although Propranolol had no effect on the UDP response for 38:4 DAG, it appeared to eliminate the UDP response in many of the mono- and di-unsaturated DAGs. This together with the R59949 data suggests an interplay between DAG kinase and LPP. We also conducted a global lipid analysis of the effects of Propranolol. In unstimulated cells pretreated with Propranolol, we observed an increase in levels of mono- and di-unsaturated and saturated PAs throughout the tested timecourse, suggesting that there exists a constitutively active DAG kinase and lipid phosphate phosphatase which are phosphorylating mono- and di-unsaturated and saturated DAGs and dephosphorylating mono- and di-unsaturated and saturated PAs, respectively, in resting cells. In stimulated cells pretreated with Propranolol, however, there was no significant increase in the mono- and di-unsaturated and saturated PAs over the amount of PA produced from Propranolol alone. For the PUFA-containing DAGs, especially 38:4 DAG, Propranolol had essentially no effect on the UDP response. For most of the PUFA containing PAs, Propranolol did not significantly increase levels in resting cells and had no significant effect on the UDP response. This also agrees with our two-pool model (Fig. 2), if we assume that Propranolol is affecting the transfer of PI to the plasma membrane: If there exist resting levels of mono- and di-unsaturated and saturated DAGs, inhibition of constitutively active LPP would lead to a depletion of the DAG pool and an increase in PA. If the remaining parts of the pathway were left intact, upon stimulation we should still see an increase in these DAG species through PA conversion to CDP-DG to PI, which is shuttled to the plasma membrane, phosphorylated to phosphatidylinositol monophosphate and again to PIP₂, which is hydrolyzed to form DAG. Since we did not see an increase in mono- and di-unsaturated and saturated DAGs with Propranolol and UDP, we must assume Propranolol is somehow affecting this part of the pathway. We still have an increase

in PUFA-containing DAGs when cells have been pretreated with Propranolol since the majority of these DAGs were coming from hydrolysis of existing PIP₂. There was also no increase in PUFA-containing PAs after pretreatment with Propranolol since there were low basal levels of PUFA-containing DAGs.

The remaining inhibitors tested at the 15 minute time point gave responses in agreement with the two-pool model for DAG production. Of special mention is the effect of U73122, which essentially eliminated the UDP response for most of the DAG species. This behavior would be expected within the two-pool model pathway structure, as the majority of DAG production from UDP stimulation comes through hydrolysis of PIP₂.

VII.3 DAG Quantification Results

Finally, we demonstrate here that DAG molecular species can be reliably quantified from a cellular extract by ESI-MS. The newly developed multiple linear regression model for raw mass spectral data analysis allows adjustment for the differences in ionization due to the differences in acyl chain composition as well as compensation for the nature of the lipid extracts (cell type and/or instrumental variability). The methodology described here also calculates the contributions of individual isotopic molecular species to each parent ion peak, making it more accurate and useful in the quantitative determination of a low abundant class of lipids such as diacylglycerols. The optimized ionization and detection conditions together with the inclusion of an internal standard permit the quantitative determination of 28 DAG species present in a RAW 264.7 cell extract after ligand stimulation. The differential kinetic behavior of DAG species with different acyl chain composition after PAF stimulation suggests a differential metabolism. With respect to the individual species detection and quantification, the proposed analytical method offers a valuable tool for comprehensive understanding of DAG metabolism. This work also provides an example of metabolomic profiling of mammalian cells. Differences between any two states can

be compared (e.g., with or without a receptor ligand) in a discovery phase approach [20, 63] which allows identification of changes in the relative abundance of different lipid classes and even individual lipid species. Subsequent absolute quantification of these changes require optimized separation approaches with tailored internal standards, such as those described here. The comprehensive analysis of species level changes in the cellular lipome is an essential goal in understanding cellular networks and identification of novel biomarkers.

APPENDIX

A. Additional SIMULINK Figures

Here we include all SIMULINK subsystems contained in the full SIMULINK model in Figure 4 as well as a list of all blocks used and their corresponding function.

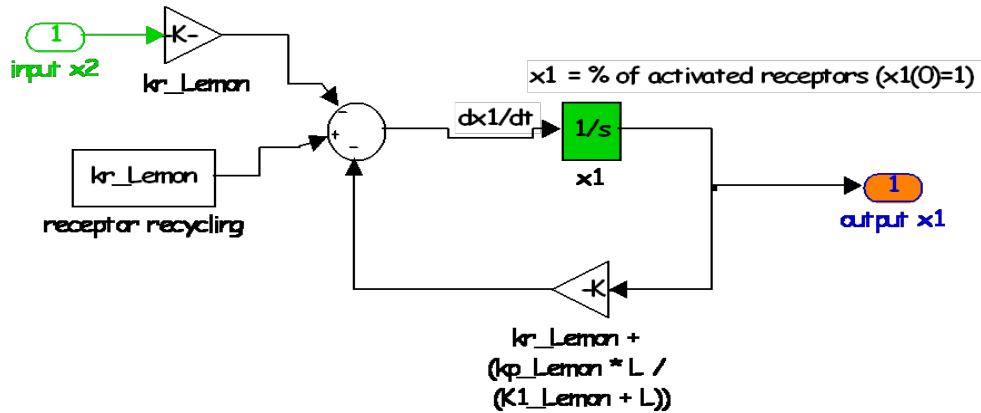


Figure 32: SIMULINK activated receptor subsystem.

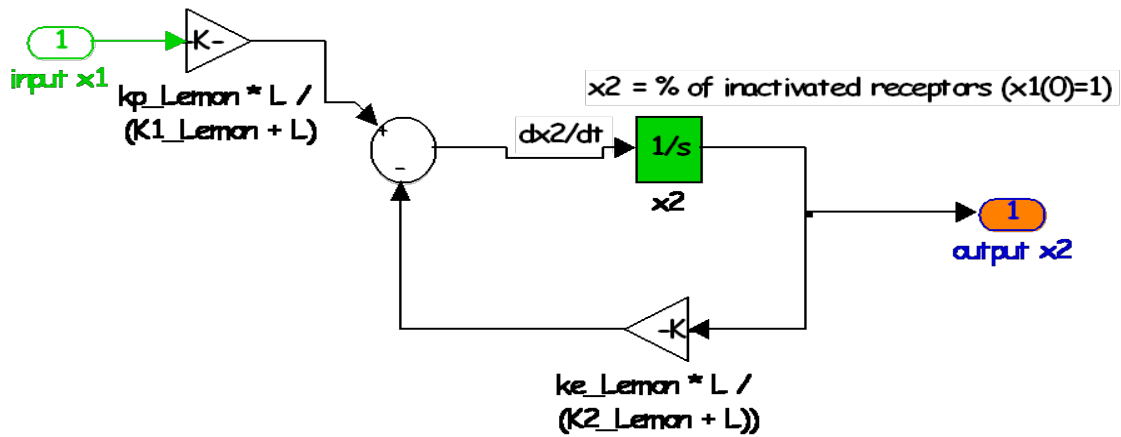


Figure 33: SIMULINK inactivated receptor subsystem.

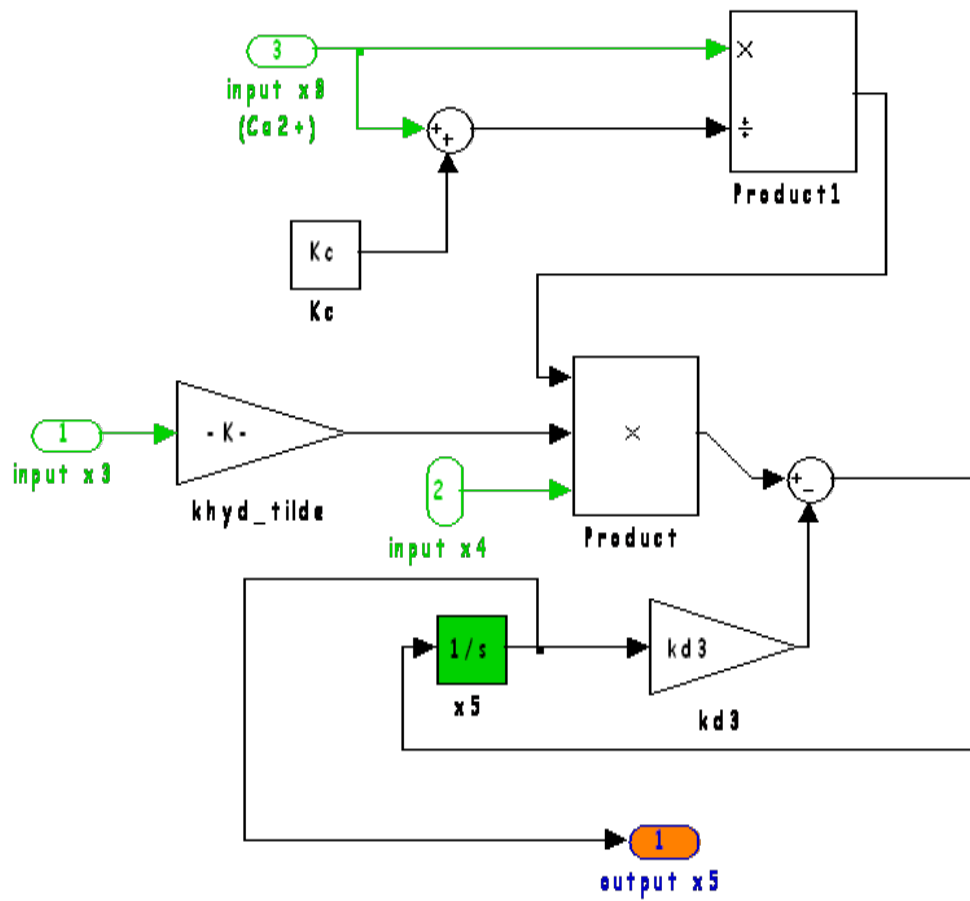


Figure 36: SIMULINK IP₃ subsystem.

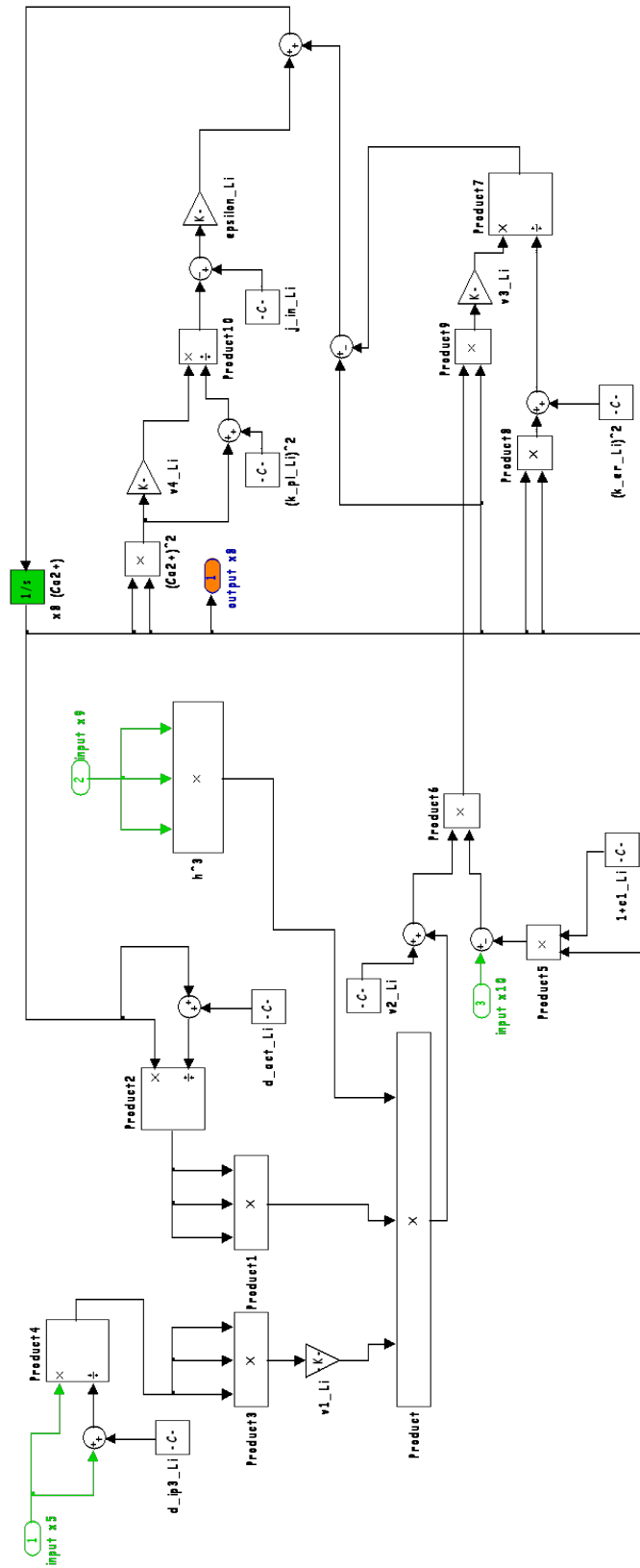


Figure 39: SIMULINK Cytosolic Ca^{2+} subsystem.


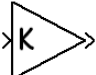

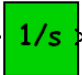

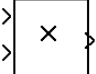
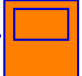

BLOCK	FUNCTION
 Constant	Output a specified constant
 Gain	Element-wise gain (output = $K \cdot \text{input}$) or matrix gain (output = $K \cdot \text{input}$ or output = $\text{input} \cdot K$)
 In1	Provide an input port for a subsystem or model
 Integrator	Continuous-time integration of the input signal
 Out1	Provide an output port for a subsystem or model
 Product	Multiply or divide inputs
 Scope	Display time-dependent output of a simulation
 Sum	Add or subtract inputs

Figure 42: SIMULINK blocks used in the model from Figure 4.

B. MATLAB Code for Numerical Simulations

Here we include the MATLAB code used to generate all numerical simulations from Section IV.2 and to perform sensitivity analysis discussed in Section IV.3.

B.1 M-file to create sample matrix

```
%-----  
% create_sample_matrix.m  
  
% THIS FILE IS USED TO CREATE A RANDOM SAMPLE MATRIX USING SIMLAB  
% AND IS MADE TO RUN ON "hannah_odes.m" and "run_hannah_odes.m"  
% THIS FILE IS A DERIVATIVE OF SIMLAB'S "sampleRepLatin.m" FILE  
% WHICH CAN BE FOUND ON THE SIMLAB WEBSITE:  
  
% http://simlab.jrc.cec.eu.int/  
%-----  
  
global final_time runstot sample  
  
runstot = 5000; % total number of samples created  
% equals total number of rows in sample matrix  
  
gsaBegin %opens SIMLAB  
  
% Below we add each input factor (parameter) using a uniform  
% distribution where the left and right endpoints are 10% variations  
% from the nominal value  
  
addFacUnif('p1',1,[432,528,1],'initial_384_DAG')  
addFacUnif('p2',1,[450,550,1],'initial_341_DAG')
```

```

addFacUnif('p3',1,[18000,22000,1],'RT')
addFacUnif('p4',1,[0.0001575,0.0001925,1],'kr_Lemon')
addFacUnif('p5',1,[0.001575,0.001925,1],'kp_Lemon')
addFacUnif('p6',1,[0.0054,0.0066,1],'ke_Lemon')
addFacUnif('p7',1,[4.5,5.5,1],'K1_Lemon')
addFacUnif('p8',1,[90,110,1],'K2_Lemon')
addFacUnif('p9',1,[270000,330000,1],'GT')
addFacUnif('p10',1,[22.5,27.5,1],'L')
addFacUnif('p11',1,[0.1233,0.1507,1],'ka_tilde')
addFacUnif('p12',1,[0.018,0.022,1],'kd')
addFacUnif('p13',1,[0.000009,0.000011,1],'khyd_tilde')
addFacUnif('p14',1,[0.0126,0.0154,1],'krep')
addFacUnif('p15',1,[0.0054,0.0066,1],'kd3')
addFacUnif('p16',1,[8100000,9900000,1],'PIP2T')
addFacUnif('p17',1,[0.001539,0.001881,1],'k_dp2')
addFacUnif('p18',1,[0.001764,0.002156,1],'k_ap2')
addFacUnif('p19',1,[0.00108,0.00132,1],'k_dp1')
addFacUnif('p20',1,[0.36,0.44,1],'Kc')
addFacUnif('p21',1,[0.405,0.495,1],'x7fac')

setMethodLatin(14237,runstot) % the first number is the seed, and the
% second number is the number of samples I want to generate using the
% Latin Hypercube sampling method

sample = createSample
% generate random sample and store under "sample"

```

```

%sample_42 = [480 500 20000 0.000175 0.00175 0.006 5 100 300000 25
%0.137 0.02 1.00E-05 0.014 0.006 9000000 0.00171 0.00196 0.0012 0.4
%0.45]; %This sets the sample to all of the nominal values

```

```

%-----

```

B.2 M-file defining system of ODEs

```

function xdot = hannah_odes(t,x)

```

```

%HANNAH_ODES

```

```

%xdot = hannah_odes(t,x)

```

```

%-----

```

```

% Declaring global variables to be seen by "hannah_odes.m" as well as
% "create_sample_matrix.m" and the m-file to run the numerical
% simulations called "run_hannah_odes"

```

```

global Nav v m2uM kr_Lemon kp_Lemon ke_Lemon RT K1_Lemon K2_Lemon GT

```

```

global ka_tilde kd lambda khyd_tilde krep kd3 PIP2T PIP2T_conc k_dp2

```

```

global k_ap2 k_dp1 Kc CaT Kctilde L

```

```

global v1 d_ip3 d_act v2 c1 v3 k_er epsilon j_in v4 k_pl a d_inh

```

```

global zeta_341 zeta_384

```

```

global initial_384_DAG initial_341_DAG

```

```

global P i final_time runstot % global variables for random parameter

```

```

% matrix "P"

```

```

%-----

```

```

% Temp equations for Calcium module

```

```

temp1 = x(5)/(x(5) + d_ip3);

```

```

temp2 = x(8)/(x(8) + d_act);
temp3 = (x(8)*x(8))/(k_er*k_er + x(8)*x(8));
temp4 = (x(8)*x(8))/(k_pl*k_pl + x(8)*x(8));
temp5 = d_inh / (x(8) + d_inh);

%-----
% XDOT: xdot with the random sample parameter matrix P (built in the
% file "create_sample_matrix.m")
xdot = [P(i,4) * P(i,3) - (P(i,4) + (P(i,5) * P(i,10) / (P(i,7) +
      P(i,10))))*x(1) - P(i,4) * x(2); % x(1) = activated receptors
      P(i,10)*((P(i,5)*x(1) / (P(i,7) + P(i,10))) - ((P(i,6)*x(2))/
      (P(i,8) + P(i,10))))); % x(2) = phosphorylated receptors
      P(i,11)*m2uM*x(1)*(P(i,9)-x(3)) - P(i,12)*x(3); % x(3) = GaGTP
      -P(i,13) * x(8) / (P(i,20) + x(8)) * x(3) * x(4) + P(i,14) *
      (P(i,16) - x(4)); % x(4) = PIP2
      P(i,13)* x(8) / (P(i,20) + x(8)) * x(3) * x(4)* m2uM -
      P(i,15) * x(5); % x(5) = IP3
      P(i,13) * x(8) / (P(i,20) + x(8)) * x(3) * x(4)* m2uM -
      P(i,19) * x(6) + P(i,17)*P(i,21)*x(7); % x(6) = DAGp1
      -P(i,17) * x(7) + P(i,18) * (P(i,2) - x(7)); %x(7) = DAGp2
      (v1*(temp1*temp1*temp1)*(temp2*temp2*temp2)*((x(9))^3) +
      v2) * (x(10) - (1 + c1) * x(8)) - v3 * temp3 + epsilon *
      (j_in - v4 * temp4); %x(8) = Ca2+
      a * (x(8) + d_inh) * (temp5 - x(9)); %x(9) = h
      epsilon * (j_in - v4 * temp4)]; %x(10) = c0
%-----

```

B.3 M-file to run simulations and sensitivity analysis

```
%RUN_Hannah_Odes
%Script file to run hannah_odes and output plot
%-----

%Clearing statistical variables
clear res1 resint1 src1 srcint1 R2Fpe1
clear res2 resint2 src2 srcint2 R2Fpe2
clear res3 resint3 src3 srcint3 R2Fpe3
clear res4 resint4 src4 srcint4 R2Fpe4
clear res5 resint5 src5 srcint5 R2Fpe5
clear res6 resint6 src6 srcint6 R2Fpe6
clear res_DAG resint_DAG src_DAG srcint_DAG R2Fpe_DAG
clear res7 resint7 src7 srcint7 R2Fpe7
clear res8 resint8 src8 srcint8 R2Fpe8
clear res9 resint9 src9 srcint9 R2Fpe9
clear res10 resint10 src10 srcint10 R2Fpe10
clear b1 bint1 r1 rint1 stats1
clear b2 bint2 r2 rint2 stats2
clear b3 bint3 r3 rint3 stats3
clear b4 bint4 r4 rint4 stats4
clear b5 bint5 r5 rint5 stats5
clear b6 bint6 r6 rint6 stats6
clear b341 bint341 r341 rint341 stats341
clear b7 bint7 r7 rint7 stats7
clear b8 bint8 r8 rint8 stats8
clear b9 bint9 r9 rint9 stats9
clear b10 bint10 r10 rint10 stats10
```



```

clear i j k m q tspan final_time P

%-----
% Declaring global variables to be seen by "hannah_odes.m" as well as
% "create_sample_matrix.m" and the m-file to run the numerical
% simulations called "run_hannah_odes"
global Nav v m2uM kr_Lemon kp_Lemon ke_Lemon RT K1_Lemon K2_Lemon GT
global ka_tilde kd lambda khyd_tilde krep kd3 PIP2T PIP2T_conc k_dp2
global k_ap2 k_dp1 Kc CaT L
global v1 d_ip3 d_act v2 c1 v3 k_er epsilon j_in v4 k_pl a d_inh
global zeta_341 zeta_384
global initial_384_DAG initial_341_DAG
global P i final_time runstot sample
% global variables for random parameter matrix
%-----

P = sample; % random sample matrix of model parameters for
% "hannah_odes.m"

final_time = 450; % number of points to plot for each graph
tspan(1) = 0;
for j = 2:final_time + 1
    tspan(j) = tspan(j-1)+4;
end

% tspan = [0 1800]; % set time span to integrate over 1800 seconds
% x0 = [1,0,0,1,0,0,1,0.00058,0.8,2]; % sets initial conditions
%-----

```

```

% Conversion constants
Nav = 6.02252e23; % Avogadro's constant

v = 5e-13; % Cell volume in L; taken from Sasada 1983, who used
% 395-589 um^3 which is approximately 5e-13L since 1 m^3=1000 L
% (also, 1e15 um^3 = 1 L) (1 um = 1 micron)

m2uM = 1 / (Nav * v * 1e-6); % multiply this by # of molecules to get
% concentration in uM

uM2pmoles = 1e6 * 5e-013; % multiply this by quantity in uM to get
% # of pmoles

uM2ng384 = 1e3 * v * 644; % multiply this by quantity in uM to get
% # ng of 38:4 DAG (since mass of 38:4 is 644)

uM2ng341 = 1e3 * v * 594; % multiply this by quantity in uM to get
% # ng of 34:1 DAG (since mass of 34:1 is 594)

initial_384_DAG = 480; % calculated value
% P(i,1)

initial_341_DAG = 500; % calculated value
% P(i,2)
%-----

% Parameters for Lemon's receptor equations
% NOTE: These parameters fit Harden 2001 P2Y6 data as well
RT = 20000; % total number of P2Y2 receptors in 1321N1 cells

```

```

% taken from Garrad et al. (1998)
% P(i,3)

kr_Lemon = 0.000175; % (in /s)
% taken from Lemon
% receptor recycling rate
% P(i,4)

kp_Lemon = 0.00175; % (in /s) receptor phosphorylation rate
% best fit for SIMULINK estimation 070404d
% P(i,5)

ke_Lemon = 0.006; %(in /s) receptor endocytosis rate
% taken from Lemon
%P(i,6)

K1_Lemon = 5; % (in uM)
% unphosphorylated receptor dissociation constant
% taken from Lukas 2004a and Flaherty 2007
% P(i,7)

K2_Lemon = 100; % (in uM)
% phosphorylated receptor dissociation constant
% taken from Lemon
% P(i,8)
%-----

%% Parameters G-protein cascade and DAG dynamics

```

```

GT = 3e5; % total number of G-protein molecules in the cell
% taken from Flaherty 2007 (measured in RAW)
% P(i,9)

L = 25; % (in uM) % ligand concentration
% P(i,10)

ka_tilde = 0.137 * m2uM * RT; % nondim. G-protein activation rate
% 0.137 /uM /s taken from Flaherty 2007
% P(i,11)

kd = 0.02; % (in /s) % GTP-ase parameter
% Mahama & Lindermann 1994
% P(i,12)

khyd = 1e-005; % (in /#mol /s) % effective hydrolysis rate
% SIMULINK 070404d
khyd_tilde = 1e-005 * GT; % khyd for nondim. system
% P(i,13)

krep = 0.014; % (in /s) % recycling of PIP2 to PM
% SIMULINK 070404d
% P(i,14)

kd3 = 0.006; % (in /s) % IP3 removal rate to IP4 or IP2
% SIMULINK 070404d
% P(i,15)

```

```

PIP2T = 9e6; % initial number of PIP2 molecules
% estimated from mass spec measurements in RAW cells
% P(i,16)
% PIP2T_conc = P(:,16)*m2uM;
% converts number of PIP2T to concentration (uM)

k_dp2 = 0.00171; % (in /s)
% effective phosphorylation rate of DAG from pool2
% better fit for SIMULINK 070404d (for 34:1 DAG)
% P(i,17)
% k_dp2 = 0.0050712; value for 38:4 DAG from SIMULINK 070404m

k_ap2 = 0.00196; % (in /s)
% effective production rate of pool 2 DAG
% SIMULINK 070404d (for 34:1 DAG)
% P(i,18)

k_dp1 = 0.0012; % (in /s)
% effective degradation rate of pool 1 DAG (PM)
% SIMULINK 070404d
% P(i,19)

Kc = 0.4; % (in uM)
% Ca2+ dissociation constant from PLC
% taken from Flaherty 2007
% P(i,20)

x7fac = 0.45; % controls the percentage of pool 2 DAG immediately used

```

```

% for pool 1 DAG production (to in effect simulate the delayed response
% SIMULINK 070404d
% P(i,21)

zeta_341 = initial_341_DAG/(m2uM*PIP2T);

zeta_384 = initial_384_DAG/(m2uM*PIP2T);

N = 8e6; % number of cells we are simulating for DAG

%-----

%Parameters for Ca2+ contribution

v1 = 40; % (in /s)
% taken from Li

d_ip3 = 0.2; %(in uM)
% taken from Li

d_act = 0.4; %(in uM)
% taken from Li

v2 = 0.00508; % (in /s)
% SIMULINK est. on 3/30/07

c1 = 0.185;

```

% taken from De Young 1992

v3 = 0.24; % (in uM /s)

% taken from Li

k_er = 0.4; % (in uM)

% taken from Lemon

epsilon = 0.01;

% taken from Li 1994 and De Young 1992

j_in = 0.44715; % (in uM /s)

% SIMULINK est. on 3/30/07

v4 = 1.3958; % (in uM /s)

% SIMULINK est. on 3/30/07

k_pl = 0.015555; % (in uM)

% SIMULINK est. on 3/30/07

a = 3.1; % (in /s)

% SIMULINK est. on 3/30/07

d_inh = 0.02; % (in uM)

% taken from Lemon

%-----

```

% ODE solver that calls "hannah_odes" and integrates the system of
% odes

clear y y1 y2 y3 y4 y5 y6 y7 y8 y9 y10

for i = 1:runstot % "i" goes from 1 to the number of rows in P

    % zeta_341 = .1*initial_341_DAG/(m2uM*P(i,16));
    x0 = [P(i,3),0,0,P(i,16),0,0,P(i,2),0.0009,0.8,2];
    [t,x] = ode15s(@hannah_odes, tspan, x0);
    % evaluate ODEs using ode15s solver
    y(:, :, i) = x;
    % hold on
    plot(t, (x(:,6)*uM2ng341*N + (x(:,7)-P(i,2))*uM2ng341*N))
    % plot(t, (x(:,6)*PIP2T_conc*uM2ng384*N + (x(:,7)-1)
    % *initial_384_DAG*uM2ng384*N))
    % plot(t, (x(:,5)*P(i,16)*m2uM*uM2pmoles*3.5e5), 'k')
    % plot pmoles of IP3 per 3.5E5 cells
    % Note: I can include the plot functions in this loop to see
    % what's happening to the shape of each graph for each of the
    % sample matrices.

end

% hold off

% Here I'm getting the y's in the form that's easier to input into
% SimLab

for k = 1:final_time+1 % the k's are time points
    for m = 1:runstot % the m's are sample numbers
        y1(m,k) = y(k,1,m);
        % e.g. y1(5,10) = the value of y1 at the 10th
        % time interval, for the 5 sample in the parameter matrix P
    end
end

```



```

        y2(m,k) = y(k,2,m);
        y3(m,k) = y(k,3,m);
        y4(m,k) = y(k,4,m);
        y5(m,k) = y(k,5,m);
        y6(m,k) = y(k,6,m);
        y7(m,k) = y(k,7,m);
        y8(m,k) = y(k,8,m);
        y9(m,k) = y(k,9,m);
        y10(m,k) = y(k,10,m);

    end

end

%-----

%%%%%%%%%%%%%%%%%%%%%%%%%%%%%%%%%%%%%%%%%%%%%%%%%%%%%%%%%%%%%%%%%%%%%%%% PLOT IP3 %%%%%%%%%%%%%%%%%%%%%%%%%%%%%%%%%%%%%%%%%%%%%%%%%%%%%%%%%%%%%%%%%%%%%%%%%

% plot(t,(x(:,5)*uM2pmoles*3.5e5),'k')
% plots pmoles of IP3 per 3.5E5 cells
% ylabel('\bf \Delta IP_3 (in pmoles per 3.5E5 cells)')

ip3t = [0 180 240 300 600 900 1200 1800];
ip3_data = [0.00 8.78 8.94 7.46 6.74 5.95 5.15 1.25];
ip3_error = [0.55 1.64 2.83 1.59 0.83 1.08 1.20 2.09];
%used to plot IP3 data points

% hold on
% errorbar(ip3t,ip3_data,ip3_error,'k.')
% hold off
% axis([-200 2000 -2 18]);

```

```

%%%%%%%%%%%%%%%%%%%%%%%%%%%%%%%%%%%%%%%%%%%%%%%%%%%%%%%%%%%%%%%%%%%%%%%% PLOT 34:1 DAG %%%%%%%%%%%%%%%%%%%%%%%%%%%%%%%%%%%%%%%%%%%%%%%%%%%%%%%%%%%%%%%%%%%%%%%%%
% plot(t,(y6(1,:)*uM2ng341*N)+ (y7(1,:)-P(2))*uM2ng341*N,'k')
% plot(t,(x(:,6)*PIP2T_conc*uM2ng341*N)+ (x(:,7)-1)
% *initial_341_DAG*uM2ng341*N,'k')
% plot ng amount of total 34:1 DAG
% ylabel('\bf \Delta 34:1 DAG (in ng per 8E6 cells)')
% xlabel('\bf time (seconds)')

dag341t = [0 30 120 180 900 1800];
dag341_data = [0 11.01 43.20 10.86 103.61 75.01];
dag341_error = [0 18.88 28.57 9.59 13.34 22.90];
% used to plot 34:1 DAG data points

% hold on
% errorbar(dag341t,dag341_data,dag341_error,'k.')
% hold off
% axis([-200 2000 -10 120]);

%%%%%%%%%%%%%%%%%%%%%%%%%%%%%%%%%%%%%%%%%%%%%%%%%%%%%%%%%%%%%%%%%%%%%%%% PLOT 38:4 DAG %%%%%%%%%%%%%%%%%%%%%%%%%%%%%%%%%%%%%%%%%%%%%%%%%%%%%%%%%%%%%%%%%%%%%%%%%
% plot(t,(y6(1,:)*PIP2T_conc*uM2ng384*N)+ (y7(1,:)-1)
% *initial_384_DAG*uM2ng384*N,'k')
% plot(t,(x(:,6)*PIP2T_conc*uM2ng384*N)+ (x(:,7)-1)
% *initial_384_DAG*uM2ng384*N,'k')
% plot ng amount of total 38:4 DAG
% ylabel('\bf \Delta 38:4 DAG (in ng per 4E6 cells)')

```

```

% xlabel('\bf time (seconds)')

dag384t = [0 30 120 180 900 1800];
dag384_data = [0 2.50 14.54 26.20 45.48 25.98];
dag384_error = [0 2.83 3.97 3.58 5.43 4.78];
% used to plot 38:4 DAG data points

% hold on
% errorbar(dag384t,dag384_data,dag384_error,'k.')
% hold off
% axis([-200 2000 -10 60]);

% plot(t,y8(1,:)) % Ca2+ trace

%%%%%%%%%%%%%%%%%%%%%%%%%%%%%%%%%%%%%%%%%%%%%%%%%%%%%%%%%%%%%%%%%%%%%%%%% STATS FOR Y1 = activated receptors %%%%%%%%%%%%%%%%%%%%%%%%%%%%%%%%%%%%%%%%%%%%%%%%%%%%%%%%%%%%%%%%%%%%%%%%%%
for q=1:final_time+1
    [b1,bint1,r1,rint1,stats1] = regress(y1(:,q),[ones(runstot,1) P]);
    src1(:,q) = b1;
    % SRC for coefficients at t(q)
    srcint1(:,q) = bint1;
    % SRC interval for coefficients at t(q)
    res1(:,q) = r1;
    % residuals for coefficients at t(q)
    resint1(:,q) = rint1;
    % residual intervals for coefficients at t(q)
    R2Fpe1(q,:) = stats1;
    % R^2 value, Fstatistic, p-value for F statistic,
    % and error for coefficients at t(q)

```

```

end

% rcoplot(res1(:,43),resint1(:, :,43)) % plots the residuals and their
% error bars for y1 at the 15th time point

%%%%%%%%%%%%%%%%%%%%%%%%%%%%%%%%%%%%%%%%%%%%%%%%%%%%%%%%%%%%%%%%%%%%%%%%% STATS FOR Y2 = phos. receptors %%%%%%%%%%%%%%%%%%%%%%%%%%%%%%%%%%%%%%%%%%%%%%%%%%%%%%%%%%%%%%%%%%%%%%%%%%
for q=1:final_time+1
    [b2,bint2,r2,rint2,stats2] = regress(y2(:,q),[ones(runstot,1) P]);
    src2(:,q) = b2;
    % SRC for coefficients at t(q)
    srcint2(:, :,q) = bint2;
    % SRC interval for coefficients at t(q)
    res2(:,q) = r2;
    % residuals for coefficients at t(q)
    resint2(:, :,q) = rint2;
    % residual intervals for coefficients at t(q)
    R2Fpe2(q,:) = stats2;
    % R^2 value, Fstatistic, p-value for F statistic,
    % and error for coefficients at t(q)
end

% rcoplot(res2(:,15),resint2(:, :,15)) % plots the residuals and their
% error bars for y2 at the 15th time point

%%%%%%%%%%%%%%%%%%%%%%%%%%%%%%%%%%%%%%%%%%%%%%%%%%%%%%%%%%%%%%%%%%%%%%%%% STATS FOR Y3 = G-proteins %%%%%%%%%%%%%%%%%%%%%%%%%%%%%%%%%%%%%%%%%%%%%%%%%%%%%%%%%%%%%%%%%%%%%%%%%%
for q=1:final_time+1
    [b3,bint3,r3,rint3,stats3] = regress(y3(:,q),[ones(runstot,1) P]);
    src3(:,q) = b3;
    % SRC for coefficients at t(q)
    srcint3(:, :,q) = bint3;

```

```

% SRC interval for coefficients at t(q)
res3(:,q) = r3;
% residuals for coefficients at t(q)
resint3(:, :, q) = rint3;
% residual intervals for coefficients at t(q)
R2Fpe3(q, :) = stats3;
% R^2 value, Fstatistic, p-value for F statistic,
% and error for coefficients at t(q)
end

% rcoplot(res3(:,15),resint3(:, :,15)) % plots the residuals and their
% error bars for y3 at the 15th time point

%%%%%%%%%%%%%%%%%%%%%%%%%%%%%%%%%%%%%%%%%%%%%%%%%%%%%%%%%%%%%%%%%%%%%%%%%% STATS FOR Y4 = PIP2 molecules %%%%%%%%%%%%%%%%%%%%%%%%%%%%%%%%%%%%%%%%%%%%%%%%%%%%%%%%%%%%%%%%%%%%%%%%%%%
for q=1:final_time+1
    [b4,bint4,r4,rint4,stats4] = regress(y4(:,q),[ones(runstot,1) P]);
    src4(:,q) = b4;
    % SRC for coefficients at t(q)
    srcint4(:, :, q) = bint4;
    % SRC interval for coefficients at t(q)
    res4(:,q) = r4;
    % residuals for coefficients at t(q)
    resint4(:, :, q) = rint4;
    % residual intervals for coefficients at t(q)
    R2Fpe4(q, :) = stats4;
    % R^2 value, Fstatistic, p-value for F statistic,
    % and error for coefficients at t(q)
end

% rcoplot(res4(:,15),resint4(:, :,15)) % plots the residuals and their

```

```

% error bars for y4 at the 15th time point

%%%%%%%%%%%%%%%%%%%%%%%%%%%%%%%%%%%%%%%%%%%%%%%%%%%%%%%%%%%%%%%%%%%%%%%%%% STATS FOR Y5 = IP3 concentration %%%%%%%%%%%%%%%%%%%%%%%%%%%%%%%%%%%%%%%%%%%%%%%%%%%%%%%%%%%%%%%%%%%%%%%%%%%
for q=1:final_time+1
    [b5,bint5,r5,rint5,stats5] = regress(y5(:,q),[ones(runstot,1) P]);
    src5(:,q) = b5;
    % SRC for coefficients at t(q)
    srcint5(:, :,q) = bint5;
    % SRC interval for coefficients at t(q)
    res5(:,q) = r5;
    % residuals for coefficients at t(q)
    resint5(:, :,q) = rint5;
    % residual intervals for coefficients at t(q)
    R2Fpe5(q,:) = stats5;
    % R^2 value, Fstatistic, p-value for F statistic,
    % and error for coefficients at t(q)
end

% rcoplot(res5(:,15),resint5(:, :,15)) % plots the residuals and their
% error bars for y5 at the 15th time point

%%%%%%%%%%%%%%%%%%%%%%%%%%%%%%%%%%%%%%%%%%%%%%%%%%%%%%%%%%%%%%%%%%%%%%%%%% STATS FOR Y6 = DAG p1 %%%%%%%%%%%%%%%%%%%%%%%%%%%%%%%%%%%%%%%%%%%%%%%%%%%%%%%%%%%%%%%%%%%%%%%%%%%
for q=1:final_time+1
    [b6,bint6,r6,rint6,stats6] = regress(y6(:,q),[ones(runstot,1) P]);
    src6(:,q) = b6;
    % SRC for coefficients at t(q)
    srcint6(:, :,q) = bint6;
    % SRC interval for coefficients at t(q)
    res6(:,q) = r6;

```

```

% residuals for coefficients at t(q)
resint6(:, :, q) = rint6;

% residual intervals for coefficients at t(q)
R2Fpe6(q, :) = stats6;

% R^2 value, Fstatistic, p-value for F statistic,
% and error for coefficients at t(q)
end

% rcoplot(res6(:, 15), resint6(:, :, 15)) % plots the residuals and their
% error bars for y6 at the 15th time point

%%%%%%%%%%%%%%%%%%%%%%%%%%%%%%%%%%%%%%%%%%%%%%%%%%%%%%%%%%%%%%%%%%%%%%%%%% STATS FOR Y6 + Y7 = DAG p1+ DAG p2%%%%%%%%%%%%%%%%%%%%%%%%%%%%%%%%%%%%%%%%%%%%%%%%%%%%%%%%%%%%%%%%%%%%%%%%%%
for q=1:final_time+1
    [b341, bint341, r341, rint341, stats341] =
        regress((y6(:, q) + (y7(:, q))), [ones(runstot, 1) P]);
    src_DAG(:, q) = b341;
    % SRC for coefficients at t(q)
    srcint_DAG(:, :, q) = bint341;
    % SRC interval for coefficients at t(q)
    res_DAG(:, q) = r341;
    % residuals for coefficients at t(q)
    resint_DAG(:, :, q) = rint341;
    % residual intervals for coefficients at t(q)
    R2Fpe_DAG(q, :) = stats341;
    % R^2 value, Fstatistic, p-value for F statistic,
    % and error for coefficients at t(q)
end

% rcoplot(res_DAG(:, 15), resint_DAG(:, :, 15)) % plots the residuals and
% their error bars for y6+y7 at the 15th time point

```

```

%%%%%%%%%%%%%%%%%%%%%%%%%%%%%%%%%%%%%%%%%%%%%%%%%%%%%%%%%%%%%%%%%%%%%%%%% STATS FOR Y7 = DAG p2 %%%%%%%%%%%%%%%%%%%%%%%%%%%%%%%%%%%%%%%%%%%%%%%%%%%%%%%%%%%%%%%%%%%%%%%%%%
for q=1:final_time+1
    [b7,bint7,r7,rint7,stats7] = regress(y7(:,q),[ones(runstot,1) P]);
    src7(:,q) = b7;
    % SRC for coefficients at t(q)
    srcint7(:, :,q) = bint7;
    % SRC interval for coefficients at t(q)
    res7(:,q) = r7;
    % residuals for coefficients at t(q)
    resint7(:, :,q) = rint7;
    % residual intervals for coefficients at t(q)
    R2Fpe7(q,:) = stats7;
    % R^2 value, Fstatistic, p-value for F statistic,
    % and error for coefficients at t(q)
end

% rcoplot(res7(:,15),resint7(:, :,15)) % plots the residuals and their
% error bars for y7 at the 15th time point

%%%%%%%%%%%%%%%%%%%%%%%%%%%%%%%%%%%%%%%%%%%%%%%%%%%%%%%%%%%%%%%%%%%%%%%%% STATS FOR Y8 = Ca2+ %%%%%%%%%%%%%%%%%%%%%%%%%%%%%%%%%%%%%%%%%%%%%%%%%%%%%%%%%%%%%%%%%%%%%%%%%%
for q=1:final_time+1
    [b8,bint8,r8,rint8,stats8] = regress(y8(:,q),[ones(runstot,1) P]);
    src8(:,q) = b8;
    % SRC for coefficients at t(q)
    srcint8(:, :,q) = bint8;
    % SRC interval for coefficients at t(q)
    res8(:,q) = r8;
    % residuals for coefficients at t(q)

```



```

    resint8(:,:,q) = rint8;
    % residual intervals for coefficients at t(q)
    R2Fpe8(q,:) = stats8;
    % R^2 value, Fstatistic, p-value for F statistic,
    % and error for coefficients at t(q)
end
% rcoplot(res8(:,15),resint8(:,:,15)) %plots the residuals and their
% error bars for y8 at the 15th time point

%%%%%%%%%%%%%%%%%%%%%%%%%%%%%%%%%%%%%%%%%%%%%%%%%%%%%%%%%%%%%%%%%%%%%%%%% STATS FOR Y9 = h %%%%%%%%%%%%%%%%%%%%%%%%%%%%%%%%%%%%%%%%%%%%%%%%%%%%%%%%%%%%%%%%%%%%%%%%%%
for q=1:final_time+1
    [b9,bint9,r9,rint9,stats9] = regress(y9(:,q),[ones(runstot,1) P]);
    src9(:,q) = b9;
    % SRC for coefficients at t(q)
    srcint9(:,:,q) = bint9;
    % SRC interval for coefficients at t(q)
    res9(:,q) = r9;
    % residuals for coefficients at t(q)
    resint9(:,:,q) = rint9;
    % residual intervals for coefficients at t(q)
    R2Fpe9(q,:) = stats9;
    % R^2 value, Fstatistic, p-value for F statistic,
    % and error for coefficients at t(q)
end
% rcoplot(res9(:,15),resint9(:,:,15)) % plots the residuals and their
% error bars for y9 at the 15th time point

%%%%%%%%%%%%%%%%%%%%%%%%%%%%%%%%%%%%%%%%%%%%%%%%%%%%%%%%%%%%%%%%%%%%%%%%% STATS FOR Y10 = c0 %%%%%%%%%%%%%%%%%%%%%%%%%%%%%%%%%%%%%%%%%%%%%%%%%%%%%%%%%%%%%%%%%%%%%%%%%%

```

```

for q=1:final_time+1
    [b10,bint10,r10,rint10,stats10] =
        regress(y10(:,q),[ones(runstot,1) P]);
    src10(:,q) = b10;
    % SRC for coefficients at t(q)
    srcint10(:, :,q) = bint10;
    % SRC interval for coefficients at t(q)
    res10(:,q) = r10;
    % residuals for coefficients at t(q)
    resint10(:, :,q) = rint10;
    % residual intervals for coefficients at t(q)
    R2Fpe10(q,:) = stats10;
    % R^2 value, Fstatistic, p-value for F statistic,
    % and error for coefficients at t(q)
end

% rcoplot(res10(:,15),resint10(:, :,15)) % plots the residuals and their
% error bars for y10 at the 15th time point

```

BIBLIOGRAPHY

- [1] Amann, H. *Ordinary Differential Equations, An Introduction to Nonlinear Analysis*, de Gruyter Studies in Mathematics, 13, Berlin. 1990.
- [2] Araki, W. and R. J. Wurtman. Control of membrane phosphatidylcholine biosynthesis by diacylglycerol levels in neuronal cells undergoing neurite outgrowth. *Proc. Natl. Acad. Sci.* **94** (1997), no. 22, 11946–11950.
- [3] Benard, S., J. Arnhold, M. Lehnert, J. Schiller, and K. Arnold. Experiments towards quantification of saturated and polyunsaturated diacylglycerols by matrix-assisted laser desorption and ionization time-of-flight mass spectrometry. *Chem. Phys. Lipids.* **100** (1999), 115–125.
- [4] Bishop, W. R. and R. M. Bell. Functions of diacylglycerol in glycerolipid metabolism, signal transduction and cellular transformation. *Oncogene Res.* **2** (1988), 205–218.
- [5] Bligh, E. G. and W. J. Dyer. A rapid method of total lipid extraction and purification. *Can. J. Biochem. Physiol.* **37** (1959), 911–917.
- [6] Brinson, A. E. and T. K. Harden. Differential Regulation of the Uridine Nucleotide-activated P2Y4 and P2Y6 Receptors. *J. Biol. Chem.* **276** (2001), 11939–11948.
- [7] Born, G. V. and M. A. Kratzer. Source and concentration of extracellular adenosine triphosphate during haemostasis in rats, rabbits and man. *J. Physiol.* **354** (1984), 419–429.
- [8] Brauer, F. and J. A. Nohel *The Qualitative Theory of Ordinary Differential Equations*, W.A. Benjamin, INC., New York. 1969.
- [9] Cabot, M. C., C. J. Welsh, Z. Zhang, H. Cao, H. Chabbott, and M. Lebowitz. Vasopressin, phorbol diesters and serum elicit choline glycerophospholipid hydrolysis and diacylglycerol formation in nontransformed cells: transformed derivatives do not respond. *Biochem. Biophys. Acta* **959** (1988), no. 1, 46–57.
- [10] Callender, H. L., J. S. Forrester, P. Ivanova, A. Preininger, S. Milne, and H. A. Brown. Quantification of diacylglycerol species from cellular extracts by electrospray ionization mass spectrometry using a linear regression algorithm. *Anal. Chem.* **79** (2007), 263–272.
- [11] Caloca, M. J., M. L. Garcia-Bermejo, P. M. Blumberg, M. E. Lewin, E. Kremmer, H. Mischak, S. Wang, K. Narco, B. Bienfait, V. E. Marquez, and M. G. Kazanietz. beta2-chimaerin is a novel target for diacylglycerol: binding properties and changes in subcellular localization mediated by ligand binding to its C1 domain. *Proc. Natl. Acad. Sci. U. S. A.* **96** (1999), 11854–11859.

- [12] Cook, R. D. Detection of Influential Observations in Linear Regression. *Technometrics* **19** (1977), 15–18.
- [13] Connolly, G. P. and J. A. Duley. Uridine and its nucleotides: biological actions, therapeutic potentials. *Trends. Pharmacol. Sci.* **20** (1999), 218–225.
- [14] Deacon, E. M., T. R. Pettitt, P. Webb, T. Cross, H. Chahal, M. J. O. Wakelam, and J. M. Lord. Generation of diacylglycerol molecular species through the cell cycle: a role for 1-stearoyl, 2-arachidonyl glycerol in the activation of nuclear protein kinase C-betaII at G2/M. *J. Cell Sci.* ,**115** (2002), 983–989.
- [15] Dekker, L. V. and P. J. Parker. Protein kinase C—a question of specificity. *Trends Biochem. Sci.* **19** (1994), 73–77.
- [16] De Young, G. and J. Keizer. A single-pool inositol 1,4,5-trisphosphate-receptor-based model for agonist-stimulated oscillations in Ca^{2+} concentration. *Proc. Natl. Acad. Sci. U.S.A.* **89** (1992), 9895–9899.
- [17] Divecha, N., D. J. Lander, T. W. Scott, and R. F. Irvine. Molecular species analysis of 1,2-diacylglycerols and phosphatidic acid formed during bombesin stimulation of Swiss 3T3 cells. *Biochim. Biophys. Acta* **1093** (1991), 184–188.
- [18] Ebinu, J. O., D. A. Bottorff, E. Y. W. Chan, S. L. Stang, R. J. Dunn, J. C. Stone. RasGRP, a Ras guanyl nucleotide-releasing protein with calcium- and diacylglycerol-binding motifs. *Science* **280** (1998), 1082–1086.
- [19] Flaherty, P. J. A Kinetic Model of G protein-coupled Signal Transduction in Macrophage Cells. Preprint. 2007.
- [20] Forrester, J. S., S. B. Milne, P. T. Ivanova, and H. A. Brown. Computational lipidomics: a multiplexed analysis of dynamic changes in membrane lipid composition during signal transduction. *Mol. Pharm.* **65** (2004), no. 4, 813–821.
- [21] Garrad, R. C., M. A. Otero, L. Erb, P. M. Theiss, L. L. Clarke, F. A. Gonzalez, J. T. Turner, and G. A. Weisman. Structural Basis of Agonist-induced Desensitization and Sequestration of the P2Y2 Nucleotide Receptor. *J. Biol. Chem.* **273** (1998), 29437–29444.
- [22] Grillone, L. R., M. A. Clark, R. W. Godfrey, F. Stassen, and S. T. Crooke. Vasopressin induces V1 receptors to activate phosphatidylinositol- and phosphatidylcholine-specific phospholipase C and stimulates the release of arachidonic acid by at least two pathways in the smooth muscle cell line, A-10. *J. Biol. Chem.* **263** (1988), 2658–2663.
- [23] Grygorczyk, R. and J. W. Hanrahan. CFTR-independent ATP release from epithelial cells triggered by mechanical stimuli. *Am. J. Physiol.* **272** (1997), C1058–C1066.

- [24] Habenicht, A. J. R., J. A. Glomset, W. C. King, C. Nist, C. D. Mitchell, and R. Ross. Early changes in phosphatidylinositol and arachidonic acid metabolism in quiescent swiss 3T3 cells stimulated to divide by platelet-derived growth factor. *J. Biol. Chem.* **256** (1981), 12329–12335.
- [25] Han, X. and R. W. Gross. Quantitative analysis and molecular species fingerprinting of triacylglyceride molecular species directly from lipid extracts of biological samples by electrospray ionization tandem mass spectrometry. *Anal. Biochem.* **295** (2001), no. 1, 88–100.
- [26] Hou, M., T. K. Harden, C. M. Kuhn, B. Baldetorp, E. Lazarowski, W. Pendergast, S. Moller, L. Edvinsson, and D. Erlinge. UDP acts as a growth factor for vascular smooth muscle cells by activation of P2Y(6) receptors. *Am. J. Physiol. Heart Circ. Physiol.* **282** (2002), H784–H792.
- [27] Hubbard, W. C., T. R. Hundley, A. Oriente, and D. W. MacGlashan, Jr. Quantitation of 1-stearoyl-2-arachidonoyl-sn-3-glycerol in human basophils via gas chromatography-negative ion chemical ionization mass spectrometry. *Anal. Biochem.* **236** (1996), 309–321.
- [28] Iman, R. L., J. M. Davenport, D. K. Zeigler. Latin hypercube sampling (Program user’s guide). *SANDIA Laboratory report* (1980) SAND79–1473.
- [29] Ivanova, P. T., S. B. Milne, J. S. Forrester, and H. A. Brown. LIPID Arrays: New Tools in the Understanding of Membrane Dynamics and Lipid Signaling. *Mol. Interv.* **4** (2004), no. 2, 86–96.
- [30] Jolly, C. A, J. C. Laurenza, D. N. McMurray, and R. S. Chapkin. Diacylglycerol and ceramide kinetics in primary cultures of activated T-lymphocytes. *Immunol. Lett.* **49** (1996), 43–48.
- [31] Kawasaki, H., G. M. Springett, T. Shinichiro, J. J. Canales, P. Harlan, J. P. Blumenstiel, E. J. Chen, A. Bany, N. Mochizuki, A. Ashbacher, M. Matsuda, D. E. Housman, and A. M. Graybiel. A Rap guanine nucleotide exchange factor enriched highly in the basal ganglia. *Proc. Natl. Acad. Sci. U. S. A.* **95** (1998), 13278–13283.
- [32] Keizer, J. *Statistical Thermodynamics of Nonequilibrium Processes* Springer, New York. 1987.
- [33] Keizer, J. and G. De Young. Two roles for Ca^{2+} in agonist stimulated Ca^{2+} oscillations. *Biophys. J.* **61** (1992), 649–660.
- [34] Koivusalo, M., P. Haimi, L. Heikinheimo, R. Kostiaainen, and P. Somerharju. Quantitative determination of phospholipid compositions by ESI-MS: effects of acyl chain length, unsaturation, and lipid concentration on instrument response. *J. Lipid Res.* **42** (2001), 663–672.

- [35] Korcok, J., L. N. Raimundo, X. Du, S. M. Sims, and S. J. Dixon. P2Y6 Nucleotide Receptors Activate NF- κ B and Increase Survival of Osteoclasts. *J. Bio. Chem.* **280** (2005), 16909–16915.
- [36] Lazarowski, E. R. and T. K. Harden. Quantitation of extracellular UTP using a sensitive enzymatic assay. *Br. J. Pharmacol.* **127** (1999), 1272–1278.
- [37] Lee, C., S. K. Fisher, B. W. Agranoff, and A. K. Hajra. Quantitative analysis of molecular species of diacylglycerol and phosphatidate formed upon muscarinic receptor activation of human SK-N-SH neuroblastoma cells. *J. Biol. Chem.* **266** (1991), no. 34, 22837–22846.
- [38] Leis, J. R. and M. A. Kramer. The simultaneous solution and sensitivity analysis of systems described by ordinary differential equations. *ACM Transactions on Mathematical Software (TOMS)*. **14** (1988), no. 1, 45–60.
- [39] Lemon, G., W. G. Gibson, and M. R. Bennett. Metabotropic receptor activation, desensitization and sequestration—I: modelling calcium and inositol 1,4,5-trisphosphate dynamics following receptor activation. *J. Theor. Bio.* **223** (2003), 93–111.
- [40] Li, Y. and J. Rinzel. Equations for InsP₃ receptor-mediated $[Ca^{2+}]_i$ oscillations derived from a detailed kinetic model: a Hodgkin-Huxley like formalism. *J. Theor. Bio.* **166** (1994), 461–473.
- [41] Lukas, T. J. A signal transduction pathway model prototype i: From agonist to cellular endpoint. *Biophys. J.* **87** (2004), no. 3, 1406–1416.
- [42] Magnaldo, I., G. L’Allemain, J. C. Chambard, M. Moenner, D. Barritault, and J. Pouysigur. The mitogenic signaling pathway of fibroblast growth factor is not mediated through polyphosphoinositide hydrolysis and protein kinase C activation in hamster fibroblasts. *J. Biol. Chem.* **261** (1986), 16916–16922.
- [43] Mahama, P. A. and J. J. Linderman. A Monte Carlo study of the dynamics of G protein activation. *Biophys. J.* **67** (1994), 1345–1357.
- [44] The Mathworks Website, <<http://www.mathworks.com>> (2007)
- [45] Mishra, J. and U. S. Bhalla. Simulations of Inositol Phosphate Metabolism and Its Interaction with InsP₃-Mediated Calcium Release. *Biophys. J.* **83** (2002), 1298–1316.
- [46] Mochly-Rosen, D. Localization of protein kinases by anchoring proteins: a theme in signal transduction. *Science* **268** (1995), 247–251.
- [47] Morris, M. D. Factorial Sampling Plans for Preliminary Computational Experiments. *Technometrics* **33** (1991), no. 2, 161–174.
- [48] Murphy, R. C., J. Fiedler, and J. Hevko. Analysis of nonvolatile lipids by mass spectrometry. *Chem. Rev.* **101** (2001), no. 2, 479–526.

- [49] Natarajan, M., K. M. Lin, R. C. Hsueh, P. C. Sternweis, and R. Ranganathan. A global analysis of cross-talk in a mammalian cellular signalling network. *Nat. Cell. Biol.* **8** (2006), 571–580.
- [50] Newton, A. C. Protein Kinase C: Structure, Function, and Regulation. *J. Biol. Chem.* **270** (1995), 28495–28498.
- [51] Nicolas, R. A., W. C. Watt, E. R. Lazarowski, et al. Uridine nucleotide selectivity of three phospholipase C-activating P2 receptors: identification of a UDP-selective, and a UTP-specific receptor. *Mol. Pharm.* **50** (1996), 224–229.
- [52] Nishizuka, Y. Protein kinase C and lipid signaling for sustained cellular responses. *FASEB J.* **9** (1995), 484–496.
- [53] Palmer, S., K. T. Hughes, D. Y. Lee, and M. J. O. Wakelam. Development of a novel, Ins(1,4,5)P3-specific binding assay: Its use to determine the intracellular concentration of Ins(1,4,5)P3 in unstimulated and vasopressin-stimulated rat hepatocytes. *Cell Signal.* **1** (1989), no. 2, 147–156.
- [54] Pessin, M. S., J. J. Baldassare, and D. M. Raben. Molecular species analysis of mitogen-stimulated 1,2-diglycerides in fibroblasts. Comparison of alpha-thrombin, epidermal growth factor, and platelet-derived growth factor. *J. Biol. Chem.* **265** (1990), 7959–7966.
- [55] Pettitt, T. R., A. Martin, T. Horton, C. Liossis, J. M. Lord, and M. J. O. Wakeham. Diacylglycerol and phosphatidate generated by phospholipases C and D, respectively, have distinct fatty acid compositions and functions. Phospholipase D-derived diacylglycerol does not activate protein kinase C in porcine aortic endothelial cells. *J. Biol. Chem.* **272** (1997), 17354–17359.
- [56] Preiss, J., C. R. Loomis, W. R. Bishop, R. Stein, J. E. Niedel, and R. M. Bell. Quantitative measurement of sn-1,2-diacylglycerols present in platelets, hepatocytes, and ras- and sis-transformed normal rat kidney cells. *J. Biol. Chem.* **261** (1986), 8597–8600.
- [57] Preiss, J., R. M. Bell, and J. E. Niedel. Diacylglycerol mass measurements in stimulated HL-60 phagocytes. *J. Immunol.* **138** (1987), 1542–1545.
- [58] Purkiss, J. R. and M. R. Boarder. Stimulation of phosphatidate synthesis in endothelial cells in response to P2-receptor activation. Evidence for phospholipase C and phospholipase D involvement, phosphatidate and diacylglycerol interconversion and the role of protein kinase C. *Biochem. J.* **287** (1992), 31–36.
- [59] Raben, D. M., K. Yasuda, and D. D. Cunningham. Modulation of thrombin-stimulated lipid responses in cultured fibroblasts. Evidence for two coupling mechanisms. *Biochemistry* **26** (1987), 2759–2765.
- [60] Riccobene, T. A., G. M. Omann, and J. J. Linderman. Modeling activation and desensitisation of G-protein coupled receptors provides insight into ligand efficacy. *J. theor. Biol.* **200** (1999), 207–222.

- [61] Rosoff, P. M., N. Savage, and C. A. Dinarello. Interleukin-1 stimulates diacylglycerol production in T lymphocytes by a novel mechanism. *Cell* **54** (1988), no. 1, 73–81.
- [62] Rouzer, C. A., P. J. Kingsley, H. Wang, H. Zhang, J. D. Morrow, S. K. Dey, and L. J. Marnett. Cyclooxygenase-1-dependent prostaglandin synthesis modulates tumor necrosis factor- α secretion in lipopolysaccharide-challenged murine resident peritoneal macrophages. *J. Biol. Chem.* **279** (2004), no. 33, 34256–34268.
- [63] Rouzer, C. A., P. T. Ivanova, M. O. Byrne, S. B. Milne, L. J. Marnett, and H. A. Brown. Lipid profiling reveals arachidonate deficiency in RAW264.7 cells: Structural and functional implications. *Biochemistry* **45** (2006), no. 49, 14795–14808.
- [64] Rouzer, C. A., P. T. Ivanova, M. O. Byrne, H. A. Brown, and L. J. Marnett. Lipid profiling reveals glycerophospholipid remodeling in zymosan-stimulated macrophages. *Biochemistry* **46** (2007), no. 20, 6026–6042.
- [65] Saltelli, A., S. Tarantola, F. Campolongo, M. Ratto. *Sensitivity Analysis In Practice: A Guide to Assessing Scientific Models*, John Wiley & Sons Inc., Hoboken, NJ. 2004
- [66] Saltelli, A. Sensitivity analysis. Could better methods be used? *J. Geophys. Res.* **104** (1999), no. D3, 3789–93.
- [67] Saltelli, A., M. Ratto, S. Tarantola, and F. Campolongo. Sensitivity Analysis for Chemical Models. *Chem. Rev.* **105** (2005), no. 7, 2811–2828.
- [68] Sasada, M., M. J. Pabst, R. B. Johnston, Jr. Activation of Mouse Peritoneal Macrophages by Lipopolysaccharide Alters the Kinetic Parameters of the Superoxide-producing NADPH Oxidase. *J. Bio. Chem.* **258** (1983), 9631–9635.
- [69] Sasaki, T. and H. Hasegawa-Sasaki. Molecular species of phosphatidylinositol, phosphatidic acid and diacylglycerol in a phytohemagglutinin-stimulated T-cell leukemia line. *Biochim. Biophys. Acta* **833** (1985), 316–322.
- [70] Seber, G. A. F. *Linear Regression Analysis*. John Wiley & Sons, New York. 1977.
- [71] Shampine, L. F. and M. W. Reichelt. The MATLAB ODE Suite. *SIAM Journal on Scientific Computing* **18** (1997), 1–22.
- [72] Sternweis, P. C. and A. V. Smrcka. G proteins in signal transduction: the regulation of phospholipase c. *Ciba. Found. Symp.* **176** (1993), 96–106.
- [73] Soto, G. and H. G. Othmer. A model for a G-protein-mediated mechanism for synaptic channel modulation. *Math Biosci.* **200** (2006), 188–213.
- [74] Tang, Y. and H. G. Othmer. Excitation, oscillations and wave propagation in a G-protein-based model of signal transduction in dictyostelium discoideum, *Philos. Trans. R. Soc. Lond. B: Biol. Sci.* **349** (1995), 179–195.

- [75] Turányi, T. Sensitivity analysis of complex kinetic systems. Tools and applications. *J. Math. Chem.* **5** (1990), 203–248.
- [76] Wagner, J. and J. Keizer. Effects of rapid buffers on Ca^{2+} diffusion and Ca^{2+} oscillations. *Biophys. J.* **67** (1994), 447–456.
- [77] Weiss, J. M., P. H. Morgan, M. W. Lutz, and T. P. Kenakin. The cubic ternary complex receptor-occupancy model I. Model description. *J. theor. Biol.* **178** (1996), 151–167.
- [78] Werner, M. H., A. E. Bielawska, and Y. A. Hannun. Diacylglycerol overcomes aspirin inhibition of platelets: evidence for a necessary role for diacylglycerol accumulation in platelet activation. *Mol. Pharm.* **41** (1991), 382–386.
- [79] Willars, G. B., S. R. Nahorski, and R. A. Challiss. Differential regulation of muscarinic acetylcholine receptor-sensitive polyphosphoinositide pools and consequences for signaling in human neuroblastoma cells. *J Biol Chem* **273** (1998), no. 9, 5037–5046.
- [80] Woolf, P. J. and J. J. Linderman. Untangling Ligand Induced Activation and Desensitization of G-ProteinCoupled Receptors. *Biophys. J.* **84** (2003), 3–13.
- [81] Wright, M. M. and C. R. McMaster. Phospholipid synthesis, diacylglycerol compartmentation, and apoptosis. *Biol. Res.* **35** (2002), 223–229.
- [82] Wright, T. M., L. A. Rangan, H. S. Shin, and D. M. Raben. Kinetic analysis of 1,2-diacylglycerol mass levels in cultured fibroblasts. Comparison of stimulation by alpha-thrombin and epidermal growth factor. *J. Biol. Chem.* **263** (1988), no. 19, 9374–9380.
- [83] Yamashita, S., N. Mochizuki, Y. Ohba, M. Tobiume, Y. Okada, H. Sawa, K. Nagashima, and M. Matsuda. CalDAG-GEFIII Activation of Ras, R-Ras, and Rap1*. *J. Biol. Chem.* **275** (2000), 25488–25493.
- [84] Yang, Y., L. Li, G. Wong, S. Krilis, M. Madhusudhan, A. Sali, and R. Stevens. RasGRP4, a new mast cell-restricted Ras guanine nucleotide-releasing protein with calcium- and diacylglycerol-binding motifs. Identification of defective variants of this signaling protein in asthma, mastocytosis, and mast cell leukemia patients and demonstration of the importance of RasGRP4 in mast cell development and function. *J. Biol. Chem.* **277** (2002), 25756–25774.
- [85] Yi, T. M., H. Kitano, M. I. Simon. A quantitative characterization of the yeast heterotrimeric G protein cycle. *Proc. Natl. Acad. Sci.* **100** (2003), 10764–10769.
- [86] Yoshioka, K., O. Saitoh, and H. Nakata. Heteromeric association creates a p2y-like adenosine receptor. *Proc. Natl. Acad. Sci. U.S.A.* **98** (2001), no. 13, 7617–7622.
- [87] You, J., C. R. Jacobs, T. H. Steinberg, and H. J. Donahue. P2Y Purinoceptors Are Responsible for Oscillatory Fluid Flow-induced Intracellular Calcium Mobilization in Osteoblastic Cells*. *J. Biol. Chem.* **277** (2002), no. 50, 48724–48729.

- [88] Zimmermann, H., N. Braun, B. Kegel, and P. Heine. New insights into molecular structure and function of ectonucleotidases in the nervous system. *Neurochem. Int.* **32** (1998), 421–425.